

ABSTRACT

Title of dissertation: THREE-DIMENSIONAL DISSIPATION
SCALE MEASUREMENTS OF
TURBULENT FLOWS

Benjamin Wolf Zeff, Doctor of Philosophy, 2002

Dissertation directed by: Professor Daniel P. Lathrop
Department of Physics

An understanding of turbulence, with its complex spatio-temporal structure, remains elusive. Ideally, an instrument to study the dynamics of turbulent flows would be capable of resolving the smallest relevant spatial and temporal scales in three dimensions. This dissertation details the development of a new optical measurement technique, three-dimensional, long-distance, high-speed micro particle image velocimetry (3-D LH μ PIV), and its application to two types of turbulent flow. This technique uses three cameras to simultaneously locally measure all three components of the velocity and all nine velocity gradients.

The first measurements were performed in turbulence produced by two oscillating grids at $Re = 2250$ ($R_\lambda=54$). Between the grids, the turbulent flow is nearly isotropic. Intense bursts of dissipation and enstrophy were observed, often show-

ing faster-than-exponential growth. We found high-dissipation and high-entropy events to be correlated in space and time, and we explore the processes by which these intense events may develop. Specifically, measured statistics and analysis of the equations of motion support the presence of a self-steepening mechanism which causes the dissipation to rise rapidly. The presence of large gradients, through vortex stretching, then produce a rapid increase in the entropy. The rising vorticity quickly damps the dissipation before itself declining suddenly. The second system studied was turbulent Rayleigh-Bénard convection with $Ra = 5.1 \times 10^9$ and $Re = 2000$. Thermal index of refraction variations in the fluid compromised the focus of one camera and reduced the quality of the data. A statistical comparison of the two systems supports Kolmogorov's 1941 hypothesis that small scale motions depend only on the average energy dissipation and viscosity and are independent of the large scale forcing. We also discuss means of improving the LH μ PIV technique and directions of future work.

THREE-DIMENSIONAL DISSIPATION SCALE
MEASUREMENTS OF TURBULENT FLOWS

by

Benjamin Wolf Zeff

Dissertation submitted to the Faculty of the Graduate School of the
University of Maryland, College Park in partial fulfillment
of the requirements for the degree of
Doctor of Philosophy
2002

Advisory Committee:

Professor Daniel P. Lathrop, Chair/Advisor
Assistant Professor Wolfgang Losert
Professor Edward Ott
Professor Rajarshi Roy
Professor James M. Wallace

© Copyright by
Benjamin Wolf Zeff
2002

ACKNOWLEDGEMENTS

I am so grateful to those people who have made this research and dissertation possible and those who have made my experience in graduate school one that I will always remember fondly.

I want to thank Jay Pyle for always being available to help out in the machine shop. I have made a lot of weird parts in the past 5 years, not all of which ever got used, and Jay was always willing to put his own work on hold to teach and offer advice. I would like to thank Dottie Brosius, who took pity on me when I wandered disheveled into her office for typesetting help. Her continuing assistance with the arcane workings of TEX typesetting will benefit many students. I want to thank Jane Hessing, who always seemed to have the answer to my questions before I had picked up the phone to call her. No forms or red tape could stop her.

I thank Dr. Katepelli Sreenivasan for his suggestions and useful discussion. I wish to thank the members of my committee, Ed Ott, Jim Wallace, Raj Roy, and Wolfgang Losert for comments and suggestions. I also thank Raj for his collaboration, financial and intellectual, on this project. I would like to thank Eric Kostelich, whose help in writing our analysis software was greatly appreciated.

I would like thank Don Martin for his technical advice and assistance. His

ideas and machining knowledge were extremely valuable in designing and building my experiments. To my “labmates”: I thank you for years of making my workdays fun. Your opinions and help were always appreciated, and our lunchtime intellectual jousting will be sorely missed. Given enough lunches, I am sure that we could solve the world’s problems (though it might slow our research progress). I would like to specifically thank Ryan McAllister and Dan Lanterman, who have worked with me on my dissertation project to get it going and keep it rolling.

More so than anyone, Dan Lathrop has guided my physics education. I have been a student of Dan’s for nearly a quarter of my life, and the things that I have learned from him are immeasurable. Wherever I am in life, the skills I learned from him will serve me well. Thank you for being an advisor and good friend.

I owe a special thanks to my Uncle Jack Miller. His “Zeff Higher Education Grants” made an enormous difference in my quality of life as a graduate student. I owe an obvious debt of gratitude to my parents and family who have been supportive every step of the way, and my mother- and father-in-law have made it easier to bear the burden of living apart from their daughter. Finally, I would like to extend a loving thank you to my wife, Nikki. Though we have lived apart, you have been there for me whenever I needed. You have waited, patiently and impatiently, through half a decade of our lives. Thank you so very, very much.

אתה חונן לאדם דעת.
ומלמד לאנוש בינה.
חננו מאתך דעה, בינה והשכל
ברוך אתה ה', חונן הרעות.
(אמירה החיל)

TABLE OF CONTENTS

List of Figures	vii
------------------------	------------

List of Tables	xvi
-----------------------	------------

1 Introduction	1
1.1 Background and Theory	3
1.1.1 Turbulence, Turbulence Everywhere...	3
1.1.2 Energy Dissipation and Turbulent Cascades	4
1.1.3 Intermittency	6
1.1.4 Euler Singularities	7
1.1.5 Interplay of Vorticity and Strain	8
1.2 Techniques of Flow Measurement	9
1.2.1 Single-Point Techniques (Eulerian)	11
1.2.2 Lagrangian Measurement Techniques	13
1.2.3 Particle Image Velocimetry	14

1.3	Numerical Work and Results	15
1.4	Dissertation Outline	18
2	Technique Development and Application	20
2.1	Measurement Theory	21
2.2	The Optical System	22
2.2.1	Tracer Particles	24
2.2.2	Laser Illumination	25
2.2.3	Video Cameras	30
2.2.4	System Alignment	32
2.3	The Control System	38
2.3.1	Video Recording	38
2.3.2	Video Synchronization	41
2.3.3	PIV Analysis Automation	42
2.4	Digital PIV Analysis	44
2.5	PIV Analysis	47
2.5.1	Spatial Rearrangement	53
2.5.2	Fitting the Linear Model	53
3	The Turbulent Flow Systems	57
3.1	Background	57
3.2	General Tank Design and Setup	61
3.2.1	Oscillating Grid Turbulence Setup	62

3.3	The Convection Setup	64
4	Results and Analysis	73
4.1	Grid Turbulence	73
4.1.1	Data Collection and Analysis	73
4.1.2	Grid Statistics	77
4.1.3	Dissipation and Enstrophy	88
4.2	Turbulent Rayleigh-Bénard Convection	102
4.3	Grid/Convection Statistical Comparison	109
5	Conclusions	112
A	Analysis Software	116
A.1	Automation	116
A.2	AVI File Format	117
A.3	PIV Analysis Code	118
A.4	Linear Least Squares Code	122
	Bibliography	135

LIST OF FIGURES

2.1	a) Three laser sheets illuminate three faces of a cubical volume within the flow. Each camera sees a two-dimensional particle field on one of the three faces. The fields of view for the three cameras are offset from the vertex of the cube. Particles within the cube and on the remaining three faces are not visualized. b) After being broken into subsections and digitally analyzed, each face yields an array of two-dimensional velocity vectors to be fit to a three-dimensional model.	23
2.2	Sample camera image of 1 μm polystyrene spheres suspended in the flow. The particles are illuminated by a laser sheet 0.018 cm thick in a plane perpendicular to the viewing angle. The resolution of the image is 240×210 pixels, corresponding to a region of flow 0.11×0.10 cm. Approximately 450 particles are visible in this image.	26
2.3	Cylindrical converging lenses are used to create laser sheets. A beam passed through the lens narrows to a thin waist before expanding again. By looking at particles in the region of the waist, a camera sees a two-dimensional slice of the flow.	29

2.4 a) 3-D view of the tank showing the three cameras and their laser sheets. The laser sheet for one horizontal camera traverses the tank from high to low along the viewing direction of the other. Camera/laser sheet pairs are numbered. b) A side view of one camera (facing out of the page) and its laser sheet. The other two cameras are similarly oriented. 34

2.5 Camera alignment procedure. a) To align camera 1 with the other two cameras, its field of view is positioned such that the laser sheets for cameras 2 and 3 are visible on screen. The thick white box shows the field of view of camera 1. b) Then, the field of view is repositioned so that the laser sheets for cameras 2 and 3 are off-screen to the left and down. This process is repeated for cameras 2 and 3. The point x_0 where the three laser sheets cross is shown at the bottom left. Positioning each field of view to be offset from x_0 guarantees that each camera sees only those particles in its own laser sheet. The linear model is fit around the origin x_0 35

2.6 3-D view of the tank and optical setup. The laser optics and two cameras are mounted on a raised platform to bring them level with the tank. The third camera is mounted on the optical table and faces vertically upward through the bottom of the tank. 36

2.7 Top view of the optical setup. 37

2.8	Schematic of the PCI 2000S camera memory buffer. Frames are recorded in a loop, overwriting previously recorded data. When a trigger is received, the recording stops (after completing the current frame), and the entire buffer is saved to disk.	39
2.9	Diagram of the frame alignment between cameras. The time lags between cameras, $t_1 - t_2$, $t_2 - t_3$, and $t_3 - t_1$, can be up to one frame length and change with each recording cycle.	43
2.10	Schematic of the video recording and processing loop for one camera. While one video sequence is processed on the analysis computer, the subsequent video sequence is recorded and saved.	45
2.11	Diagram of the data acquisition and control network. Dotted lines represent ethernet connections. Components shown in blue are used only for the convection system.	46
2.12	Flow chart of the digital analysis procedure.	48
2.13	Corresponding subsections from two consecutive frames and their cross-correlation. A red circle is drawn around one group of particles which appears in both frames. The location of the bright peak relative to the center of the image in the cross-correlation gives the average particle velocity between frames.	52
2.14	Subsection velocity traces before and after weighted averaging. Weighted averaging around the peak pixel (red curve) in the cross-correlation greatly reduces the pixel noise.	54

3.1	Images of particle streaks formed with low shutter speeds show the difference between flows with low and high turbulence intensity I_T . The low I_T image on the left is from a Taylor-Couette flow with $Re = 18,300$. The mean flow in this system is high, making it difficult to measure velocity gradients. The high I_T image is from oscillating grid turbulence with $Re = 2500$. Note the large variations in both the direction and magnitude of the velocity in the right high I_T image.	58
3.2	Proposed camera setup for LH μ PIV measurements in a Taylor-Couette flow apparatus. The three cameras image through a flat face cut into the outer cylinder. The inner cylinder rotates to drive the flow.	60
3.3	Cross-section of the tank with the bottom chamber attached. The top chamber and copper plate are added for convection, discussed, in Sec. 3.4.	63
3.4	Photograph of the double grid and mount.	68
3.5	Photograph of the grid-turbulence system.	69
3.6	Diagram of the system set up for turbulent convection. The three thermocouples are shown coming in through right side. Heated water is pumped in through two sides of the bottom chamber and out through the other two. Likewise, cooled water is pumped through the top chamber. The copper tube at the top right is used to fill and top off the convection cell.	70
3.7	Photograph of one of the end chambers. The arrows show the direction of flow for the cooling or heating water.	71

3.8	Wiring Diagram for the thermometry.	72
4.1	Plot of pixel noise vs. the weighted averaging radius r . Here, pixel noise $\equiv \langle(\delta v/\delta t)^4\rangle$. The solid line is for a weighted average using the pixel intensity, and the dashed line is for a weighted average using squared intensity. For a radius of zero, the velocity data was pixel quantized, and the noise was relatively high. Increasing the radius and squaring the intensity data in the averaging dramatically decreases the noise. A radius of 2 was used for the data analysis.	75
4.2	Subsection velocity traces from the three cameras. Each camera sees a two-dimensional slice of the flow and measures two components of the velocity in 4 subsections. The vertical oscillation of the grid is visible on the v_y traces from cameras 1 and 3. Gradients across the measurement volume appear as small differences in a particular velocity component between cameras.	76
4.3	Typical traces of the three components of \vec{v}_0 . The velocities are measured at time steps of 0.008 s.	78
4.4	Typical traces of three components, $\partial v_x/\partial x$, $\partial v_x/\partial y$, and $\partial v_x/\partial z$, of the gradient matrix \mathbf{M}	79
4.5	3-D vector plot of the flow inside the test volume. This image shows the flow, reconstructed using \vec{v}_0 and \mathbf{M} , during a very high dissipation event.	80

4.6 PDF of the v_y . The distribution is fit well by a gaussian, shown as a solid line. While, $\langle v_y \rangle > 0$, both negative and positive values are common. The PDF of v_x is similarly skewed to positive values, while $\langle v_z \rangle$ is very close to zero. Spurious high velocity points are seen at the lowest probability value. 82

4.7 Power spectrum of v_y showing a small region of $E(f) \propto f^{-5/3}$ scaling. Large peaks are seen at the oscillation frequency of the grid, $f = 10$ Hz, and at higher harmonics. 85

4.8 PDF of $\partial v_y / \partial z$, one component of the gradient matrix \mathbf{M} . The distribution is exponential with slight asymmetry around the mean. . . . 86

4.9 PDFs of a_x and the helicity h . a) The distribution of a_x is a stretched exponential, $Pr(a_x) \propto \exp(a_x^{0.68})$ as expected from previous analytical, numerical, and experimental work. b) The distribution of h is also a stretched exponential, $Pr(h) \propto \exp(h^{0.85})$, though its form is closer to a simple exponential. 87

4.10 a) PDFs of $\epsilon / \langle \epsilon \rangle$ (+) and $\Omega / \langle \Omega \rangle$ (o). The tails of the PDFs extend toward high values of ϵ and Ω and are fit well by stretched exponentials: $Pr(\epsilon) \propto \exp(-\epsilon^{0.6})$ and $Pr(\Omega) \propto \exp(-\Omega^{0.45})$. Their time averages are: $\langle \epsilon \rangle = 0.0337 \text{ cm}^2/\text{s}^3$ and $\langle \Omega \rangle = 4.13 \text{ 1/s}$. b) Log-log PDFs of ϵ and Ω show a significant skewing towards values below their time averages. At low values, ϵ and Ω show scalings $Pr(\epsilon) \propto \epsilon^{2.34}$ and $Pr(\Omega) \propto \Omega^{1.44}$ over four decades. 89

4.11 PDFs of λ_1 , λ_2 , and λ_3 , the eigenvalues of the symmetric strain matrix. Because the fluid is incompressible, $\lambda_1 < 0$ (representing compression), $\lambda_3 > 0$ (representing stretching), and $\sum \lambda_i = 0$. λ_2 can be either positive or negative, though the PDF is skewed toward positive values. 90

4.12 Time traces showing high dissipation (black) and enstrophy (red) events. The extreme events in both a) and b) are qualitatively similar, but the sharp rise in ϵ has a steeper functional form in the latter. A 3-D reproduction of the flow at the time of the ϵ peak in b) is shown in Fig. 4.5, in which both shear and rotation are visible. 92

4.13 Examples of both exponential and algebraic growth of ϵ . a) Exponential growth of ϵ during the intense event in Figure 4.12a. The straight line represents the exponential growth $\epsilon \propto e^{\alpha t}$ with $\alpha = 1.75$ 1/s. b) Log-log plot of exponential growth of ϵ for the event shown in Figure 4.12b and one other. The dissipation is plotted versus $t_0 - t$, where t_0 is a time towards which ϵ is attempting to diverge. The straight line represents the scaling $\epsilon \propto (t_0 - t)^{-2}$ expected in the presence of an Euler singularity. 93

4.14 A scatter plot of $\log(\epsilon/\langle\epsilon\rangle)$ and $\log(\Omega/\langle\Omega\rangle)$. The color of the graphs represents the value $Pr(\epsilon/\langle\epsilon\rangle, \Omega/\langle\Omega\rangle)/Pr(\epsilon/\langle\epsilon\rangle)Pr(\Omega/\langle\Omega\rangle)$ and would be 1 (green) everywhere if these two quantities were statistically independent. We find that very high values of the dissipation and enstrophy occur simultaneously about eight times more often than would be expected. Particularly low values are similarly correlated. 94

4.15 The average of $\dot{\epsilon}$ conditioned on $\lambda_3 > \lambda_c$. The gradients are subject to a self-steepening mechanism, so when λ_3 is large, the dissipation is typically rising. 95

4.16 The average of $\dot{\epsilon}$ conditioned on $\Omega > \Omega_0$. When the enstrophy is high, the dissipation is typically falling. 96

4.17 A vortex tube (high- Ω) and dissipation sheet (high- ϵ) passing through the measurement volume. The advection of such coherent structures offers one possible explanation for the observed statistics. 97

4.18 A possible sequence of events which could explain the observed statistics of ϵ and Ω . a) A region of high dissipation develops due to fluid motions. b) A self-steepening mechanism causes the gradients to grow rapidly, increasing both ϵ and Ω in tandem. c) An instability causes the formation of a vortex, which grows rapidly due to vortex stretching. d) As Ω rises, the dissipation falls. 100

4.19 Another sequence of events which may explain the observed statistics of ϵ and Ω . a) & b) A region of high dissipation and zero vorticity develops and is amplified by self-steepening mechanisms. c) An instability produces a non-zero vorticity which grows exponentially due to vortex stretching. d) The dissipation falls rapidly. 101

4.20 Sample frame of 1 μm particles imaged through the thermal boundary layer. Temperature fluctuations in the fluid change the index of refraction and the focal depth. 105

4.21 Subsection traces v_x and v_y for turbulent convection. Focusing problems results in poor cross-correlations that often show no velocity at all, as in the noisy section at the end. 106

4.22 Traces of the three components of \vec{v}_0 for turbulent convection. The velocity measurement error is higher than in the case of grid-generated turbulence. 107

4.23 Typical traces of three components, $\partial v_x/\partial x$, $\partial v_x/\partial y$, and $\partial v_x/\partial z$, of the gradient matrix \mathbf{M} for turbulent convection. The gradients are calculated from spatial variations of measured velocity components. Hence, the noise is magnified in these quantities. 108

4.24 PDFs of the scaled helicity for grid turbulence (+) and turbulent convection (\odot). 110

4.25 PDFs of the scaled dissipation for grid turbulence (+) and turbulent convection (\odot). Other than at very high values of ϵ , the statistics appear very similar. 111

LIST OF TABLES

1.1	Comparison of velocimetry techniques. The technique developed in this research (3-D LH μ PIV) has the distinction of being the only three-dimensional, non-invasive, time-resolved technique currently in use.	16
2.1	Frame rates, pixel resolution, and maximum record time for the Red-lake PCI 2000S camera.	31
2.2	Frame rates, pixel resolution, and maximum record time for the Red-lake PCI 2000S camera.	50
4.1	Time-average velocity components in oscillating grid turbulence. the grid oscillations are in the y -direction.	81
4.2	Time-average velocity components in turbulent convection.	104

Chapter 1

Introduction

It is a bit surprising to the neophyte turbulence researcher the extent to which open questions remain in this field. After all, the governing equation for this pervasive phenomenon has been known for the better part of two centuries:

$$\frac{\partial \vec{v}}{\partial t} + (\vec{v} \cdot \vec{\nabla}) \vec{v} = -\frac{1}{\rho} \vec{\nabla} P + \nu \nabla^2 \vec{v} \quad (1.1)$$

in which ρ and ν are the density and kinematic viscosity of the fluid, respectively. This equation, known as the Navier-Stokes equation [1], along with the incompressibility condition,

$$\vec{\nabla} \cdot \vec{v} = 0, \quad (1.2)$$

and boundary conditions provide a complete description of turbulent flows in incompressible fluids. It is for neither lack of motivation nor lack of effort that many

issues remain unresolved. A brief look around the natural world turns up hundreds of examples of turbulent flows, which influence our lives in immeasurable ways. Countless engineering applications, on modest and grand scales, involve turbulent flows, and a review of the literature reveals research efforts nearly as diverse and numerous as the flows themselves.

To be sure, one reason that a complete understanding of turbulence continues to be elusive is the sheer complexity of turbulent flows. Equally important, though, is that the very idea of a “complete understanding” is ambiguous in this case. Would an accurate statistical model of turbulence at all scales complete the task? With advances in computing power, turbulent solutions to Eqs. 1.1 and 1.2 may someday be computed or simulated accurately (and already has been solved for $Re < 10,000$)—would that count? With so many researchers approaching the problem from so many directions, it seems inevitable that some coherent picture of fluid turbulence will be formed. In the absence of analytical solutions representing turbulent flows to the Navier-Stokes equation, this picture will largely develop from improved numerical analyses and advances in flow measurement technology. It is in the latter category that the research we present here falls.

Section 1.1 includes brief overview turbulence and introduces some important questions on which we hope to shed light with these new measurements. Section 1.2 gives a review of some modern flow measurement techniques and experimental results. We briefly discuss key numerical methods and results in Section 1.3. In Section 1.4, we outline the rest of this thesis.

1.1 Background and Theory

1.1.1 Turbulence, Turbulence Everywhere...

It would be hard to overstate the importance of turbulent flows to human life and endeavor. The earth's oceans and atmosphere, both highly turbulent fluid systems, provided the necessary environment for the evolution of life. We quite literally spend our entire lives immersed in turbulent flow. A complex system of currents throughout the oceans mixes hot and cold and salty and fresh water and helps to mediate the climate [2]. That the atmosphere exhibits strong turbulence is apparent to anyone who has ever pondered the complex structure of clouds, seen a swirling whirlwind whip up dust, or relied in vain on a long-term weather forecast. In fact, a classic work by Edward Lorenz [3] in 1963 underlying the extreme complexity of atmospheric flows served as a seed for the development of the theory of chaos.

The importance of turbulence in engineering applications is equally widespread, with both positive and negative effects. Many industrial applications, such as chemical processing and sewage treatment [4, 5], rely on the ability to effectively mix components. Turbulence in mixing systems greatly improves their efficiency [6, 7]. On the other hand, turbulence in pipe flows can greatly increase the required pumping power at great expense to industry. Sometimes, the results of turbulence can be catastrophic. On November 12, 2001, an American Airlines flight crashed in New York, killing all 260 people on board. News reports [8] said the flight "had two abnormally stiff encounters with turbulence within 20 seconds of each other...the second encounter...may have proved deadly." An understanding of the significance

of turbulence has driven researchers to explore the phenomenon for centuries. (A number of useful review articles and reference books offer background into turbulence research and theory [9]–[14].)

Half a millennium ago, Leonardo DaVinci turned his scientific eye towards turbulence, producing perhaps the first detailed sketches of turbulent flows. But, turbulence entered the modern era with the work of Osborne Reynolds [15, 16], who provided a base from which turbulence research has grown and spread. In studying the onset of turbulence, he formed a non-dimensional number, now known as the Reynolds number, which compares the advective forces in the fluid to the dissipative forces:

$$Re = U\ell/\nu, \tag{1.3}$$

where U and ℓ are characteristic length and velocity scales. Re can be used to non-dimensionalize Eq. 1.1, putting it in the familiar form:

$$\frac{\partial \vec{v}'}{\partial t'} + (\vec{v}' \cdot \vec{\nabla}') \vec{v}' = -\vec{\nabla}' P' + \frac{1}{Re} \nabla'^2 \vec{v}'. \tag{1.4}$$

Here, the variables \vec{v}' , t' , $\vec{\nabla}'$, and P' are non-dimensional. Turbulent flows are represented by high Re solutions to this equation, such that the viscous damping term is small compared to the non-linear terms.

1.1.2 Energy Dissipation and Turbulent Cascades

Turbulent fluid motions are produced by the energy put into a system. If the input of energy is ceased, the fluid will eventually return to a laminar flow state and then come to a stop. This energy dissipation takes place due to the viscous conversion

of mechanical energy to heat. The local energy dissipation (per unit mass) ϵ in a turbulent flow is a function of the local strain components:

$$\epsilon = \frac{\nu}{2} \sum_{i,j} \left(\frac{\partial u_i}{\partial x_j} + \frac{\partial u_j}{\partial x_i} \right)^2 \quad (1.5)$$

The fact that energy is put into a system at large scales and dissipated at much smaller scales leads naturally to the idea of an energy cascade. This idea is attributed to Richardson [17], known best from Kolmogorov's formulation [18, 19], and is still an important concept in modern turbulence theory. Richardson was inspired to compose a short rhyme describing the process:

*Big whirls have little whirls,
That feed on their velocity;
And little whirls have lesser whirls,
And so on to viscosity.*

In his 1941 theory (K41), Kolmogorov laid out the following picture. Energy is introduced into a system at a rate ϵ in large scale eddies of some scale ℓ_0 . These eddies break into smaller eddies, which break into still smaller ones in a cascade which carries energy down to small scales. The energy cascades downward in scale at the same rate ϵ as it enters the system. These intermediate length scales are referred to as the inertial scales. At a sufficiently small scale, the cascade ceases, the flow is smoothed by viscosity, and energy is dissipated as heat (once again, at a rate ϵ). This scale at which dissipation occurs, defined by the local $Re = 1$, is known as the Kolmogorov length scale:

$$\eta = \left(\frac{\nu^3}{\epsilon} \right)^{1/4}. \quad (1.6)$$

K41 included two hypotheses relating to turbulent flows at small scales (for very high Re): (1) Statistical properties are universal and fully determined by ϵ and ν , and (2) the motion is statistically isotropic. Within the inertial range, K41 predicted an energy spectrum of the form $E(k) \propto \epsilon^{2/3} k^{-5/3}$, with $\epsilon = \Delta U^3/\ell$, where ΔU is the velocity difference measured across length ℓ .

1.1.3 Intermittency

K41 is a statistical picture based upon the average energy dissipation. At dissipative length scales, though, quantities such as the dissipation undergo large local fluctuations, bursting sporadically to values many times their mean, a characteristic known as intermittency. In keeping with the tradition of Richardson, I offer the following short verse:

*In a cascade that's turbulent,
The energy flux that fills all spaces,
At smaller scales is intermittent,
And localized in smaller places.*

Batchelor and Townsend [20] discovered experimentally that at small scales, the energy dissipation rate ϵ is not distributed evenly throughout space. Instead, ϵ is best taken as an average over a large space; there exist small regions of particularly high dissipation separated by larger regions of lower dissipation. Kraichnan [21] offered an early explanation of intermittency at dissipative scales, and Frisch and Morf [22] presented a detailed model of the phenomenon.

The distribution of ϵ (and other intermittent variables) at small scales has long been recognized as a key descriptive feature of turbulence. The exploration of intermittency in turbulence has led to a number of cascade models for turbulent flows, with different cascade models leading to different statistics for intermittent variables at dissipative scales. Kolmogorov's proposals [23] led to a log-normal distribution model (a gaussian distribution for the logarithm of a variable), a model not supported by experiments [24]. Mandelbrot [25] suggested a fractal model, and more recently, extensive work by Meneveau and Sreenivasan [26, 27] and many others has been done on multifractal models. The interplay between theory and experiment in this area offers hope for the development of a more complete model of turbulence. Improved dissipation-scale statistics from our three-dimensional measurement may serve to further refine cascade models.

1.1.4 Euler Singularities

As noted in the previous section, intermittent quantities occasionally burst to very high values. The sudden rise of these values naturally leads one to explore the possibility of finite-time singularities in the flow. More specifically, work has focused on the possibility of singularities in the 3-D Euler equation (from $Re \rightarrow \infty$ in Eq. 1.4:

$$\frac{\partial \vec{v}}{\partial t} + (\vec{v} \cdot \vec{\nabla}) \vec{v} = -\vec{\nabla} P. \quad (1.7)$$

Assuming a self-similar form for a singularity occurring at some time t_0 , one finds from dimensional arguments that gradient components must scale as $\partial_i v_j \propto (t_0 - t)^{-1}$.

From Eq. 1.5, it is clear that as $t_0 \rightarrow t$,

$$\epsilon \propto (t_0 - t)^{-2}. \quad (1.8)$$

With sufficient time resolution in a three-dimensional measurement, it might be possible to observe such a temporal dependence (see Chapter 4). In a real system, viscosity may provide a mechanism by which to cap the growth. Extensive analytical and phenomenological work [28, 29] and numerical work [30, 31, 32] on singularities in both Eq. 1.4 and Eq. 1.7 has been done.

1.1.5 Interplay of Vorticity and Strain

Examine briefly the 3×3 matrix of velocity gradients, \mathbf{M} :

$$M_{ij} = \partial v_i / \partial x_j. \quad (1.9)$$

We see (Eq. 1.5) that ϵ comprises a norm of the symmetric part (\mathbf{S}) of \mathbf{M} . A similar quantity, enstrophy Ω , is determined from the antisymmetric part (\mathbf{A}) of \mathbf{M} :

$$\Omega = \frac{1}{2} \sum_{i,j} \left(\frac{\partial u_i}{\partial x_j} - \frac{\partial u_j}{\partial x_i} \right)^2. \quad (1.10)$$

The enstrophy is a measure of the rotational energy in the system: $\Omega = \frac{1}{2} |\vec{\omega}|^2$, where the vorticity is $\vec{\omega} = \vec{\nabla} \times \vec{v}$. Rotating \mathbf{M} into a coordinate system in which \mathbf{S} is diagonal yields the form:

$$\mathbf{M} = \begin{pmatrix} \lambda_1 & \omega_z/2 & \omega_y/2 \\ -\omega_z/2 & \lambda_2 & \omega_x/2 \\ -\omega_y/2 & -\omega_x/2 & \lambda_3 \end{pmatrix}, \quad (1.11)$$

where ω_x, y, z are the components of the vorticity, and $\lambda_{1,2,3}$ are eigenvalues of the strain, and $\lambda_1 + \lambda_2 + \lambda_3 = 0$ for incompressibility. Undoubtedly, these two quantities, ϵ and Ω are closely related.

One interesting topic in turbulence that has arisen more recently is the presence of large-scale, coherent structures of vorticity and strain. Numerical simulations [33, 34, 35] have shown a tangle of “vortex tubes” throughout a turbulent flow system. The presence of such tubes, which may be as long as the integral scale of the flow, has been confirmed in many experimental systems [36, 37]. They appear to form in the presence of thin sheets on which both shearing and stretching (high- ϵ) are occurring. While local dissipation is low in the vortex tube, in both experiments and simulations, vortex tubes are associated with nearby sheets of high-dissipation [38]. The full significance of these coherent structures of high Ω and ϵ in turbulence is yet unknown. Our measurement technique has access to all components of \mathbf{M} and can be used to determine both quantities and study the interrelationship of the vorticity and strain fields.

1.2 Techniques of Flow Measurement

The highly complex spatio-temporal structure of turbulence, some aspects of which were discussed above, presents many challenges to its experimental study. Consider briefly the following simple example of a mixing system. A cup of water is stirred by a 3 cm spoon at speed of about 75 cm/s. The integral scale, at which the energy is introduced into the system, is $\ell_0 = 3$ cm. The Reynolds number, defined

by the spoon size and speed, is $Re = 22,500$. Vortices spin off the spoon, and energy cascades down to the Kolmogorov scale, $\eta \approx \ell_0 Re^{-3/4} = 16 \mu\text{m}$, so length scales over at least three orders magnitude are populated. The turnover time of the smallest scale structures is estimated from the Kolmogorov time scale, $\tau = 0.27 \text{ ms}$. Fortunately, several measurement techniques have been developed, many in the last two decades, which can offer significant insight into nature of such complex flows.

Ideally, an experimenter would like to have full access to all turbulent quantities in a flow at all locations and scales. While such access is becoming increasingly available in numerical simulations (see Section 1.3), there are more limitations in the laboratory. The complex nature of turbulence lends itself well to statistical analysis. And if the turbulent flow is homogeneous and isotropic at very small scales, as K41 suggests, studying the flow at a single point may offer information about the flow as a whole. Common techniques fall into a number of categories: Eulerian or Lagrangian, one-dimensional or multi-dimensional, single-point or whole-field, invasive or non-invasive, time-resolved or static, and many others [39]. We have developed a new measurement technique (Chapter 2) to study turbulent flows at dissipative length scales. This Eulerian technique is non-invasive and capable of measuring all velocities and velocity gradients at a point in a flow with good time resolution. In the following sections, we discuss those techniques and results which have motivated and guided the development of our new technique.

1.2.1 Single-Point Techniques (Eulerian)

One flow measurement technique which has long been a standard is hot-film and hot-wire wire anemometry (HWA). This technique is invasive; a very thin, temperature-controlled wire probe is inserted into the flow, and, via cooling, the flow speed transverse to the wire probe can be measured with high time-resolution. Confirmation of Kolmogorov's 5/3 law for inertial scales has been provided in numerous situations using HWA. To measure velocity gradients with a single hot-wire probe requires use of Taylor's hypothesis, which requires the mean flow U to be much larger than the turbulent velocity fluctuations, v' :

$$U/v' \gg 1.$$

Piomelli et al. [40] found Taylor's hypothesis to be suitably applicable to a boundary layer measurements with $U/v' \approx 5$. If this condition holds true, one can assume that small scale structures in the flow get swept by the probe faster than they change, and the temporal variations in velocity can be transformed into spatial variations via the relationship:

$$x = Ut.$$

One-dimensional approximations of the turbulent energy dissipation ($\epsilon \approx 15\nu(\partial v/\partial x)^2$) have been attained using measurements with single hot-wire probes in atmospheric airflows and in wind tunnels [28]. Statistics indicating intermittency from these experiments play an important role in the development of cascade models and point to the need for three-dimensional measurements of the dissipation and other intermittent quantities [41]. Spatial velocity structure functions have been measured using

two probes of variable separation.

One can avoid the need for Taylor’s hypothesis for cross-stream gradients, and increase the number of velocity components measured, by using an array of hot-wire sensors. While Park and Wallace found the measurement accuracy of four-sensor probes to drop significantly in flows with high shear [42], nine- and twelve-sensor arrays have been used with success by Wallace et al. [43, 44] and Tsinober et al. [45] amongst others for vorticity, helicity, and velocity gradient measurements in air flows. The twelve-sensor probe has higher accuracy for flows with a high cross-stream to streamwise velocity ratio [46] and has been used to measure vorticity fields in a high-shear mixing layer [47]. The majority of three-dimensional velocity gradient measurements to date have been made with using such hot-wire arrays. Still, the construction and calibration of such probe arrays is extremely difficult [46], and a non-invasive measurement technique is desirable.

An alternate local measurement technique is laser doppler velocimetry (LDV), invented by Cummins et al. [48]. This optical technique relies on the scattering of laser light off tracer particles in the flow [49]. Like HWA, LDV measures a single component of the velocity, but does not require calibration. Shifting the measurement location means simply shifting the illumination. Multiple flow components can be measured by illuminating with lasers of different wavelengths from different directions. With multiple probes, LDV can be used to measure spatial velocity gradients without relying on Taylor’s hypothesis [50].

A comparison by Wallace and Foss [51] of HWA and LDV vorticity measurements highlights the strengths and limitations of each. These two techniques

together point in the general direction of the development of this new measurement technique. As with multi-probe HWA, our technique can measure local velocities and velocity gradients directly. The optical nature of LDV, non-invasive and straightforward to calibrate, also provided an important model motivating this work.

1.2.2 Lagrangian Measurement Techniques

While the Eulerian techniques described in Sec. 1.2.1 observe a single location over a long period of time, Lagrangian techniques seek to track individual particles in time. Lagrangian flow measurements in turbulence are of great interest and importance, and new Lagrangian techniques have succeeded in measuring quantities previously accessible only via numerical simulation. One particular challenge of Lagrangian tracking techniques is the large range of spatial scales required, so low mean flow turbulence is preferable. Mordant et al. [52] used ultrasonic doppler tracking (a form of sonar) to track one component of a particle's velocity over a large range of times in the region between two counter-rotating disks. High-speed optical measurements of particle position in three dimensions were made by Bodenschatz et al. [53, 54] for the same geometry. The most obvious quantities which can be measured by tracking individual particles with good time resolution are velocity (a first derivative in time) and acceleration (a second derivative in time). Tracking a single particle, however, does not offer access to velocity gradients or, by extension, the dissipation. The Eulerian technique which we have developed can be used to find the acceleration and the dissipation simultaneously.

1.2.3 Particle Image Velocimetry

Particle image velocimetry (PIV) is perhaps the most widely used optical flow measurement technique. PIV in its basic form measures velocity fields in a planar slice of a flow [56]. Two images of tracer particles in the field are captured separated by a known time, and the double images are used to measure a velocity at each particle location. The measured velocity field is two-dimensional; that is, only two velocity components and four gradient components can be measured. Because so many particles can be imaged at once, the information density is high, and statistics can be easily gathered. In recent years, many forms of PIV have been developed that have added to its capabilities as a flow diagnostic.

Advances in digital imaging technology, specifically high-resolution digital video, has brought improvements in the time and spatial resolution of PIV measurements. Megapixel-resolution digital video cameras are now available with frame rates up to 1000 frames/s (with lower resolutions much faster), making temporal resolution of some turbulent flows practical. Additionally, μ PIV, essentially PIV under a microscope, has been used to analyze microscopic flow systems. To the best of our knowledge, PIV has not previously been used to measure microscopic velocity fields in a much larger flow.

Other forms of PIV have broken the two-dimensional barrier. In stereoscopic PIV, two cameras observe a two-dimensional field of particles from different angles. With this technique, all three velocity components and six gradient components are measured. Velocity gradients transverse to the measurement plane remain inac-

cessible. A more elegant, and significantly more complex technique is holographic PIV (HPIV). Using the principles of holography along with those of PIV, HPIV is a fully three-dimensional technique. The 3-D velocities of particles within an illuminated test volume are measured. The small-scale resolution of HPIV is quite good. Tao et al. [37, 57] applied HPIV to channel flows to provide an unprecedented look inside a turbulent flow. A cinematographic form of HPIV has the potential to yield time-resolved measurements, but the sampling rates necessary have not been achieved.

In the next chapters, we describe the development and application of a new fully three-dimensional PIV technique, 3-D LH μ PIV, and its application to two types of turbulent flow. Table 1.1 shows a comparison of flow velocimetry techniques (adapted from [58]).

1.3 Numerical Work and Results

Paralleling the advances in flow measurement capabilities has been a dramatic increase in the use of computers for flow modeling and analysis. Turbulent fluid flow is a deterministic system; given Eqs. 1.1 and 1.2 and sufficient knowledge of the initial conditions, it is possible, if only in theory, to fully describe the system at later times. Such calculations are highly sensitive to initial conditions. While such knowledge of a flow system is infeasible in a laboratory situation, it has been done numerically with constantly increasing accuracy. Direct numerical simulation (DNS) refers to flow simulation in which there is full spatio-temporal resolution of all relevant scales,

Measurement Technique	Velocity Components	Gradient Components	Time-Resolved	Taylor's Hypothesis	Invasive
HWA	1	1	yes	yes	yes
Multi-probe HWA	3	9	yes	yes	yes
Ultrasound	1	1	yes	no	no
LDV	1	1	yes	no	no
3-D LDV	3	3	yes	no	no
PIV	2	4	yes	no	no
Stereoscopic PIV	3	6	yes	no	no
HPIV	3	9	no	no	no
3-D LH μ PIV	3	9	yes	no	no

Table 1.1: Comparison of velocimetry techniques. The technique developed in this research (3-D LH μ PIV) has the distinction of being the only three-dimensional, non-invasive, time-resolved technique currently in use.

from the integral scale down to the dissipation scale. With DNS, all turbulent quantities in the flow can be determined. But DNS is as costly as it is powerful, with the computational work required to resolve the flow increasing as Re^3 . Even at lower Re , DNS has proved to be a valuable tool. Chen, Sreenivasan, and Nelkin used DNS to explore the scaling of ϵ and Ω for homogeneous isotropic turbulence [59]. Their results are compared with our experimental results in Chapter 4. Flow structures resolved in simulations, such as the vortex tubes and high-dissipation sheets discussed in Sec. 1.1.5, have later been observed in the lab and provide a framework for understanding experimental data.

Numerical simulations run into problems if singularities (or near singularities) of the form in Eq. 1.8 exist. Direct numerical simulations must resolve length scales over a range $\sim Re^{-3/4}$. However, in close proximity to a singularity ($t \rightarrow t_0$), the smallest spatial scales go to zero as $(t_0 - t)^\alpha$ ($\alpha \geq 1$). Without being able to resolve the rapidly shrinking smallest scales, a simulation is likely to break down in the presence of a singularity.

One method of circumventing computation-hungry DNS is Large Eddy Simulation (LES), used for many engineering applications. In LES, only the large scales of the flow are directly calculated; smaller scales are estimated based upon some appropriate statistical model. Hence, LES requires much less computing power than DNS, but unlike DNS, it requires some a priori knowledge of small-scale turbulent behavior. A detailed experimental picture of the flow at small scales, as our measurement technique provides, can improve the realism of LES.

1.4 Dissertation Outline

As detailed in the previous sections, significant questions remain about the behavior of turbulent flows even as new measurement techniques help create a more detailed picture than ever of turbulence. We have applied a new technique, long-range, high-speed micro-PIV (LH μ PIV) to two types of flow: oscillating grid turbulence and turbulent Rayleigh-Bénard convection. These particular flows were chosen because they have low mean flow, could be produced in a single system, and they represent two very different turbulent flow paradigms. Grid-generated turbulence is nearly homogenous and isotropic [60, 61], perhaps the closest one can get in turbulence research to a “basic” model. One hopes to gain a general understanding of turbulent flows from measurements in grid turbulence. Turbulent convection, on the other hand, is a field unto itself (see review by Siggia [62]). Driven by thermal density variations and gravity, this flow system is clearly non-isotropic. Many real-world systems, including the oceans and the atmosphere, are driven by turbulent convection. Measurement techniques, including our own, are complicated by the thermal fluctuations in convection. Others, such as hot-wire anemometry, cannot be applied to such a system because it has very low mean flow. In addition to studying these two flows independently, we present a comparison of their statistics.

Chapter 2 covers the design and development of the LH μ PIV system. The theoretical framework for the measurement, its setup, and its calibration are detailed. In Chapter 3, the design and setup of the two flow systems are described. Chapter 4 contains the results and analysis from the experiments with both systems.

The two are discussed separately, with an emphasis on grid-generated turbulence. The statistics and interrelationships of enstrophy and dissipation are discussed. In addition, individual high-dissipation events are analyzed for evidence of finite-time singularities. The statistics of the two turbulent systems are compared. Chapter 5 summarizes the current work. Suggestions for future measurements and analysis are also discussed. Relevant analysis and software is included in the Appendix.

Chapter 2

Technique Development and Application

Our goal in these experiments was to measure velocities and velocity gradients in three-dimensions in a turbulent flow. Myriad technologies for flow measurement have been developed in recent years, which offer access to different physical quantities and range from one-dimensional to three-dimensional. Still, we knew of no technique which provided the proper combinations of parameters to suit our requirements: temporal resolution, spatial resolution at small scales, non-invasiveness, ability to measure flows with low mean velocity, and full three-dimensionality. We chose to develop a modified version of particle image velocimetry (PIV), a common optical particle tracking method. The result is a novel technique which we termed three-dimensional, long-range, high-speed, micro-PIV (3-D LH μ PIV).

This chapter details the development of 3-D LH μ PIV and its application to two

turbulent flows. In Section 2.1, we introduce the theory behind this measurement technique. Section 2.2 details the optical and imaging system, including tracer particles, illumination, and cameras. The control system is described in Section 2.3, and the digital analysis of the video data, through which the velocities and gradients are determined, is covered in Section 2.4.

2.1 Measurement Theory

In PIV measurements, the fluid is seeded with small particles that track the flow. These particles are illuminated with a laser sheet (a planar beam), and images of the particles are captured by a camera at two different times. The shift of the particle images between frames is used to measure velocities. In this fashion, a two-dimensional slice of the flow is imaged, and one can measure two velocity components (of three) and four velocity gradients (of nine).

In order to extend this basic PIV framework to measure the flow in all three dimensions, we essentially multiply it by three. That is, instead of a single laser sheet and camera, three camera-laser sheet pairs are used, each perpendicular to the others. With three orthogonal views, all three velocity components and nine gradients can be measured. However, for such a system of cameras to actually measure corresponding velocities and velocity gradients and not three independent two-dimensional slices, the cameras must be carefully aimed to record within the same small volume of flow. Around any origin, the flow can be written as the Taylor

series expansion:

$$\vec{v} \approx \vec{v}_0 + \mathbf{M} \cdot \vec{x} + \dots, \quad (2.1)$$

where \vec{v}_0 is the velocity at the origin, \vec{x} is the displacement vector from the origin, and \mathbf{M} is the matrix of velocity gradients, $M_{ij} = \partial v_i / \partial x_j$. Below a particular length scale, the first-order approximation of Eq. 2.1 (the first two terms in the Taylor expansion) is sufficient to describe the flow. The scale at which the flow is smooth and the linear approximation valid corresponds to the Kolmogorov length scale η discussed in Chapter 1.

Though looking in the same volume of flow, each camera must see only those particles in its own laser sheet. To achieve the proper alignment, each laser sheet illuminates one face of an (imaginary) cube within the flow of size $\sim \eta$. Any two laser sheets cross along one edge of the cube, and all three sheets cross at one vertex of the cube. Each camera is aimed at one face with the vertex and sides just outside the field of view and measures velocities in a plane perpendicular to the other two (Fig. 2.1). An array of velocity vectors is measured on each of the three illuminated faces of the cube. These two-dimensional vectors and their position in 3-space are then fit to the linear model of Eq. 2.1 to determine \vec{v}_0 and \mathbf{M} (see Sec. 2.4).

2.2 The Optical System

Though straightforward, putting the above measurement theory into practice requires a carefully designed optical system. This system includes the particles, laser illumination, cameras, and all associated optics.

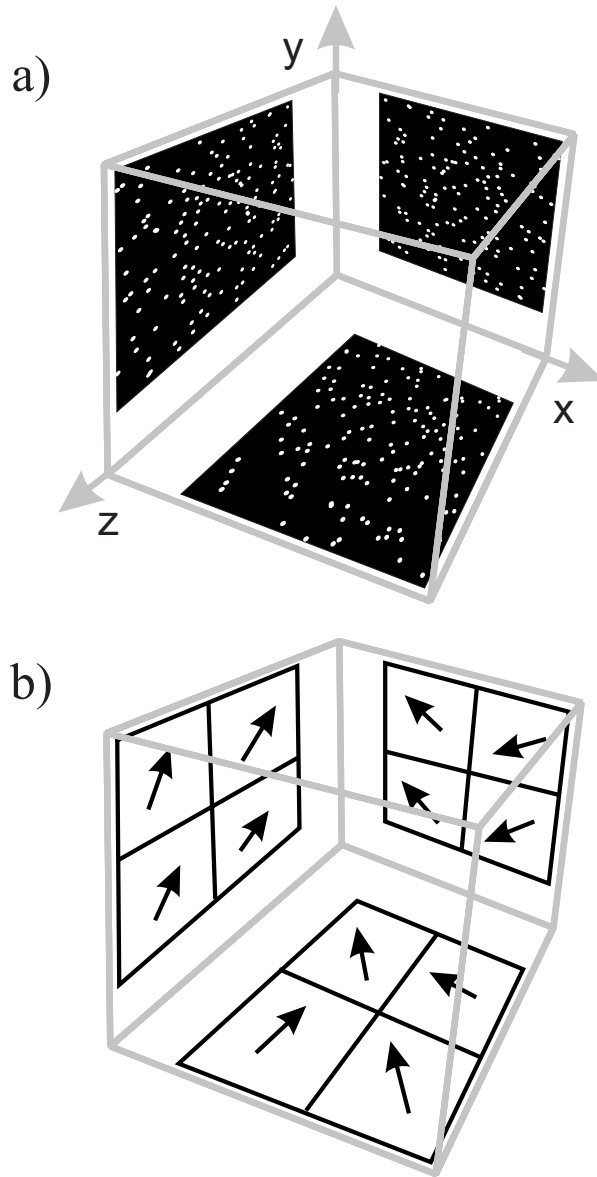


Figure 2.1: a) Three laser sheets illuminate three faces of a cubical volume within the flow. Each camera sees a two-dimensional particle field on one of the three faces. The fields of view for the three cameras are offset from the vertex of the cube. Particles within the cube and on the remaining three faces are not visualized. b) After being broken into subsections and digitally analyzed, each face yields an array of two-dimensional velocity vectors to be fit to a three-dimensional model.

2.2.1 Tracer Particles

A number of considerations were taken into account in choosing the size of the particles. The desired tracer particle size can be roughly estimated by the resolution of the imaging system. In our case, at maximum magnification (to image the smallest possible flow volume), an approximately $5\mu\text{m}$ region of flow is imaged onto one pixel of the camera's CCD chip. As there are no imaging benefits to seeding with particles which are much smaller than a single pixel, only polystyrene spheres with diameters of $9\mu\text{m}$, $3\mu\text{m}$, and $1\mu\text{m}$ were tested. As mentioned in Sec. 2.1, the spheres are illuminated by laser light scattering. Due to physical restraints and ease of design, the scattered light was viewed at a 90° angle relative to the propagation of the laser sheet, an angle that is, unfortunately, the minimum for scattered light intensity. The amount of light scattered scales as r^{-2} , where r is the radius of a particle. For illumination purposes, then, the larger particles are clearly better. However, the density of particles (particle number per volume) with which the flow can be seeded scales as r^{-3} for a set volume of particles in the flow. A higher particle density improves velocity measurements. Another factor considered in choosing a particle size was settling. The polystyrene spheres have a density of 1.05 g/mL and are nearly neutrally buoyant in water but do slowly settle out of the flow over a few days. Since one camera images through the bottom of the tank, particle settling can cause significant optical problems.

We use $1\mu\text{m}$ fluorescent spheres from Duke Scientific Corporation at an approximate density of 3×10^6 particles/mL. The particles are embedded with fluores-

cent dye that absorbs light at a peak wavelength of 542 nm (green) and emits light at 612 nm (red-orange). In actuality, these particles scatter much more green light (our laser emits at 532 nm) than they fluoresce, and primarily scattered light is used for imaging. However, the fluorescence does offer a few important benefits. Unlike scattered light, the fluoresced light is emitted equally in all directions, potentially increasing the light per particle which reaches the camera. Also, the red-orange light emitted by the particles can be seen clearly through goggles which filter out the very bright green light background, allowing for easy visual inspection of the flow. Figure 2.2 shows a sample image of tracer particles in water.

2.2.2 Laser Illumination

In making a PIV measurement, it is important to “stop the action” —that is, particle images should be captured as dots and not as streaks. A pulsed laser source, which illuminates the particles for only a small fraction of the frame exposure, serves this purpose in many standard PIV systems. Our technique was designed to be time-resolved with frame rates high enough to temporally resolve the flow. Our frame rates and shutter speeds are sufficient to stop the action without using a pulsed light source. Hence, a Spectra-Physics Millennia Vs 5 W cw doubled Nd:YVO₄ laser is used for illumination. This laser emits a green beam of wavelength 532 nm with a diameter of 0.23 cm.

The single beam from the laser is used to produce all three laser sheets. The beam is prepared with a series of optical components before separating it into three

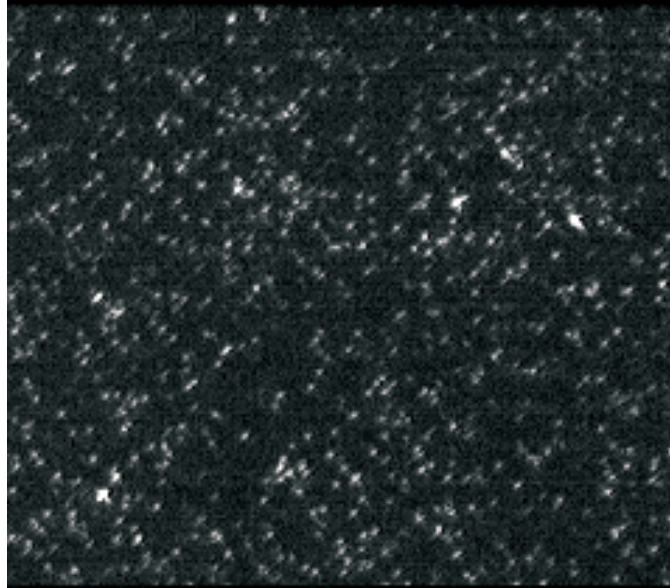


Figure 2.2: Sample camera image of $1\ \mu\text{m}$ polystyrene spheres suspended in the flow. The particles are illuminated by a laser sheet $0.018\ \text{cm}$ thick in a plane perpendicular to the viewing angle. The resolution of the image is 240×210 pixels, corresponding to a region of flow $0.11\times 0.10\ \text{cm}$. Approximately 450 particles are visible in this image.

parts. Upon exiting the laser cavity, the light is linearly polarized. It is passed through a quarter waveplate ($1/4\lambda$) whose major axis is rotated at a 45° angle relative to the polarization axis of the beam. In this manner, the beam becomes circularly polarized, a state which is preferable for the beamsplitters used later. Next, the beam is expanded to a diameter of 0.8 cm using a Galilean telescope consisting of a plano-concave lens and a plano-convex lens. This telescope expands the beam without passing it through a focus. If the light is narrowed to a focal point, small dust particles moving through that point cast shadows on the entire illumination system. Though the beam is later focused down in one direction to create laser sheets, it remains 0.8 cm wide in the other direction to ensure that the full field of view of the camera is illuminated. After expansion, the beam is elevated to the height of the platform on which the remaining optical components are mounted.

Two plate beamsplitters are used to divide the beam into three parts. The actual transmission and reflection coefficients of the beamsplitters are highly sensitive to the incident angle of the incoming beam for linearly polarized light. For circularly polarized light (essentially random polarization), the beamsplitters work at their specified coefficient ratios. The beam first strikes a beamsplitter which reflects 70% and transmits 30% of the incoming light (70R/30T). The reflected beam strikes a 50R/50T beamsplitter which equally divides it in two. In this way, the initial beam is divided into three beams of equal size and roughly equal intensity, each of which will provide illumination for one camera.

Prior to entering the turbulent flow, each beam passes through a plano-convex

(converging) cylindrical lens. These lenses do not produce planar laser beams. Instead, they narrow the beams to a thin waist in one direction (Fig. 2.3). The wavelength, lens focal length (50 cm), and incoming beam size can be used to estimate the thickness of the waist d_0 :

$$d_0 = 4\lambda/\pi\theta \approx 4\lambda f/\pi r,$$

where $\lambda = 532$ nm is the wavelength of the light, θ is the angle of the narrowing beam, $r = 0.4$ cm is the beam radius at the lens and $f = 50$ cm is the focal length of the lens. It is near this waist that the beams are actually laser sheets and the cameras are aimed. The lenses are in vertical rotation mounts to allow fine rotation of the sheets and can move horizontally on optical rails to change the location of the beam waist relative to the measurement volume. Additionally, each focused beam is reflected off two aiming mirrors, so the sheets can be very precisely positioned for measurements. These mirrors also steer the laser beams up and over the optics for the cameras.

The actual location of the waist relative to the measurement volume must be chosen carefully. If the laser sheet is too narrow, tracer particles with any motion perpendicular to the sheet will pass through it too quickly to be imaged twice. At the waist, this effect can be seen by eye. The particles appear to twinkle and no motion can be discerned. If the sheet is too thick, however, the region of the flow being imaged is not sufficiently two-dimensional. In this case, differential motion between the foreground and background can be seen on the video displays. With limited laser power, another factor must go into choosing how close to the waist

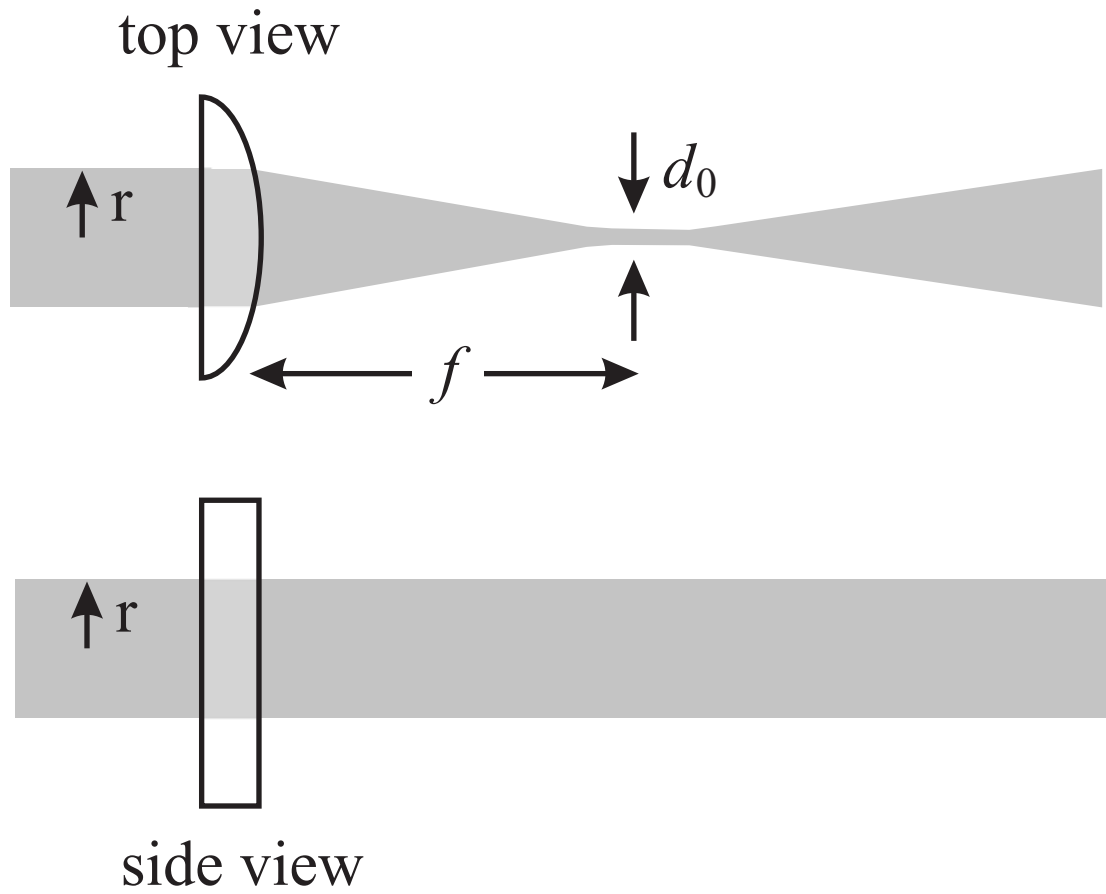


Figure 2.3: Cylindrical converging lenses are used to create laser sheets. A beam passed through the lens narrows to a thin waist before expanding again. By looking at particles in the region of the waist, a camera sees a two-dimensional slice of the flow.

to observe the flow. At the waist, each particle is illuminated with light of greater intensity, but fewer particles are illuminated. As the view moves farther from the waist, the number of particles illuminated goes up as the brightness per particle drops accordingly. We achieved good measurement results by aiming the cameras at the laser sheets at a distance of 3.5 cm from the waist. At this point, the sheets are 0.018 cm thick.

2.2.3 Video Cameras

Three Redlake PCI 2000S high-speed video cameras are used to image the illuminated tracer particles. The PCI 2000S has a maximum frame rate of 2000 frames/s. The CCD has $7.4 \mu\text{m}$ square pixels with a maximum resolution of 480×420 pixels. Frame rates higher than 500 frames/s are achieved by imaging only a subset of the CCD so have lower resolution. At frame rates lower than 500 frames/s, an “extended record” option allows for lower resolution (240×210 pixels) to be used. This option is useful because it allows a smaller region of flow to be imaged while increasing the maximum recording time by a factor of 4. Since the camera has a fixed amount of memory, the maximum record time varies with both speed and resolution (Table 2.1). The recording parameters are chosen so as to get good time-resolved data for the specific flow being studied. In addition to being able to vary the frame rate, the shutter speed of the cameras can be varied down to $1/40,000^{\text{th}}$ s. Lowering the shutter speed allows the motion of the particles to be stopped without needlessly increasing the frame rate. The CCD has a bit depth of 8, corresponding to 256

Frame Rates	Pixel Resolution	Max. Record Time (sec)
60	480×420	8.5
60E	240×210	34.2
125	480×420	4.1
125E	240×210	16.4
250	480×420	2.0
500	320×280	2.0
1000	240×210	2.0

Table 2.1: Frame rates, pixel resolution, and maximum record time for the Redlake PCI 2000S camera.

levels of grey. The cameras were assembled without the standard UV filter, greatly improving their low-light sensitivity. As is common with CCD imagers, bright light “bleeds” from an overexposed pixel to neighboring pixels.

A long-distance microscope lens, Infinity KV model with a CFV-1 objective from Infinity Photo-Optical Company, is connected to each camera using a standard video c-mount. These lenses have a working distance of 33–127 cm for a magnification range of 1.5×–0.35×. In order to image the smallest possible region of flow, the lenses are used at the low end of the working distance range, 43.3 cm. At this distance, the spatial resolution of the video images is 5 μm /pixel, giving a field of view of 0.23×0.20 cm at full resolution and 0.11×0.10 cm at 240×210 pixels, the resolution we used in many of our experimental runs. For maximum light, the lens apertures are kept fully open at all times. The focus of the lenses is adjusted with

the manual focusing rings.

An estimate of the depth-of-field of the cameras-lens system was found experimentally using a target consisting of tracer particles on the surface of an acrylic block. The target was mounted on a fine-adjust translation stage with micrometer control and illuminated with the laser at low power. With the camera at a typical working distance, the suspended particles were brought into focus on screen. The translation stage was then moved back and forth from the optimal focus so that the particles went in and out of focus. Though there is no sharp transition in focus, the range over which the particle images are sufficiently clear can be estimated. With this method, the depth-of-field was found to be 0.25 cm. In the experiments, the depth-of-field is actually set by the thickness of the laser sheet used for illumination.

2.2.4 System Alignment

The cameras must be carefully aimed relative to the crossing point of the three laser sheets. Three rotating mirror mounts were used for this purpose. Each camera faces parallel to the walls of the tank at an aiming mirror that is positioned very close to 45° relative to the wall of the tank, so that the camera looks through the wall of the tank at a right angle. The mirror can be rotated around both horizontal and vertical axes using two independent micrometer controls while the center of the mirror remains stationary. Two cameras look in horizontally through two adjoining sides of the square tank. Each of these cameras faces a vertical laser sheet which originates above the other camera. The camera which looks in vertically through

the bottom of the tank faces a horizontal laser sheet which crosses the tank at a sharp angle relative to the sides (Figure 2.4). Hence, the planes formed by the laser sheets are the same as the focal planes of the three cameras.

Once this rough alignment is established, the cameras and sheets must be finely aligned relative to each other. The laser is turned on, and the cameras are connected to external video monitors. The focus on one camera is adjusted to bring the tracer particles in its laser sheet into clear focus, with the sheet centered vertically in the camera's field of view. The laser sheets for the other two cameras are positioned so that they also appear in the field of view of the first camera (as bright horizontal and vertical lines) then are repositioned left and down to be just outside the field of view (Figure 2.5).

The focus and alignment of the second camera is adjusted to bring tracer particles in its sheet into focus, and that sheet is vertically centered in the field of view. Once again, the two laser sheets from the other cameras are placed just off-screen to the left and bottom, this time by adjusting the aiming of the camera and not the sheets themselves. This process is then repeated for the final camera and laser sheet. The resulting alignment ensures that the three cameras views are orthogonal and offset equally from a well-defined origin. The full optical setup is shown in Figures 2.6 and 2.7.

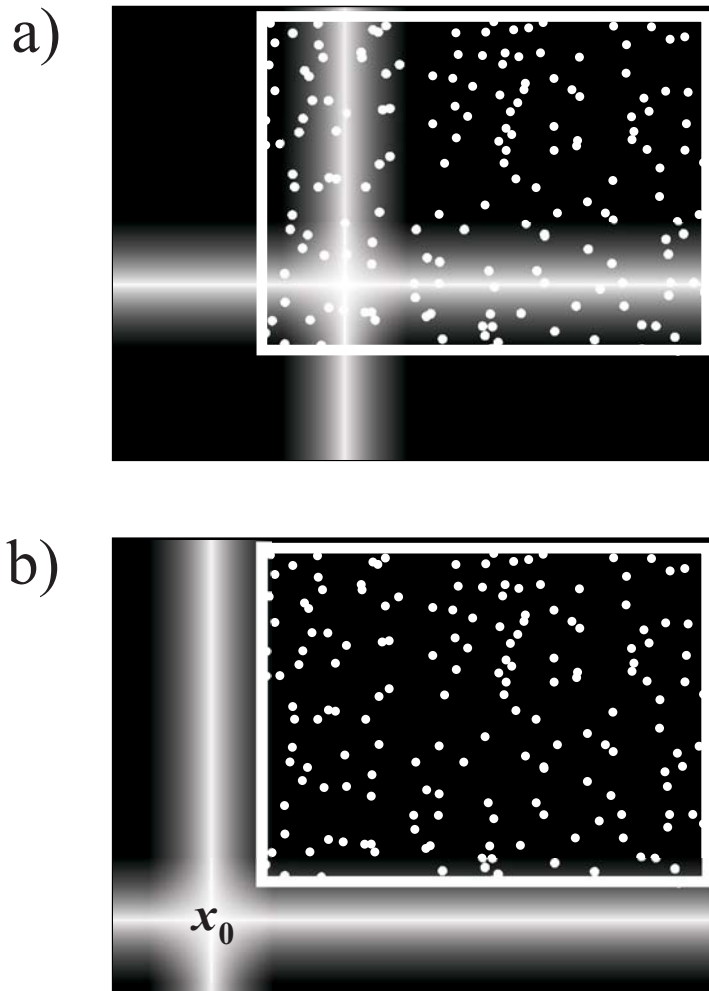


Figure 2.5: Camera alignment procedure. a) To align camera 1 with the other two cameras, its field of view is positioned such that the laser sheets for cameras 2 and 3 are visible on screen. The thick white box shows the field of view of camera 1. b) Then, the field of view is repositioned so that the laser sheets for cameras 2 and 3 are off-screen to the left and down. This process is repeated for cameras 2 and 3. The point x_0 where the three laser sheets cross is shown at the bottom left. Positioning each field of view to be offset from x_0 guarantees that each camera sees only those particles in its own laser sheet. The linear model is fit around the origin x_0 .

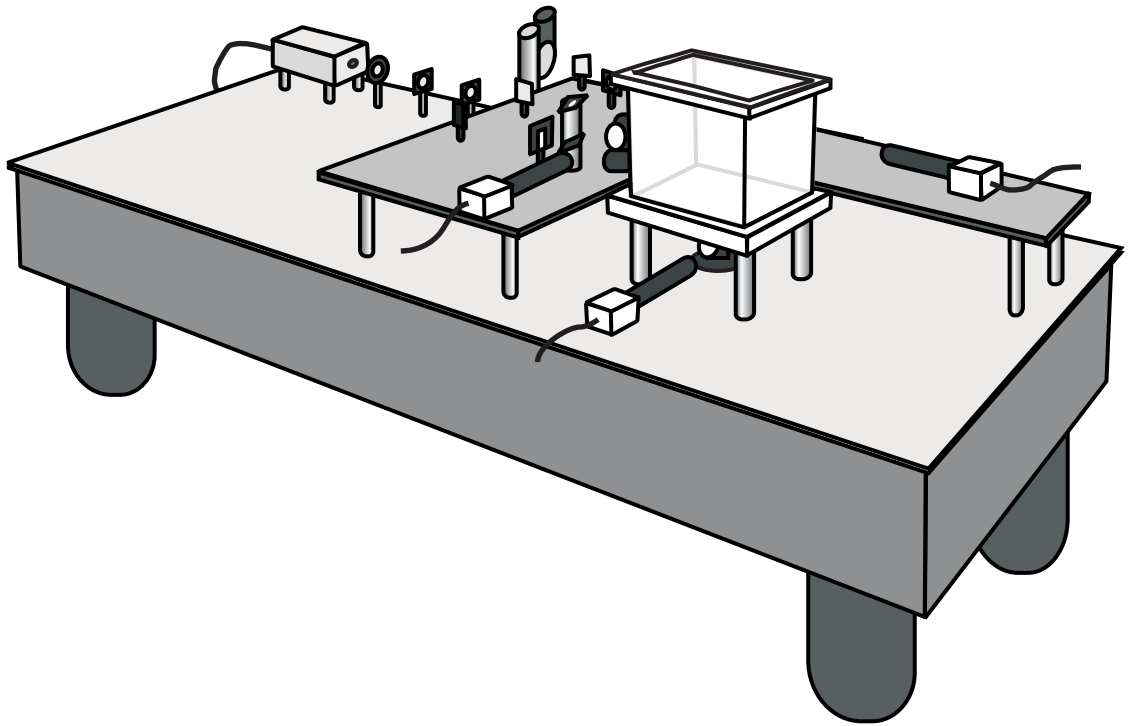


Figure 2.6: 3-D view of the tank and optical setup. The laser optics and two cameras are mounted on a raised platform to bring them level with the tank. The third camera is mounted on the optical table and faces vertically upward through the bottom of the tank.

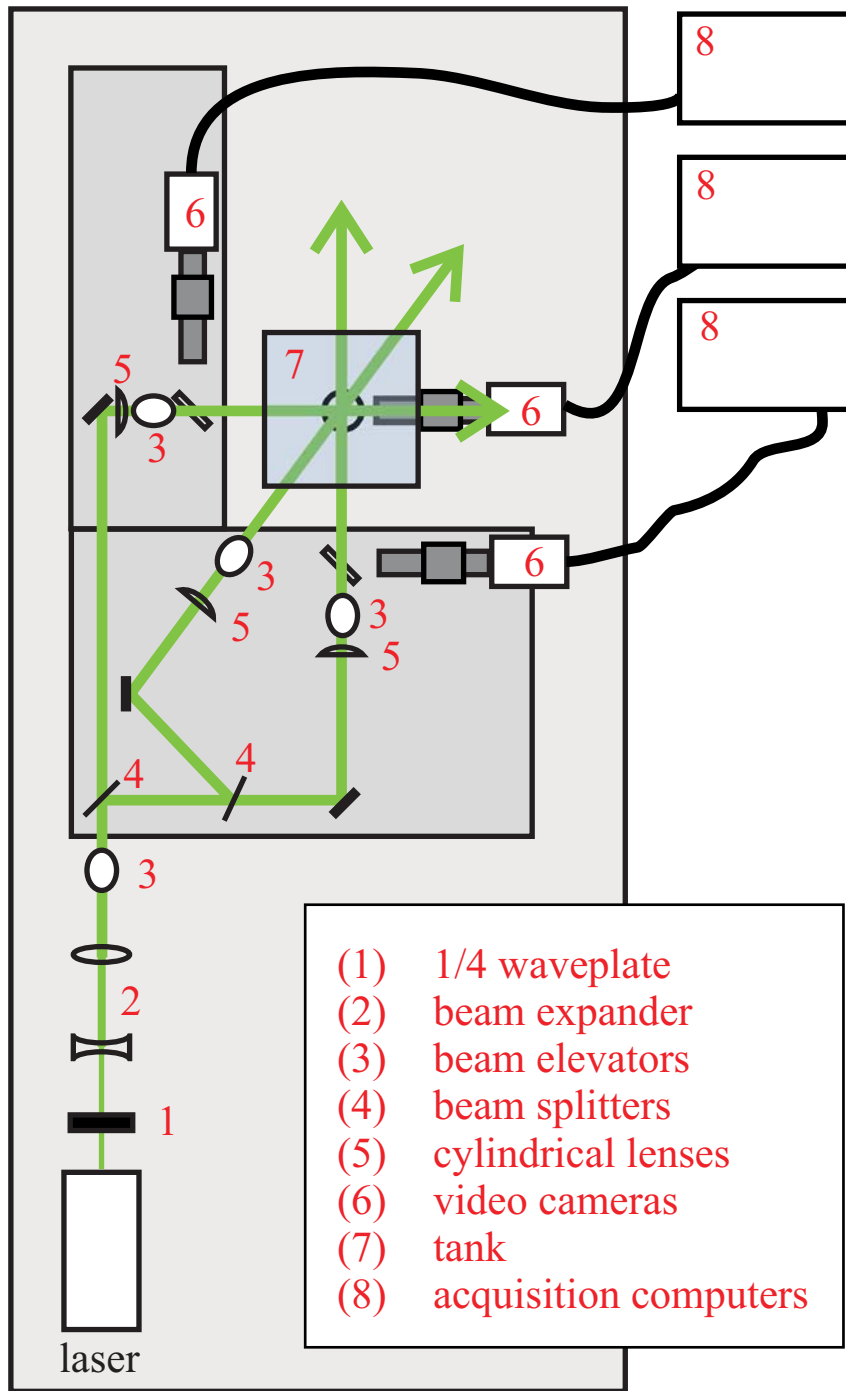


Figure 2.7: Top view of the optical setup.

2.3 The Control System

2.3.1 Video Recording

Each camera is connected to its own computer (Pentium III, 550 MHz) via a PCI card. In addition to the PCI connection, the camera cables have a bundle of connectors that include those for external video monitoring, external triggering, and synching. Video data is not displayed on the computer monitor while it is recorded, so we use external monitors to observe the flow state. While recording, video data is continuously spooled into the on board memory of the PCI card. The camera memory consists of a single 100 MB DRAM module. Video data in the memory is constantly overwritten in a loop. When recording is stopped, either via an internal or external trigger, the trigger settings determine which frames are saved. The trigger is set such that the frame being recorded at the time of the trigger becomes the last frame of the recorded sequence (Figure 2.8). Once the recording has been stopped, the data in the camera buffer must be fully saved to disk before recording a second sequence.

The number of frames saved (N) in a full memory buffer depends upon the resolution and frame rate settings for the camera. Since measurements are made using frame pairs, each set of three videos (one from each camera, recorded simultaneously), yields $N - 1$ data points, where one data point consists of a velocity and a gradient matrix. Time sequences are limited to these $N - 1$ points. For example, at 125 frame/s and 240×210 pixels, the maximum time sequence is 16.376 s long and contains 2047 data points. The video data for a set of three videos requires 300 MB

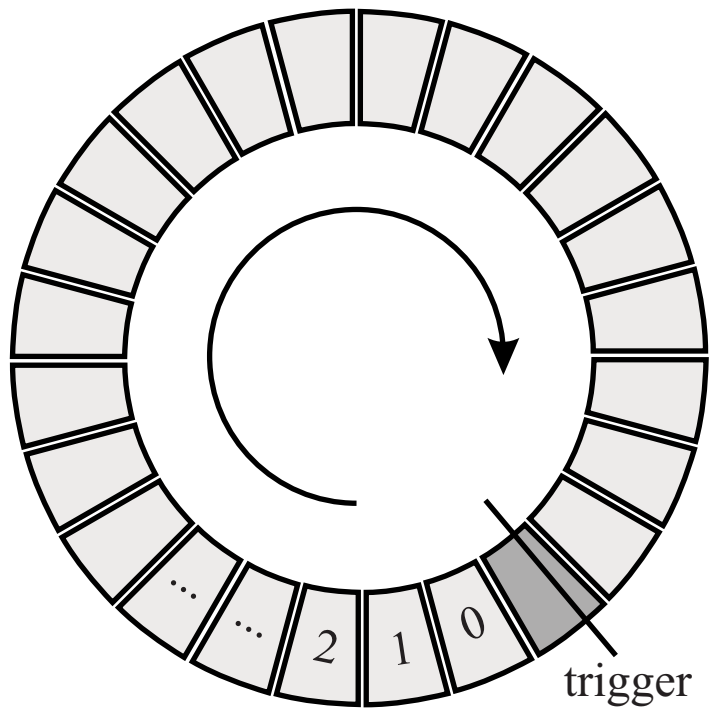


Figure 2.8: Schematic of the PCI 2000S camera memory buffer. Frames are recorded in a loop, overwriting previously recorded data. When a trigger is received, the recording stops (after completing the current frame), and the entire buffer is saved to disk.

of hard disk space. In order to gather a large statistical sample (5×10^6 points), thousands of video sequences must be recorded. To store all the video sequences for analysis would require disk space on the order of terabytes and, hence, would be quite impractical. In order to collect this much data, then, video data must be processed on-the-fly. That is, once a set of videos from the three cameras have been analyzed, they are deleted in preparation for the next set. The collection of millions of data points can easily require two days or more of recording and analysis. To handle the collection of large data sets and on-the-fly data processing, a control and automation procedure was developed.

The first step in the control system is the automation of data acquisition. The proprietary software bundled with the cameras does not allow for automated video recording. That is, each video must be saved and the recording restarted using mouse and keyboard commands. For automation, a digital video analysis software package, Xcitex's MiDAS, was used. MiDAS includes the same basic video controls (frame rate, shutter speed, etc.) as the Redlake software. It also offers an "auto record" feature. When using this feature, a base file name and saving location is set. Video is recorded until triggered to stop. As soon as the trigger is received, the recording stops, and the video is saved to the preset location with the base file name appropriately incremented. The recording begins again as soon as saving is completed and continues until another trigger is received. The process repeats until stopped manually.

2.3.2 Video Synchronization

In addition to being automated, the video data acquisition for the three cameras must be synchronized. There are two primary methods of synchronizing the video acquisition between cameras. With one method, one camera is assigned the role of the master, and the other two are slaves. Each time a frame is recorded on the master camera, a synch pulse from the master forces a frame to be recorded on each of the slaved cameras. This master/slave setup ensures that corresponding frames on each camera were recorded at the same time, and it is the preferable method. Unfortunately, the MiDAS software cannot accommodate master/slave synchronization between multiple computers. Instead, a second method of synchronization is used, which makes use of the external trigger pulse. All three cameras are set recording independently. An external pulse, produced by a digital delay/pulse generator, triggers the three cameras simultaneously to stop recording. After saving is complete, the three cameras automatically begin recording again and await another external trigger pulse. Unlike master/slave synchronization, the external trigger pulse does not force the frames from the three cameras to be recorded together. The cameras record independently, so a random time lag of up to one frame length exists between any two of the videos (Figure 2.9). These time lags change each time the cameras begin recording again after files are saved, and cannot be predicted. However, because frame rates which provide very good temporal resolution are used, the time scale on which the turbulent flow states change is much larger than the length of a single frame. (For our grid system, the Kolmogorov time scale, $\tau_k = (\nu/\epsilon)^{1/2}$ is 0.55

s.) For this reason, we assume in our analysis that the sequence of frames from each camera is synchronized with the other two.

2.3.3 PIV Analysis Automation

As soon as a set of videos is saved, PIV analysis of the data to measure velocities is immediately carried out. This computationally intensive analysis is described in detail in the next section. To bring the processing time down, video from the cameras is processed in parallel by three Silicon Graphics Octane computers running IRIX 6.5, a UNIX operating system. Each of these computers has a 250 MHz R10000 processor, and a 9 GB hard disk. The video transfer to the analysis computers is done over a 100 Mbit/s ethernet network with a multi-port 100 Mbit/s switch. The switch allows all three control computers to communicate with the analysis computers at 100 Mbit/s in unison. We created a shell script to automate the analysis (shown in full in Appendix A). The script runs continuously on the analysis computers, checking every second for videos of a preset size. When a full-size video file is found, the script runs the PIV analysis program. The analysis program writes velocity data out to a file. Upon completion, this file is sent to a seventh computer (a Silicon Graphics O₂ with a 300 MHz R5000 processor and 150 GB of hard disk storage) to be combined with that from the other two cameras, and the original video file is deleted. An option to keep the video data can be selected. During the analysis, the next video from the system can be saved to the hard disk. It is important, however, that the saving of the second video file not be completed until

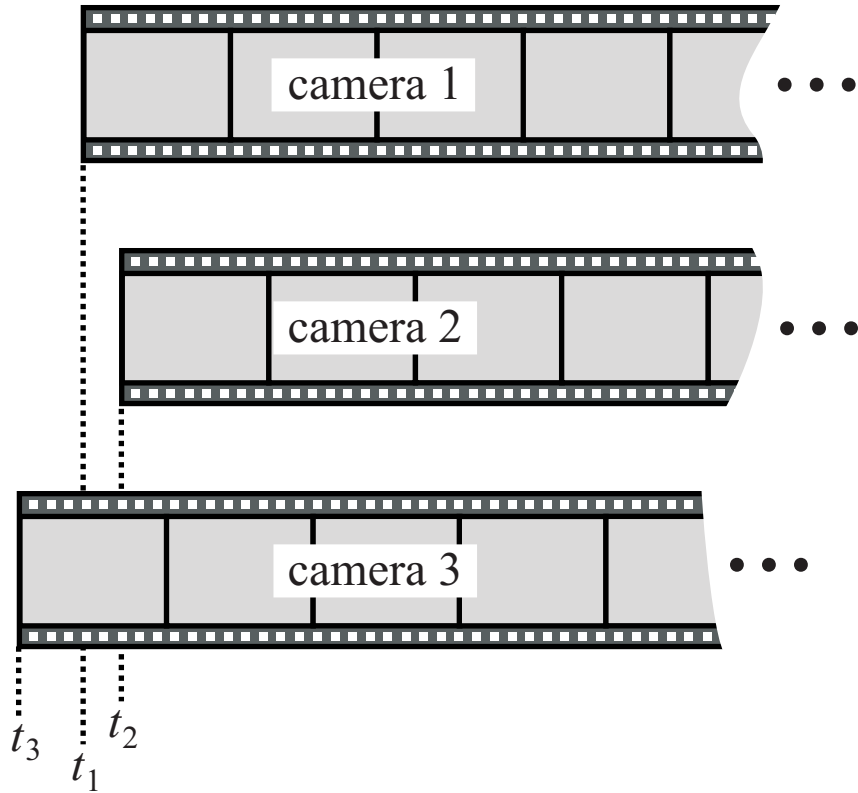


Figure 2.9: Diagram of the frame alignment between cameras. The time lags between cameras, $t_1 - t_2$, $t_2 - t_3$, and $t_3 - t_1$, can be up to one frame length and change with each recording cycle.

after the analysis of the first is finished so that files do not accumulate and fill the hard disk.

The complete automation procedure is as follows (Figure 2.10). Using the MiDAS software, we start all three cameras with the auto record feature. We set the pulse generator to send a trigger pulse every 62.5 seconds. When a pulse is generated, the three cameras finish recording with their active frame. MiDAS then transfers the video data from each camera control computer via the network to the corresponding analysis computer. When each video file has been completely transferred over the network, the analysis computer begins to process the data, and the camera computer begins to record again. When the next trigger pulse is received, another set of videos are saved over the network to the analysis computers while the processing of the first set is ongoing. The three analysis computers finish processing the first set, delete the AVI files, and send the resulting velocity data over the network to the O₂ machine. A few seconds later, the saving of the next set of complete video files is completed, and the processing starts again. The data acquisition and control network is shown in Figure 2.11.

2.4 Digital PIV Analysis

At the heart of a PIV measurement is the digital image analysis by which velocities are measured. For our 3-D LH μ PIV system, this analysis is the first of three steps required to measure \vec{v}_0 and \mathbf{M} . In the second step, the velocity data from each of three orthogonal planes is combined into one three-dimensional array of velocity

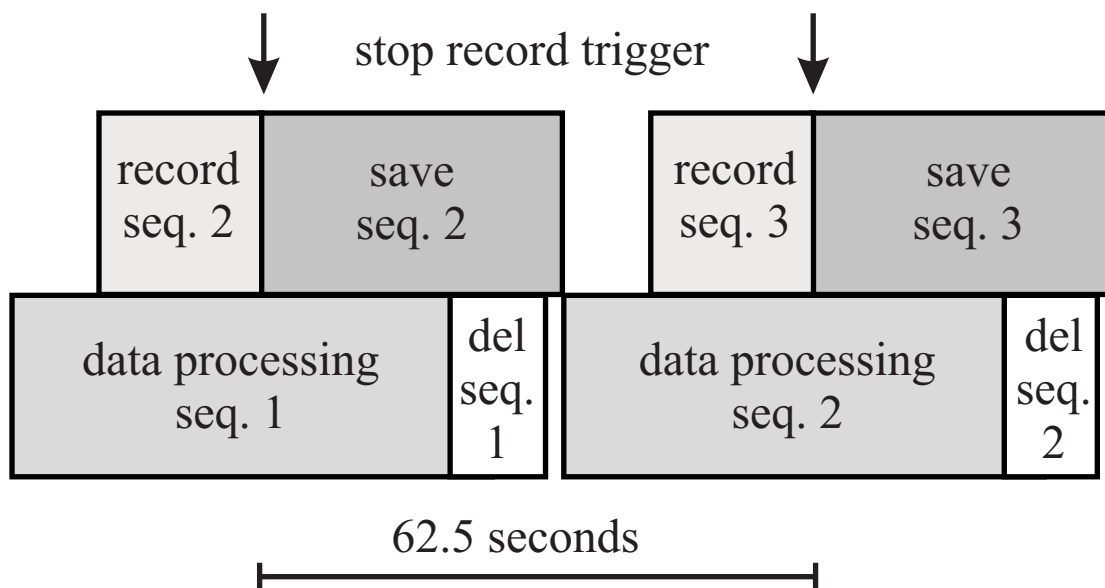


Figure 2.10: Schematic of the video recording and processing loop for one camera. While one video sequence is processed on the analysis computer, the subsequent video sequence is recorded and saved.

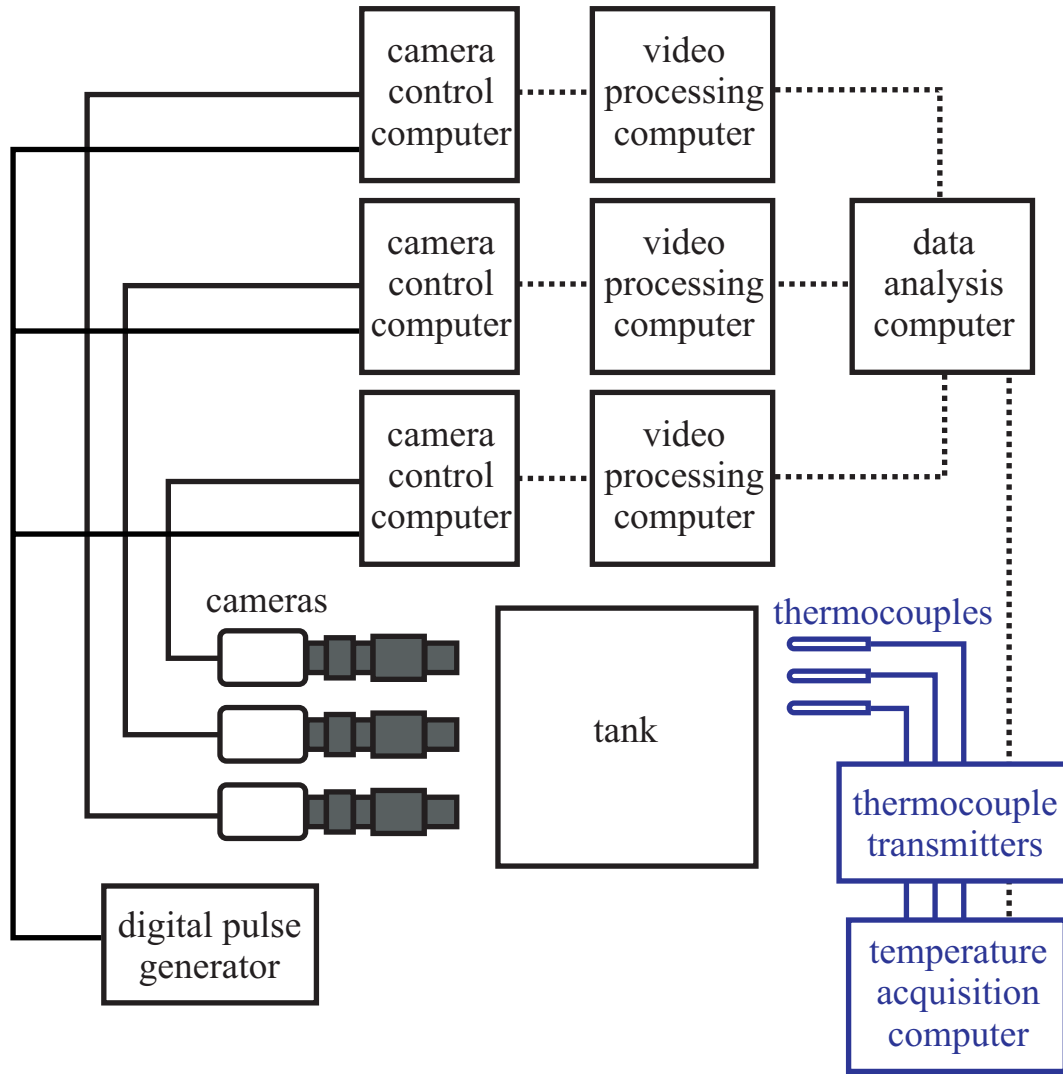


Figure 2.11: Diagram of the data acquisition and control network. Dotted lines represent ethernet connections. Components shown in blue are used only for the convection system.

vectors. The third step involves numerically fitting the velocity vectors to the linear model of Eq. 2.1 to find \vec{v}_0 and \mathbf{M} . In this section, these three steps will be described in detail (Figure 2.12).

2.5 PIV Analysis

The PIV analysis is performed identically for the three orthogonal views, so the procedure described here for one camera view applies equally to all three. As described in the preceding section, 100 MB video files are saved over the network to an SGI Octane computer which handles the heavy analysis. Videos are saved as uncompressed AVI (Audio Video Interleave) files, a standard PC format. These files begin with a header of 4096 bytes which contains information such as the number of frames, the frame rate, and the frame dimensions. Each frame is stored as an unbroken series of bytes, with each byte giving the greyscale level (0-255) of a single pixel, and the pixels stored from the lower left of the image to the upper right by rows. A detailed description of the AVI format is found in Appendix A.

The basis of the PIV analysis is the two-dimensional cross-correlation (*CC2D*) of particle images in two frames. The cross-correlation is defined as:

$$CC2D(a, b) = \langle I_1(x, y)I_2(x + a, y + b) \rangle_{x, y}, \quad (2.2)$$

where $I(x, y)$ is the intensity of the pixel at the location (x, y) . The peak of the function *CC2D* occurs for the x - and y -shift values a and b which best align the particle images in the two frames. Numerically, *CC2D* is calculated using two-

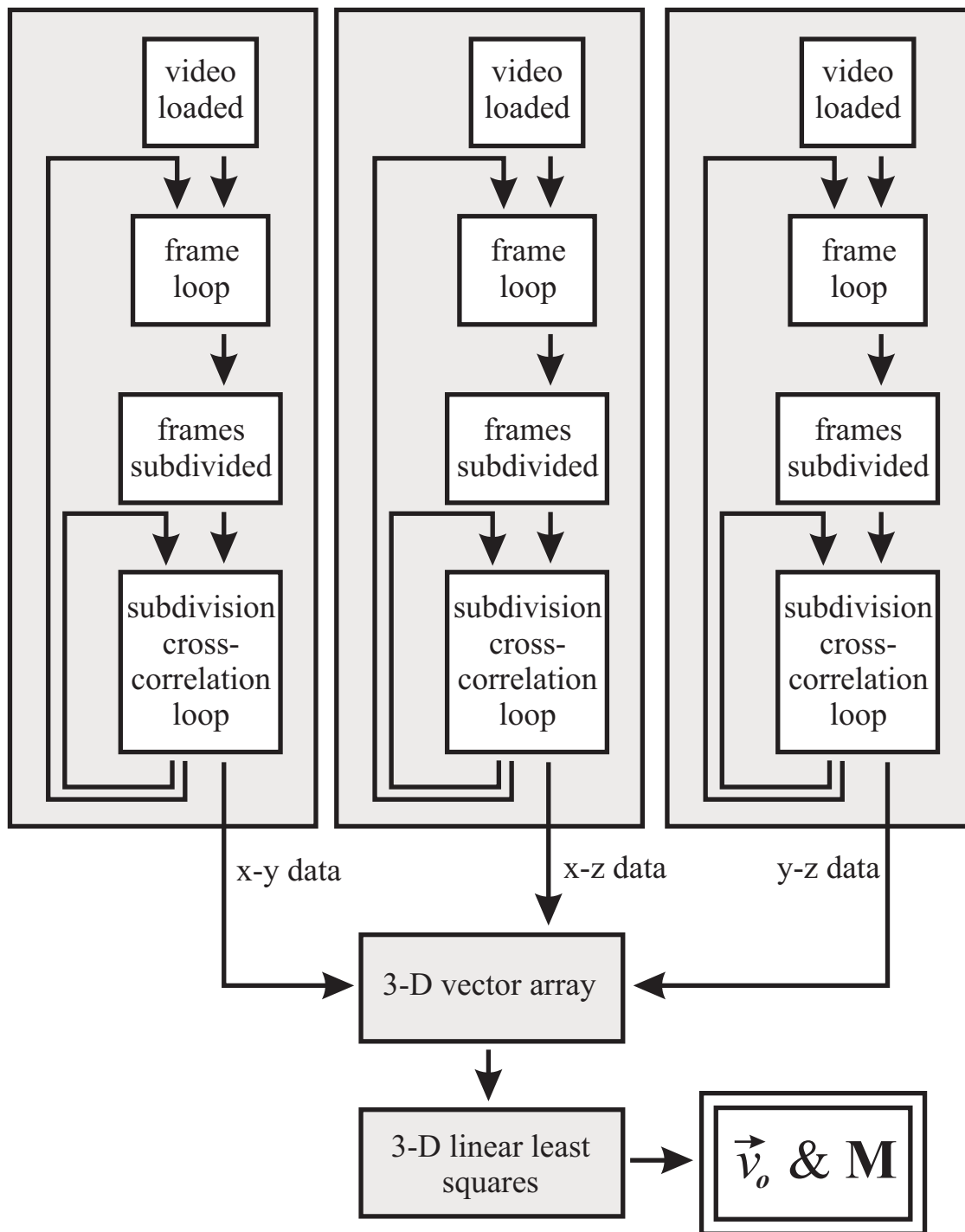


Figure 2.12: Flow chart of the digital analysis procedure.

dimensional fast Fourier transforms (FFT):

$$CC2D(x, y) = \mathcal{F}^{-1} [\mathcal{F}(I_1(x, y))\mathcal{F}^*(I_2(x, y))]. \quad (2.3)$$

Before performing cross-correlations, a decision must be made as to the number of subsections into which the frame must be divided, N^2 ($N \times N$ subsections). $N = 2$ yields a total of 12 subsections, or 24 equations of state of the form of Eq. 2.1, and so provides sufficient information to measure all components of v_0 and \mathbf{M} . With only 4 subsections per camera, measurement error in a single subsection can have a large effect on all calculated quantities. Moving up to $N = 3$ provides over twice the number of equations of state, which can improve data quality, but the size of the subsections also has an effect. For a given particle density, the number of particles per subsection scales as N^{-2} . Hence, the error in the subsection velocity measurements scales as N , so fewer subsections can improve the measurements. Larger subsections are beneficial for another reason. Between frames, a certain percentage of particles will shift out of each subsection, and others shift into the subsection. These “loners” have no matching image and introduce random error into the measurements. For a particular mean velocity, the percentage of particles which are loners scales as N . Clearly, a balance must be struck between improved statistics for gradient measurements and improved velocity measurements. In practice, the best value of N is determined empirically by comparing the “smoothness” of the resulting data from a sample video.

The value of N given in the command line and the frame dimensions ($xsize \times ysize$) are used to determine the subsection size. Table 2.2 shows the subsection

sizes for the most common frame dimensions. These subsection sizes were chosen to be close to $xsize/N \times ysize/N$ while also having small prime factors (to speed processing time). Many of these subsection dimensions result in slight overlapping between adjacent subsections, which does little to affect the data as the center location of the subimages are used for the final analysis.

Frame Size (pixels)	N	Subsection size (pixels)
480×420	2	256×256
480×420	3	192×144
480×420	4	128×128
320×280	2	192×192
320×280	3	128×96
240×210	2	128×108

Table 2.2: Frame rates, pixel resolution, and maximum record time for the Redlake PCI 2000S camera.

The first step in the program is to load an entire video file into the computer’s memory, which cuts down on the time spent reading from the hard disk. The AVI header is then parsed to determine the dimensions of a frame and the number of frames. The main body of the program consists of two main loops: one over all frames in the video, and the second over all subsections in a frame. The first two frames are loaded into two arrays. For the first subsection in each of the two frames,

the following four-step calculation is carried out:

$$\tilde{I}_1(k_x, k_y) = \mathcal{F}[I_1(x, y)] \quad (2.4)$$

$$\tilde{I}_2(k_x, k_y) = \mathcal{F}[I_2(x, y)] \quad (2.5)$$

$$\tilde{I}_{12}(kx, ky) = \tilde{I}_1^*(kx, ky)\tilde{I}_2(kx, ky) \quad (2.6)$$

$$CC2D(x, y) = \mathcal{F}^{-1}[\tilde{I}_{12}(kx, ky)]. \quad (2.7)$$

The pixel intensity data, I_1 and I_2 , consist of real numbers, so real-to-complex FFTs are performed in the steps in Eqs. 2.4 and 2.5. Using real-to-complex FFTs cuts the number of floating point calculations required and so saves processing time. Likewise, the step in Eq. 2.7 is performed with a complex-to-real FFT.

The function $CC2D$ is the cross-correlation of the two subsections. The peak of this function represents the fluid velocity between frames in that region of flow (Figure 2.13).

If one simply uses the brightest pixel in the cross-correlation to determine the velocity, the result is pixel-quantization of velocity values. This pixel noise can easily wash out the actual velocity data (Figure 2.14). However, the cross-correlation peak extends over many pixels, and this additional data can be used to get subpixel resolution in the velocity measurements. A weighted average is taken in a radius r around the location of the brightest pixel (x_p, y_p) . The intensity values are squared for the averaging to decrease the influence of background noise [56].

$$x_w = \frac{\sum_{x-x_p \leq r} x \cdot I^2(x, y)}{\sum_{x-x_p \leq r} I^2(x, y)} \quad \text{and} \quad y_w = \frac{\sum_{y-y_p \leq r} y \cdot I^2(x, y)}{\sum_{y-y_p \leq r} I^2(x, y)}. \quad (2.8)$$

The ideal radius r over which the average is taken is determined empirically for a given tracer particle size. The location of weighted average peak (x_w, y_w) is taken

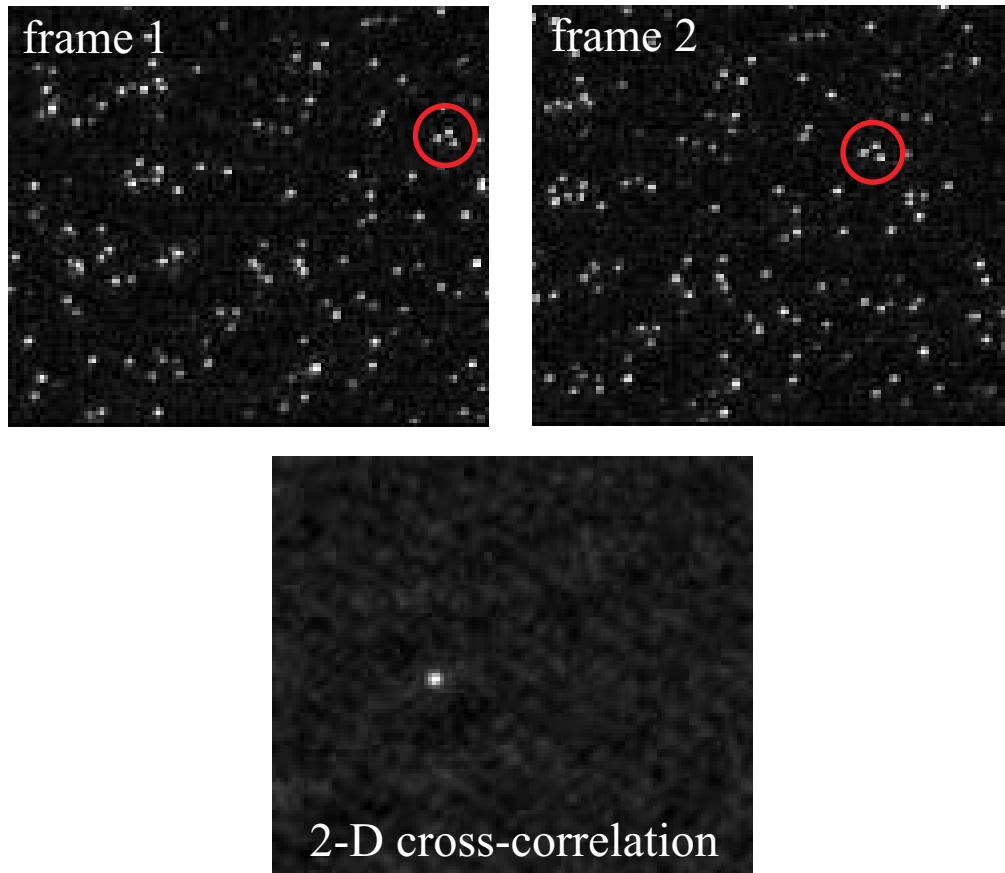


Figure 2.13: Corresponding subsections from two consecutive frames and their cross-correlation. A red circle is drawn around one group of particles which appears in both frames. The location of the bright peak relative to the center of the image in the cross-correlation gives the average particle velocity between frames.

to be the velocity at the center of the subsection. The time (defined as the time of the first of the two cross-correlated frames), velocity, and subsection location are written out to a data file. This entire procedure is repeated for each subsection and each frame pair for the entire video.

2.5.1 Spatial Rearrangement

Upon completion of the PIV analysis on a video, each analysis computer sends its data file over the network to the computer which handles the linear model. These three data files contain two-dimensional velocity vectors and their locations in a plane. Before fitting to the model, these data files must be combined appropriately into a single file containing vectors in 3-space.

Each camera treats its data as (x, y) coordinates. By definition, however, only camera 2 sees the x, y -plane. Camera 2 sees the z, x -plane, and camera 3 sees the z, y -plane. A short program reassigns the vector locations to the correct planes. Additionally, the vector locations are shifted such that the origin \vec{x}_0 where the laser sheets meet is the point $(x, y, z) = (0, 0, 0)$. This data file, containing two-dimensional vectors in 3-space, is passed to the program which fits the linear model.

2.5.2 Fitting the Linear Model

To fit the three-dimensional PIV data to the linear model of Eq. 2.1, a linear least squares calculation is performed. Our collaborator Dr. Eric Kostelich wrote the

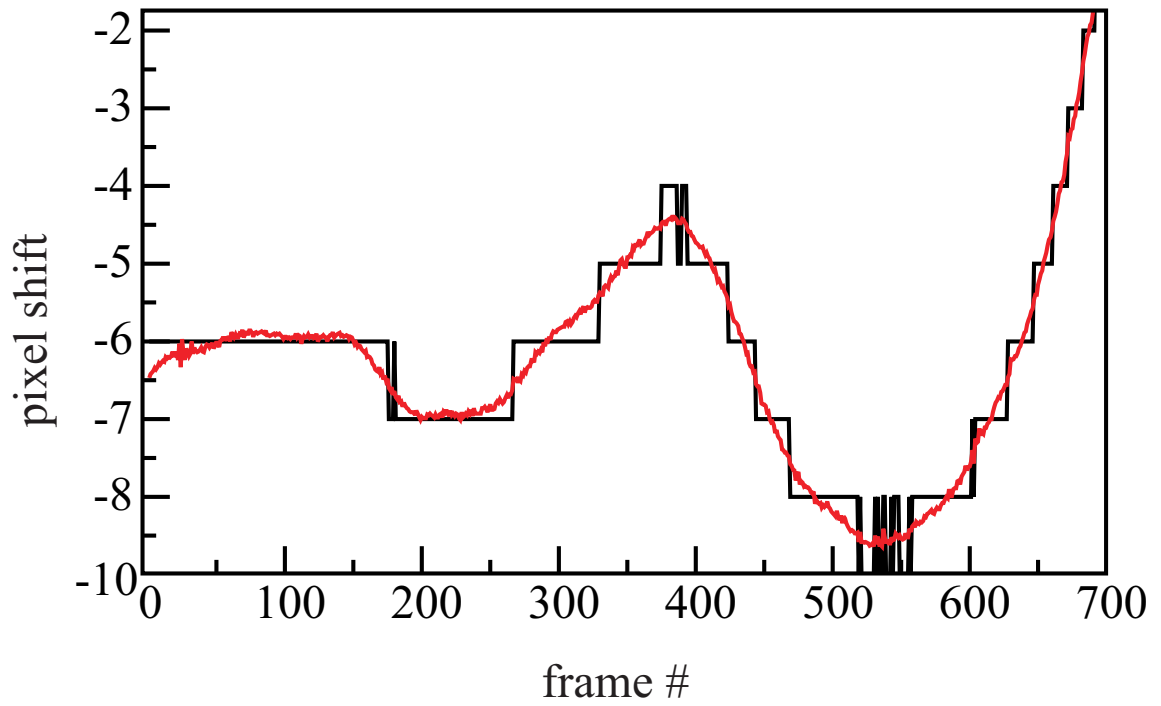


Figure 2.14: Subsection velocity traces before and after weighted averaging. Weighted averaging around the peak pixel (red curve) in the cross-correlation greatly reduces the pixel noise.

program frag.f90 to carry out this processing step. The Fortran 90 code of this program can be found in Appendix A.

The linear least squares fit is performed subject to the divergence-free condition (Eq. 1.2). The program can also fit to an unconstrained linear model or an unconstrained quadratic fit, which includes the third term of the Taylor series. Since the flow system is known a priori to be divergence-free, the unconstrained model was not used. The quadratic model has 30 unknown quantities and would require at least 3×3 subsections, whereas we often use a 2×2 division. All analysis to date was performed for the constrained linear model, and only that model will be discussed here. The three-dimensional combined vector data is cast as a series of linear equations of state of the form:

$$v_i = \beta_i \cdot (x, y, z, 1) = \left(\frac{\partial v_i}{\partial x}, \frac{\partial v_i}{\partial y}, \frac{\partial v_i}{\partial z}, v_{i0} \right) \cdot (x, y, z, 1),$$

where the vectors β_i contain the twelve desired quantities, and the quantities v_i are the experimental measurements. Each subsection gives two such equations of state, so $N \times N$ subsections gives $6N^2$ equations of state. These $6N^2$ linear equations plus the constraint condition are passed to the standard LAPACK routine “sgglse.” The linear algebra routine “sgglse” numerically fits the constrained linear system and outputs the components of \vec{v}_0 and \mathbf{M} . An error value R is also calculated by the program to check the quality of the linear fit:

$$R = \frac{\sum_i (v_{actual} - v_{model})^2}{\sum_i v_{max}^2}. \quad (2.9)$$

The value v_{max} is chosen to be the highest expected pixel shift between frames. This form makes R a good relative measure; it works equally well for high and low

velocities and so reflects the accuracy of the linear fit and not the flow state itself.

The output of the linear modeling program for a set of three videos is written to a file containing the thirteen pieces of information at each time step, \vec{v}_0 , \mathbf{M} , and R . By this arduous path, we reduce 300 MB of video to 2047×13 floating point numbers!

Chapter 3

The Turbulent Flow Systems

3.1 Background

LH μ PIV was developed to be a flexible measurement technique applicable to many turbulent flow systems. In the process of development, we discovered the strengths—and the limitations—of this method. We wanted a three-dimensional technique that could measure systems with low mean flow. LH μ PIV handles low mean flow situations very well, but proves less capable for flows with high mean velocity. That is, it works best for flows with a high turbulence intensity, $I_T \equiv v'_{rms}/U$, the ratio of the rms velocity fluctuations and mean velocity (Figure 3.1).

Additionally, the technique places geometrical requirements on the flow, as optical access to the flow must be available from three orthogonal directions for the

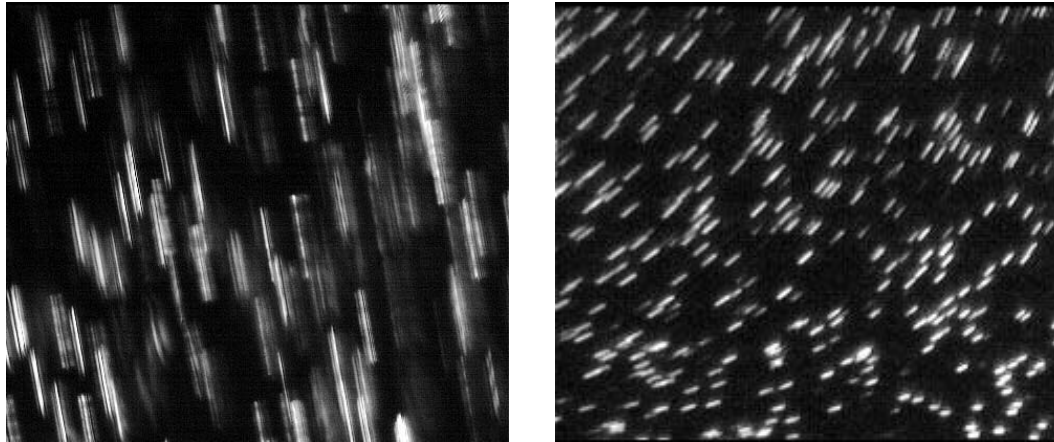


Figure 3.1: Images of particle streaks formed with low shutter speeds show the difference between flows with low and high turbulence intensity I_T . The low I_T image on the left is from a Taylor-Couette flow with $Re = 18,300$. The mean flow in this system is high, making it difficult to measure velocity gradients. The high I_T image is from oscillating grid turbulence with $Re = 2500$. Note the large variations in both the direction and magnitude of the velocity in the right high I_T image.

cameras and laser sheets. (Strictly speaking, the measurement can be carried out using cameras facing from three non-orthogonal directions, as long as no two cameras are coplanar. Such geometrical arrangements would complicate calculations and potentially decrease the measurement accuracy but greatly extend the applicability of the method.) We considered each of these issues in designing and building a flow system to study.

Initially, we planned to take turbulence measurements in a large Taylor-Couette apparatus. In such a system, the inner of two concentric cylinders rotates to drive motions in the fluid between the two. The Taylor-Couette system offered important benefits: the flows has been studied extensively in other manners, a simple laminar flow can be set up for use in instrument calibration, and, most importantly, a fully-fabricated apparatus was available. The apparatus, built by my advisor Dr. Daniel Lathrop for his dissertation work at the University of Texas, Austin, was generously loaned with all accoutrements by Dr. Harry Swinney. The cylindrical geometry presented imaging challenges, so we initially cut a flat window into the outside of the outer cylinder (Figure 3.2).

Even with the flat window and later corrective optics, imaging at such odd angles through a cylindrical fluid/wall interface proved too complex. Additionally, the Taylor-Couette flow has a very low I_T . Turbulent velocity fluctuations are superimposed on a much higher velocity rotating mean flow. We found it too difficult to measure velocity gradients against this background. Our experiences with this apparatus were quite valuable, however, in designing a different system to explore.

One thing made clear from our experiences with the Taylor-Couette apparatus

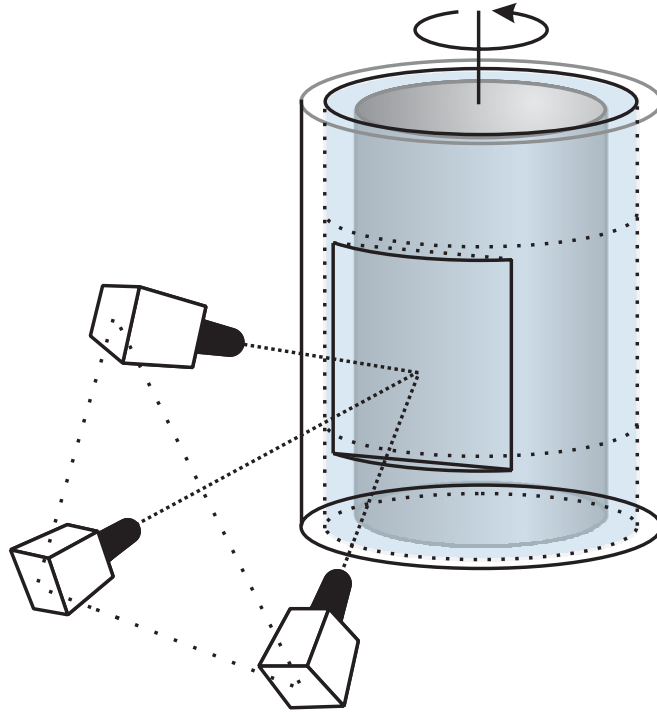


Figure 3.2: Proposed camera setup for LHMPIV measurements in a Taylor-Couette flow apparatus. The three cameras image through a flat face cut into the outer cylinder. The inner cylinder rotates to drive the flow.

is that a system with rectilinear geometry is preferable. Three perpendicular tank walls offer obvious viewing angles for cameras. Dr. Katepalli Sreenivasan made two useful suggestions for possible systems with low mean flow: oscillating grid turbulence and turbulent Rayleigh-Bénard convection. In a moment of inspiration, or perhaps just indecision, we decided to incorporate both of these flows into one apparatus. In the rest of this section, we detail the general tank design, the oscillating grid turbulence system, and the design of the convection system.

3.2 General Tank Design and Setup

The main chamber of the tank is a cube with sides $\ell = 24.1$ cm (Figure 3.3). The sides of the tank are 1.27 cm-thick clear acrylic (Polymethyl Methacrylate). A single 3/8" hose barb connection in the lower corner of one side wall is used for filling and draining the tank. Additionally, a 1/16" compression fitting is positioned near the center of the same side for thermometry. This hole is plugged when not studying convection. Two strips of thin mylar tape coated with a matte black, waterproof, high-temperature paint are affixed to the two inner walls opposite those through which the cameras face. The tape absorbs much of the light from the two vertical laser sheets after they traverse the flow and greatly reduces pixel noise on the cameras due to scattered light. Flanges at both ends of the flow chamber are used to attach secondary chambers for heating and cooling. The top chamber (cooling) is used only for convection and will be addressed in more detail in Sec. 3.4. A borosilicate glass plate 0.31 cm thick and 25.4 cm square, resting on top

of the bottom (heating) chamber, forms the base of the cube. Two O-rings at the periphery of this plate seal the two chambers. The acrylic bottom chamber is filled only for convective flows and is 22.9 cm square and 2.54 cm deep. It has a 1.27 cm thick floor and 3.18 cm walls. Each side of the bottom chamber has a 1/2" hose barb connector (Sec. 3.4). We fill the tank with filtered, distilled, deionized water, and add tracer particles once the tank is full.

3.2.1 Oscillating Grid Turbulence Setup

The majority of data that we have taken and analyzed is for turbulence produced by the oscillation of a mesh grid. The grid oscillated vertically (y -direction) with a forcing of the form $y(t) = y_0 \sin(\omega_g t)$, where y_0 is the vertical amplitude of the grid, and ω_g is its angular frequency. Initial data was taken at a point in the flow directly under a single oscillating grid. In this setup, however, significant vertical pumping of the flow was present $\langle v_y \rangle \neq 0$. Additionally, the oscillation of the grid could be seen strongly in the velocity traces, especially v_y .

We solved these problem by constructing a double grid. The double grid consists of two 21.2 cm square mesh grids rigidly attached at all four corners with stainless steel 10-32 bolts. The grids are welded stainless wire mesh with a wire diameter of 0.13 cm and square holes of size $\ell_g = 0.85$ cm. To mount the grids to the shaker, two additional supports are added off-center (Figure 3.4) to avoid blocking optical access or strongly influencing the flow at the center. A C-shaped mount attaches to these supports and a single vertical shaft. The horizontal bar

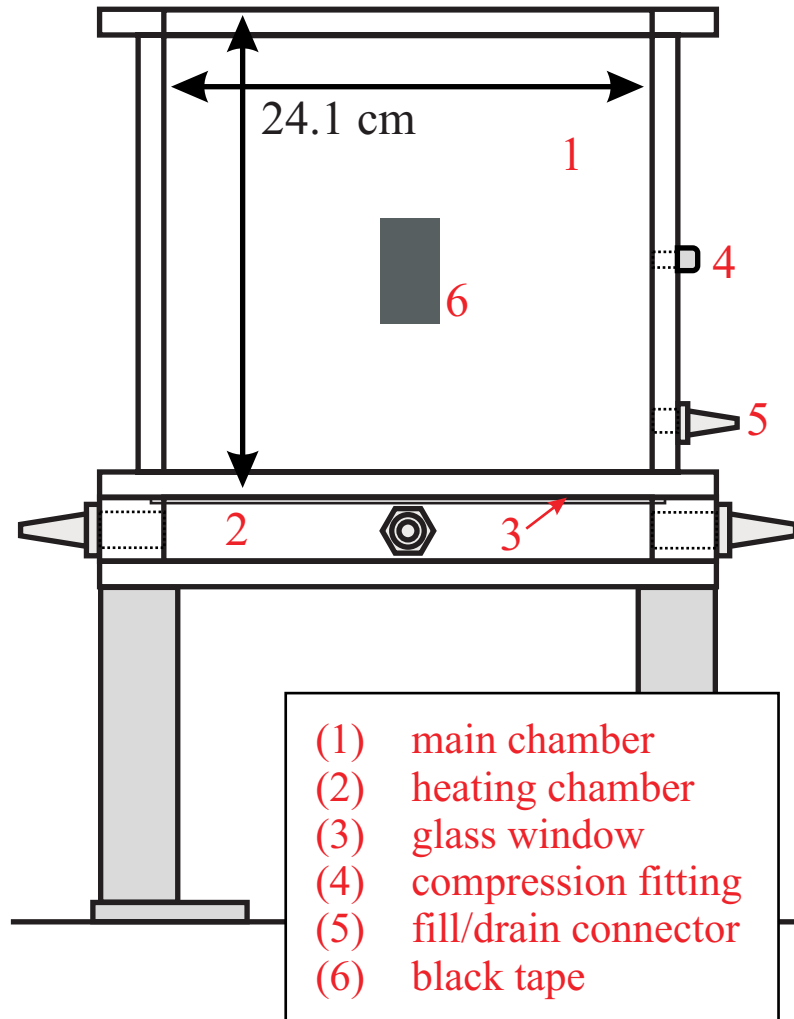


Figure 3.3: Cross-section of the tank with the bottom chamber attached. The top chamber and copper plate are added for convection, discussed, in Sec. 3.4.

of this mount is kept above the water line to prevent it from disturbing the flow. The spacing between the two grids is 6.5 cm, just large enough to accommodate the diagonal paths of the two vertical laser sheets. The grid is slightly smaller than the interior of the tank to allow it to be shifted horizontally so that the bottom camera sees the test volume through a grid hole. The test region is in the center of the tank horizontally, equidistant from the two grids.

The grid is forced using a linear actuator mounted vertically above the tank on a frame. A synthesized function generator provides a sine signal to a bipolar power supply used as an amplifier that powers the linear actuator. A peak-to-peak voltage and frequency are set with the function generator. The actual amplitude of the grid oscillation is measured using traces from a pen which is rigidly mounted to and oscillates with the shaft of the actuator. A collar attaches the actuator shaft to that of the grid. We choose the frequency and amplitude to achieve a desired Re or flow state. Figure 3.5 shows the system set up for grid turbulence.

3.3 The Convection Setup

The experimental setup to produce turbulent convection is considerably more complex. To produce turbulent convection, the fluid in the main chamber is heated from the bottom and cooled from the top (Figure 3.6). The floor and ceiling of the convection cell should be maintained at a constant temperature; heated and chilled water are pumped through the two end chambers for this purpose. While the floor and ceiling ideally would be thick and have a high thermal conductivity, the heating

chamber on the bottom must allow full optical access to the flow, so its design differs a bit from the cooling chamber. The two will be treated separately here.

The optical requirements on the bottom chamber presented us with design challenges. Short of Scotty beaming down and introducing to us the means of producing transparent aluminum, available transparent, thermally conductive materials are few. Pure sapphire crystals (Al_2O_3) are both clear and have high thermal conductivity (24 W/m-K). Given the large dimensions of the bottom window (the floor of the convective cell), a single crystal sapphire window could not be made. We did order a 10 cm square sapphire window to possibly embed in a larger copper window. We decided to use a borosilicate glass window which has a much lower thermal conductivity (1.1 W/m-K) than sapphire, but is easily available. To increase heat transfer, this window is only 0.31 cm thick.

A circulating temperature control bath pumps heated, distilled water through four 1/2" hose barb connectors, each centered on one side of the bottom chamber (Figure 3.7). The two inputs are positioned opposite the two outputs to prevent a stagnation point from forming in the center of the chamber. Additionally, the connectors are positioned as close as possible to the top of the chamber walls to increase the flow at the window.

Optical access to the flow is not needed through the top of the tank. Hence, a 3/4" thick copper plate (thermal conductivity: 388 W/m-K) serves as the top of the convection cell, clamped between the flanges of the main chamber and the cooling chamber. A copper tube with an inner diameter of 0.3 cm is soldered through one corner of the copper plate and is flush with the bottom of the plate. This tube pierces

through the top of the coolant chamber and is required for filling and draining the cell as well as adding particles to the flow. When preparing the experiment for convection, the convection cell is filled with distilled water and tracer particles all the way to the rim. The copper plate is then placed on the top and the cooling chamber bolted down. Distilled water is then dripped in through the copper tube to fill the cell up to the copper plate. Chilled water is pumped through the top chamber in the same manner as the bottom chamber. Because refrigeration requires much more energy than heating, a powerful Neslab HX-150 circulating chiller capable of removing 4.5 kW of heat is used for the cooling bath.

Added diagnostics are required for the turbulent convection system. In Rayleigh-Bénard convection, the convective state is characterized by the Rayleigh number,

$$Ra = \frac{g\alpha\ell^3\Delta T}{\kappa\nu} \quad (3.1)$$

where g is the gravitational acceleration, α is the volumetric coefficient of thermal expansion, ℓ is the size of the convection cell, and κ and ν are the thermal diffusivity and viscosity of the fluid. In order to measure ΔT , one must know the temperature of the interfaces at the ends of the cell. Thermometry cannot be embedded into the thin glass plate, so Ra is estimated by measuring $\Delta T/2$ across half the cell. An E-type thermocouple extends into the flow through the compression fitting on the tank side. The tip of this thermocouple is positioned in the center of the tank vertically and very close measurement volume. Two more thermocouples, vertically separated by 1.27 cm, extend into the copper plate from the side. These two thermocouples are used to estimate the temperature at the interface of the fluid and the copper plate.

Each thermocouple is connected to a thermocouple transmitter which produces a 4-20 mA current proportional to the temperature (Figure 3.8). A reference resistor converts this signal back to a voltage to be read into a computer. The thermocouples were calibrated using boiling and ice water baths.



Figure 3.4: Photograph of the double grid and mount.

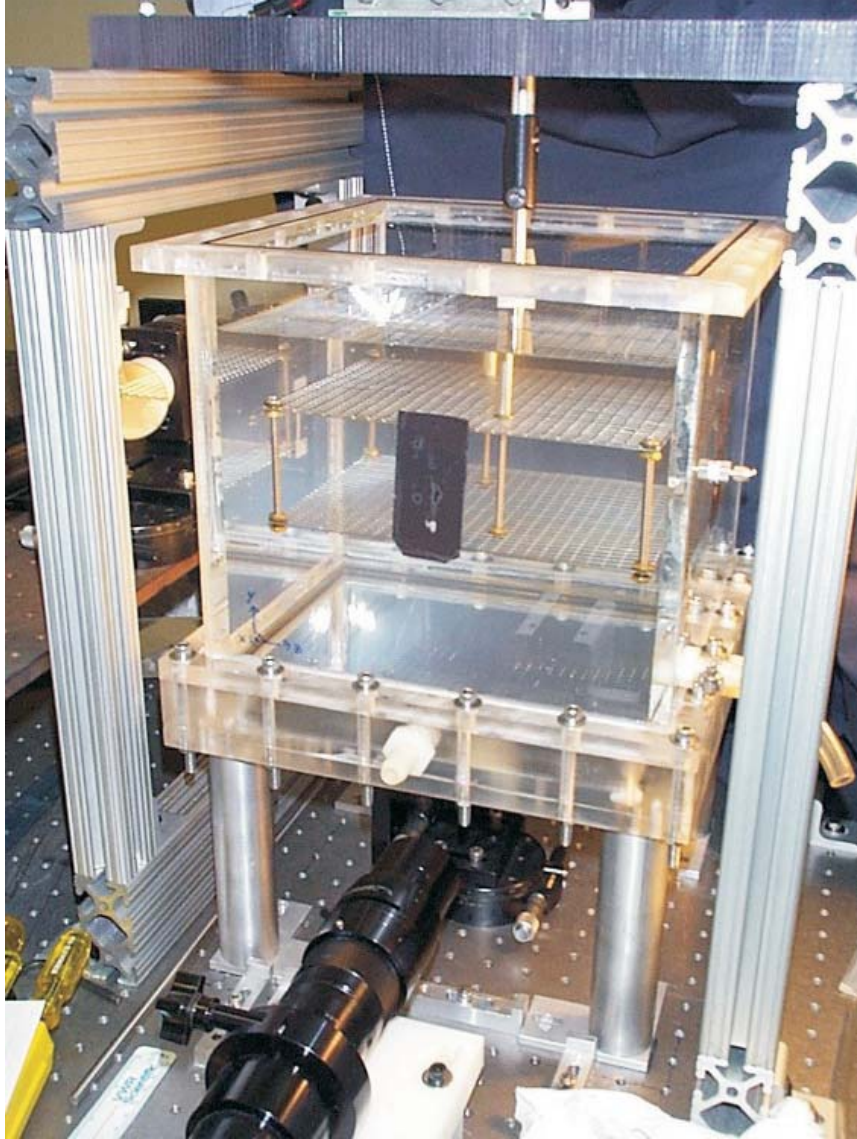


Figure 3.5: Photograph of the grid-turbulence system.

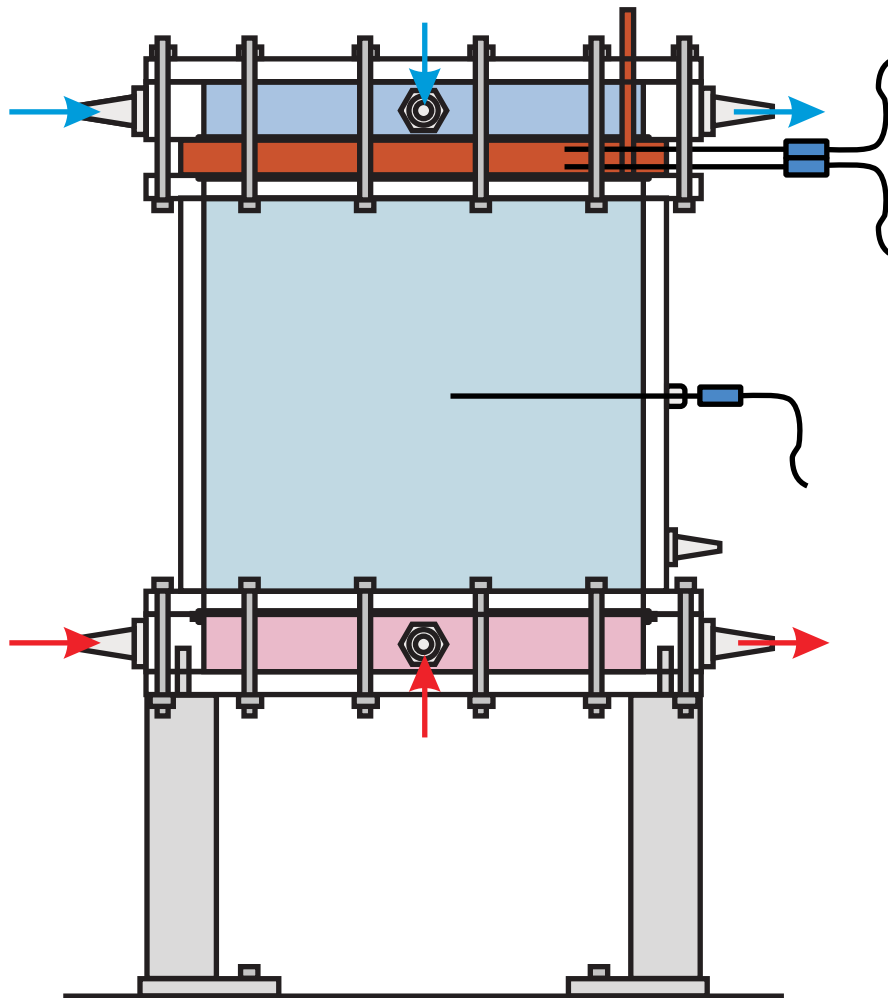


Figure 3.6: Diagram of the system set up for turbulent convection. The three thermocouples are shown coming in through right side. Heated water is pumped in through two sides of the bottom chamber and out through the other two. Likewise, cooled water is pumped through the top chamber. The copper tube at the top right is used to fill and top off the convection cell.

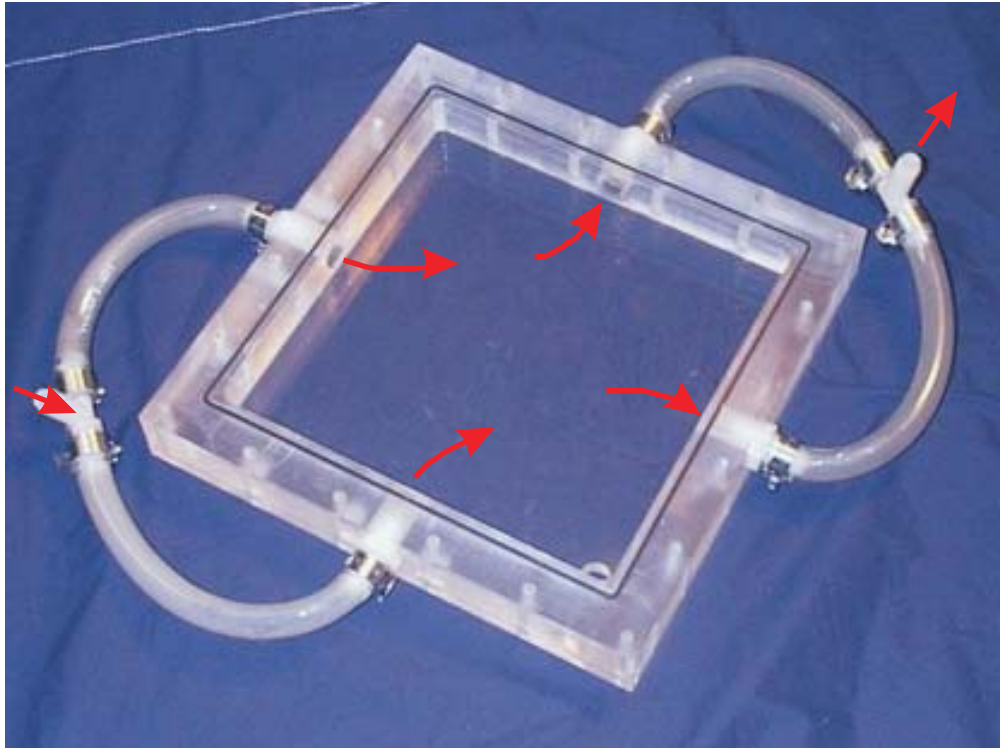


Figure 3.7: Photograph of one of the end chambers. The arrows show the direction of flow for the cooling or heating water.

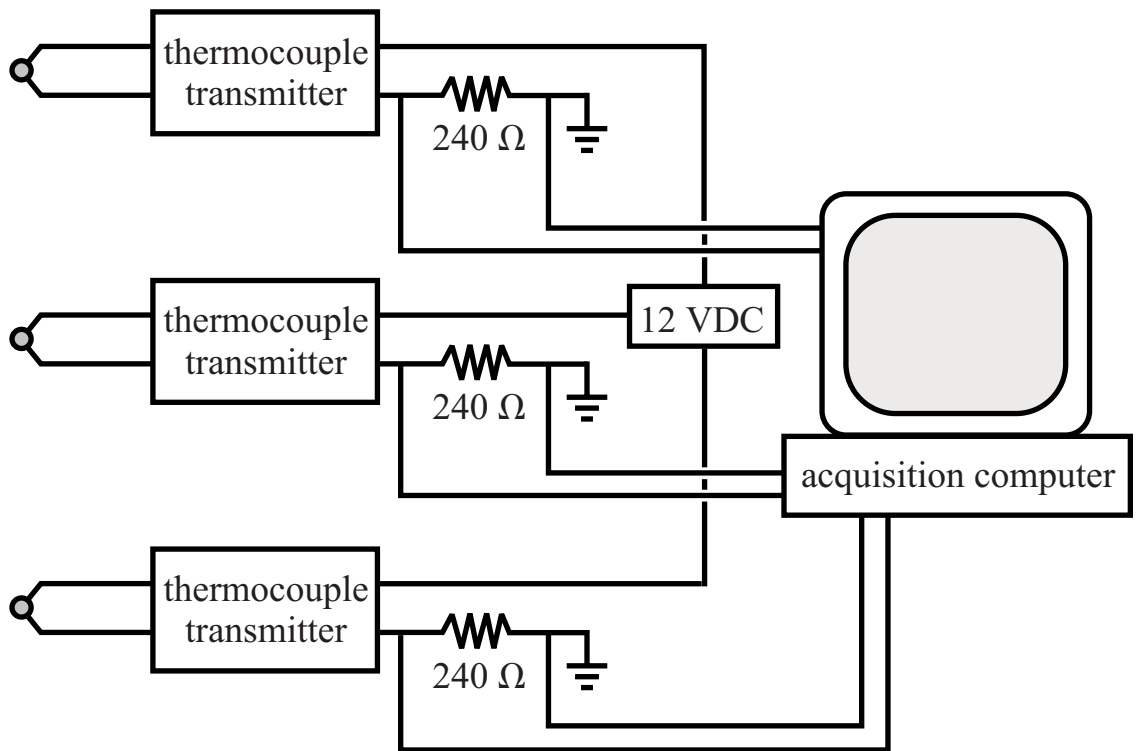


Figure 3.8: Wiring Diagram for the thermometry.

Chapter 4

Results and Analysis

4.1 Grid Turbulence

4.1.1 Data Collection and Analysis

We recorded and processed 2510 sets of videos of grid turbulence over a period of 50 hours. Of these sets (of three videos each), 44 were saved for later analysis and viewing. The videos were recorded at 125 frames/s with shutter speeds of 1/500 s. The full laser power, 5.2 W, was used to illuminate the tracer particles (see Fig. 2.2 for a sample frame). The angular frequency of the grid oscillation was $\omega_g = 62.8$ Hz with a forcing amplitude of $y_0 = 0.318$ cm (for a forcing of the form $y(t) = y_0 \sin(\omega_g t)$). These parameters can be used to define the grid Reynolds

number, Re_g :

$$Re_g = \frac{\ell_g y_0 \omega_g}{\nu}. \quad (4.1)$$

For this experimental run, $Re_g = 1700$.

For the PIV analysis, each frame was divided into 2×2 subsections. A weighted average (Eq. 2.8) around the brightest pixel in the cross-correlation was used to get sub-pixel resolution (estimated at < 0.25 pixels). The radius r over which the weighted averaging was performed was determined empirically. For a subsection in a test video, the PIV analysis was performed with the weighted average taken over a range of radii and for both squared and unsquared intensity values. A forward difference of the subsection velocity, $\delta v / \delta t = (v_{i+1} - v_i) / \delta t$, was calculated, with a pixel noise factor defined as $\langle (\delta v / \delta t)^4 \rangle$. A plot of the pixel noise versus r (Figure 4.1) shows the effect of the averaging. A radius of $r = 2$ pixels (corresponding to a weighted average over 5×5 pixels) with squared intensity data was chosen for the analysis. Typical subsection velocity traces, one from each camera, are shown in Figure 4.2. Velocity measurements from all 12 subsections are used in the linear model to find \vec{v}_0 and \mathbf{M} .

Figure 4.3 shows traces of all three components of \vec{v}_0 calculated using the linear least squares algorithm. Three components of the corresponding gradient matrix \mathbf{M} , $\partial v_x / \partial x$, $\partial v_x / \partial y$, and $\partial v_x / \partial z$ are shown in Figure 4.4. The velocity components all take on both positive and negative values with the oscillation visible in v_y . The gradient components are noticeably noisier than the velocity components. We measured 2510 (\vec{v}_0, \mathbf{M}) sets. The values \vec{v}_0 and \mathbf{M} can be used to “reconstruct”

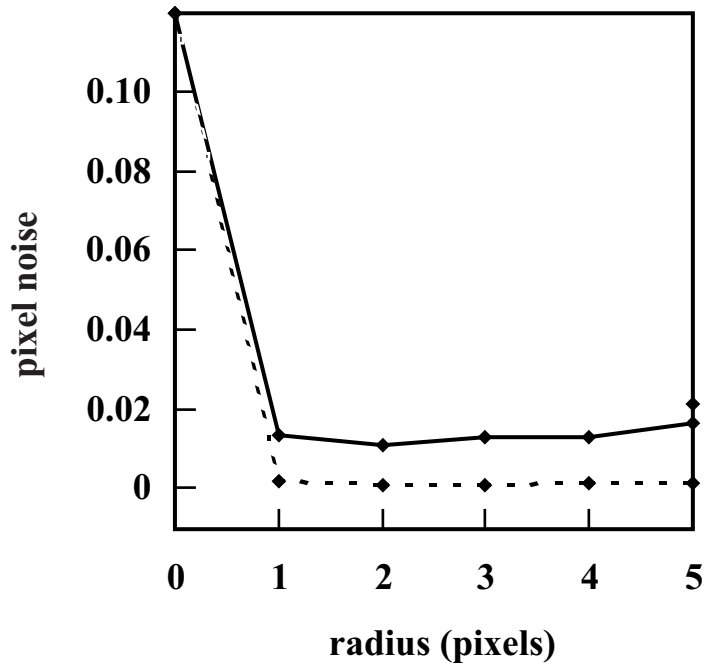


Figure 4.1: Plot of pixel noise vs. the weighted averaging radius r . Here, pixel noise $\equiv \langle (\delta v / \delta t)^4 \rangle$. The solid line is for a weighted average using the pixel intensity, and the dashed line is for a weighted average using squared intensity. For a radius of zero, the velocity data was pixel quantized, and the noise was relatively high. Increasing the radius and squaring the intensity data in the averaging dramatically decreases the noise. A radius of 2 was used for the data analysis.

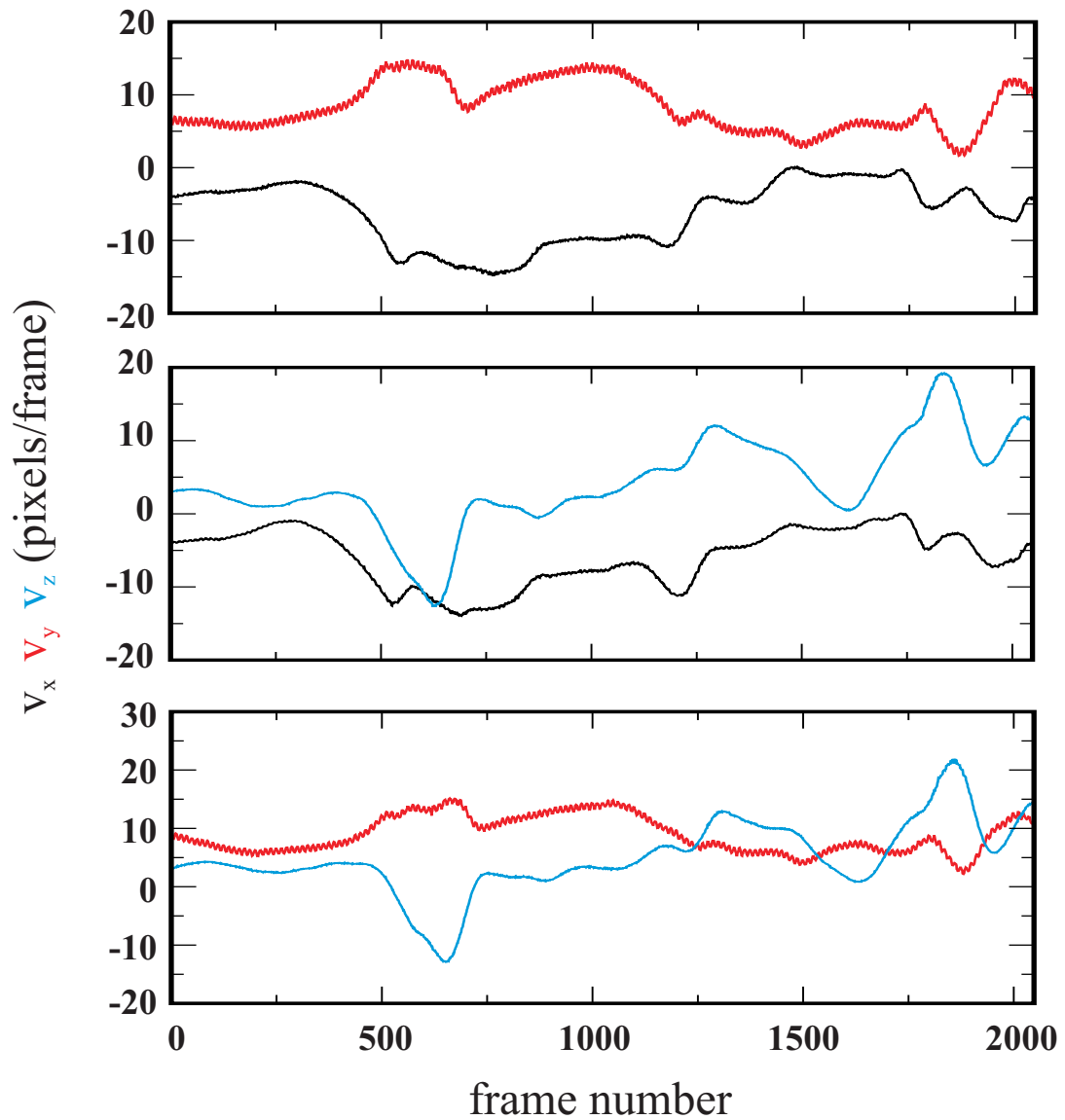


Figure 4.2: Subsection velocity traces from the three cameras. Each camera sees a two-dimensional slice of the flow and measures two components of the velocity in 4 subsections. The vertical oscillation of the grid is visible on the v_y traces from cameras 1 and 3. Gradients across the measurement volume appear as small differences in a particular velocity component between cameras.

the flow inside the test volume, as shown during a high- ϵ event in Figure 4.5.

An algorithm was used to remove spurious points from the data sets. As a result of too few particles or too many loners, incorrect subsection velocity values are sometimes measured. Without filtering the data sets to remove spurious points, the high-value statistics can be dominated by erroneous data. These velocities are uncorrelated with those in neighboring subsections. They usually produce large jumps in at least one gradient component when the least squares calculation attempts to fit them to a linear model. All 9 gradient components are used to calculate the dissipation (Eq. 1.5), so an error in any one component would likely appear in this quantity. Hence, traces of ϵ were used to find and remove such spurious points. When a spurious point is identified, all data at that time step were removed. The algorithm uses two conditions to identify bad points, both based upon unrealistic jumps in ϵ . Most bad points appear as sharp peaks, so those points which showed a jump in ϵ of greater than $0.04 \text{ cm}^2/\text{s}^3$ from both neighboring values (like a δ -function) were considered spurious. Additionally, those points which showed a jump in ϵ greater than $0.065 \text{ cm}^2/\text{s}^3$ on either side were removed. Even when ϵ is changing very rapidly, such a high jump in a single time step is highly unlikely. After cleaning the data, a set of 5,115,453 data points remained for analysis.

4.1.2 Grid Statistics

Table 4.1 shows time-average values of measured velocity components. It is clear from $\langle v_x \rangle$ and $\langle v_y \rangle$ that there was significant pumping of the fluid in those directions.

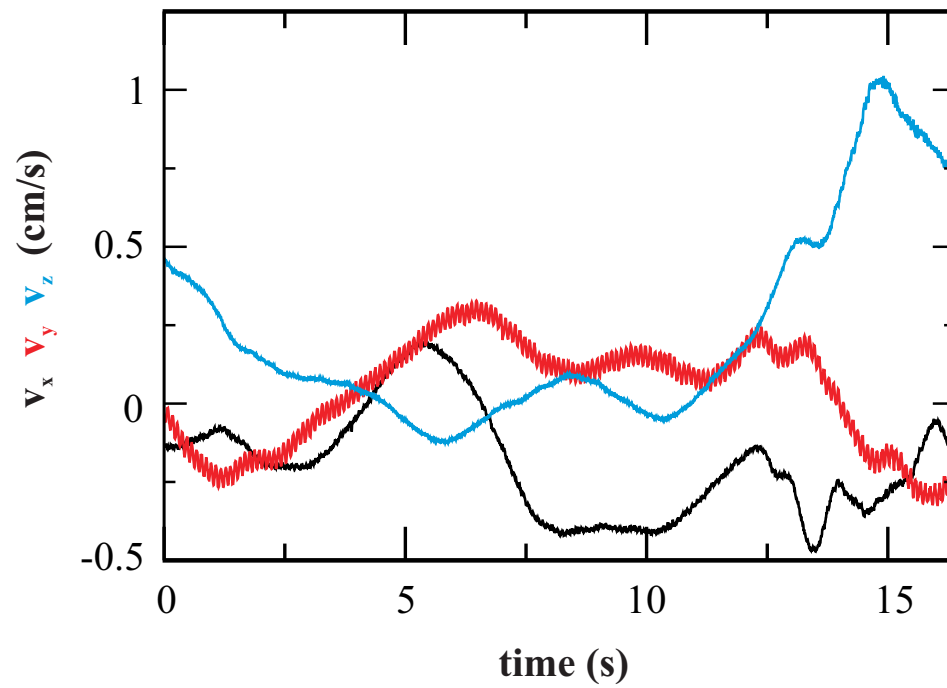


Figure 4.3: Typical traces of the three components of \vec{v}_0 . The velocities are measured at time steps of 0.008 s.

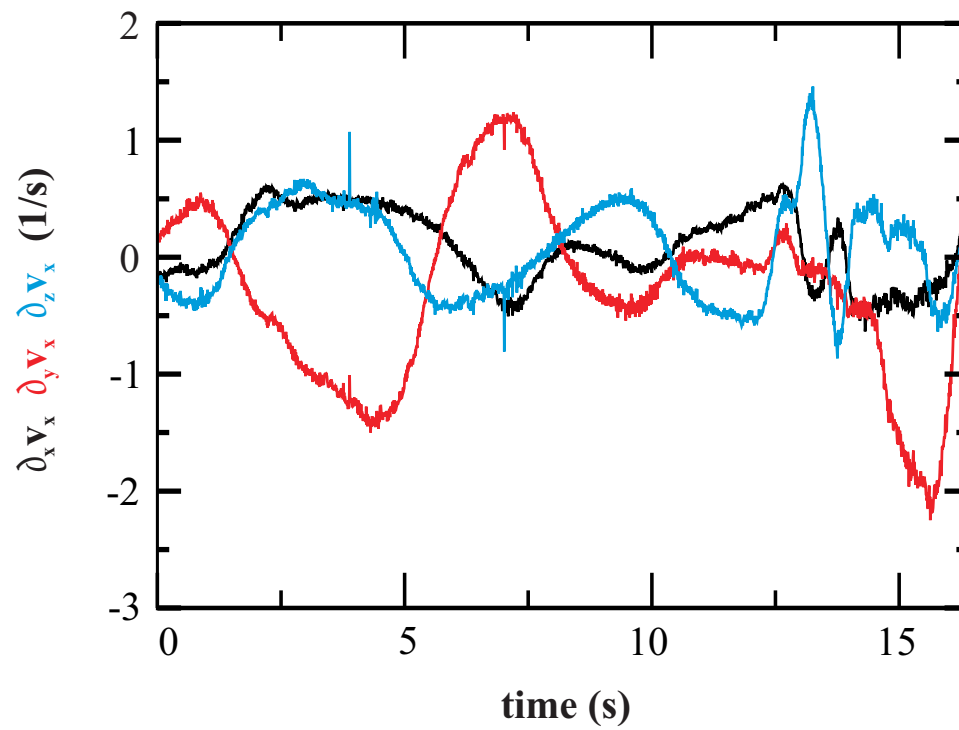


Figure 4.4: Typical traces of three components, $\partial v_x/\partial x$, $\partial v_x/\partial y$, and $\partial v_x/\partial z$, of the gradient matrix \mathbf{M} .

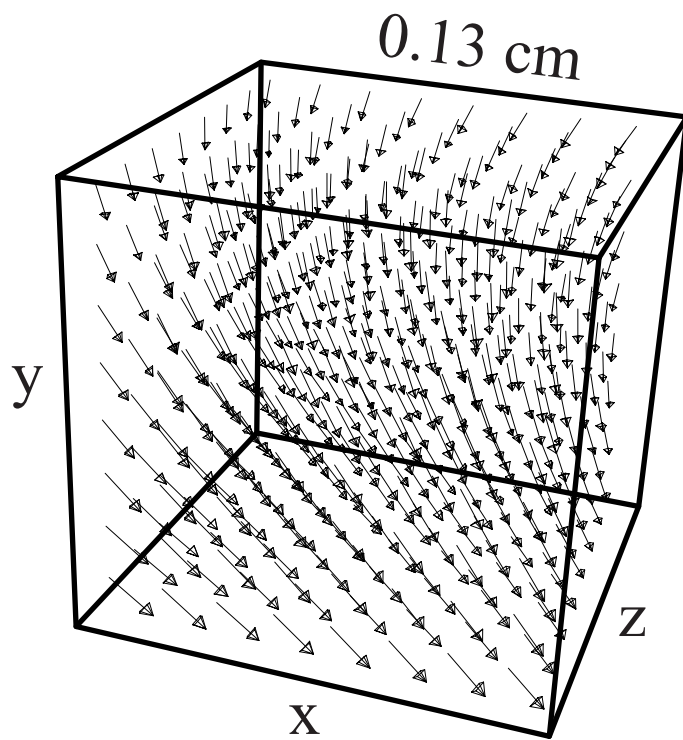


Figure 4.5: 3-D vector plot of the flow inside the test volume. This image shows the flow, reconstructed using \vec{v}_0 and \mathbf{M} , during a very high dissipation event.

X	$\langle X \rangle$	σ_X
v_x	-0.35 cm/s	0.25 cm/s
v_y	0.30 cm/s	0.25 cm/s
v_z	0.06 cm/s	0.38 cm/s
$\ \vec{v}\ $	0.66 cm/s	0.23 cm/s

Table 4.1: Time-average velocity components in oscillating grid turbulence. the grid oscillations are in the y -direction.

While single and double oscillating grid setups have been shown to produce nearly isotropic turbulence [60, 61], such larger circulations are usually present. One likely source of the pumping in our experiment is the design of the double grid. The mounting and support rods, as well as the free surface of the water, force the fluid and introduce asymmetries which amplify this effect. Figure 4.6 shows a probability distribution function (PDF) of v_y . The distribution is nearly Gaussian, as expected for turbulent flows, and clearly shows the directional pumping of the flow. Still, all three velocity components show both positive and negative values, and the flow is nearly isotropic with respect to the fluctuations.

The time-average of the error value R can be used to estimate the error in the velocity measurements. From $\langle R \rangle$ and Eq. 2.9, we find:

$$\langle v_{actual} - v_{model} \rangle \approx 2.79 \text{ pixels/frame} = 0.160 \text{ cm/s.}$$

24 measurements of the velocity are used to calculate \vec{v}_0 , so the error in that value is estimated to be $\approx 0.0326 \text{ cm/s}$, or $\pm 5\%$. If the error in the velocity measurements

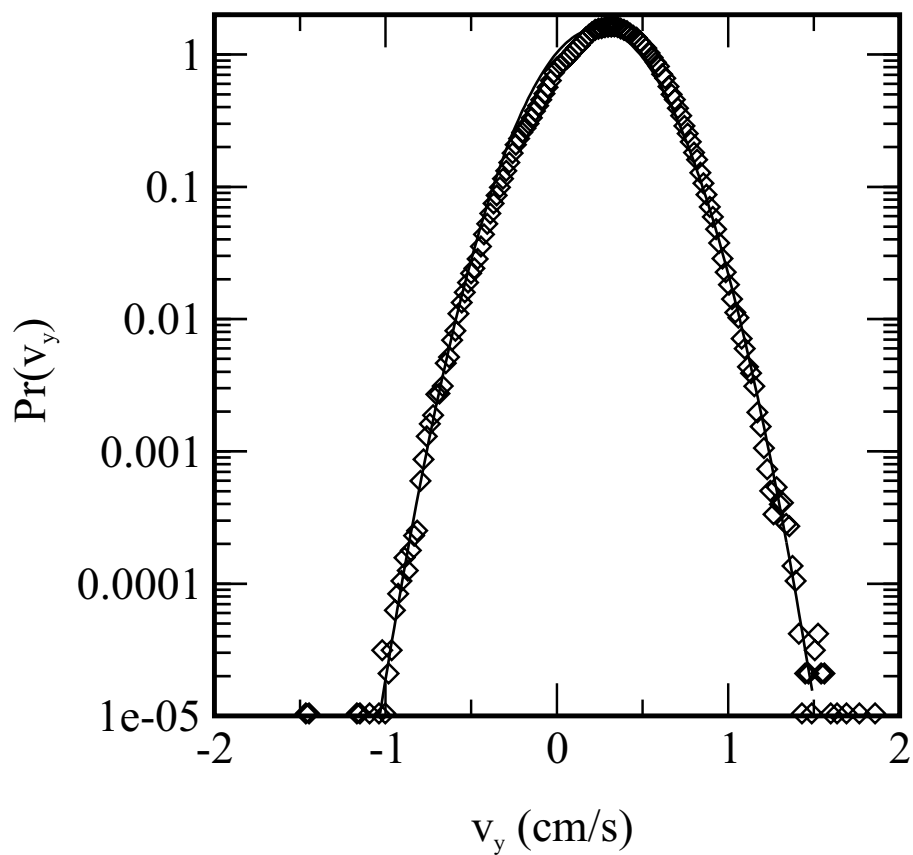


Figure 4.6: PDF of the v_y . The distribution is fit well by a gaussian, shown as a solid line. While, $\langle v_y \rangle > 0$, both negative and positive values are common. The PDF of v_x is similarly skewed to positive values, while $\langle v_z \rangle$ is very close to zero. Spurious high velocity points are seen at the lowest probability value.

were actually this high, it would wash out the fine structure seen in Fig. 4.3. More likely, variations in the R^2 value are due not to measurement error, but to inherent nonlinearities in the flow within the test volume. Observing the flow in a smaller region would improve the data in this respect.

The time average dissipation is $\langle \epsilon \rangle = 0.0337 \text{ cm}^2/\text{s}^3$ and can be used to find the Kolmogorov length scale for the flow:

$$\eta = \left(\frac{\nu^3}{\epsilon} \right)^{1/4}. \quad (4.2)$$

Using this relationship, we find $\eta=0.07 \text{ cm}$. Furthermore, this value can be used to calculate a different estimate of the Reynolds number:

$$Re = \left(\frac{\ell}{\eta} \right)^{4/3} = 2245, \quad (4.3)$$

where ℓ is the tank size. This definition of Re , as well as that in Eq. 4.1, involve some arbitrary choice of length scales. A common alternative measure is the Taylor microscale Reynolds number R_λ :

$$R_\lambda = \frac{(v_{rms})^2}{\nu(\partial_i v_i)_{rms}}. \quad (4.4)$$

R_λ is based upon measured statistical quantities in the flow and not external geometry. Using the x -component of the velocity, we find $R_\lambda = 54$.

As we are observing a turbulent flow, it makes sense to examine the velocities for evidence of the -5/3 power law scaling predicted by K41 (see Sec. 1.1.2). (Though in frequency space, we should see $E(f) \propto f^{-5/3}$.) Figure 4.7 shows the power spectrum of v_y , with the expected -5/3 scaling holding over less than a decade. The lack of Kolmogorov scaling is likely due to two factors: turbulence which is not fully

developed, and limitations of our system. The recording frame rate sets a limit as to the highest frequencies which can be resolved, and the recording time (16.4 s) sets a limit on lower frequencies. A larger region of $-5/3$ scaling would likely be seen for higher Re .

The distributions of velocity gradients are exponential (Figure 4.8). Exponential behavior of velocity gradients is a well-established feature of turbulence [63]. Figure 4.9 shows distributions of the x -component of the acceleration a_x and the helicity $h = \vec{v} \cdot \vec{\omega}$. Both of these quantities require a fully three-dimensional measurement. The acceleration is given by:

$$a_x = \partial v_x / \partial t + (\vec{v} \cdot \vec{\nabla}) v_x.$$

The second term on the right can be directly computed from the measured velocity and gradient components. The first term, $\partial v_x / \partial t$ is calculated from a least squares estimate from the measured velocity data. The a_x distribution is an stretched exponential, a form predicted analytically [64] and seen in numerical simulations [65] and the Lagrangian measurements of Bodenschatz et al. [53, 54]. The helicity is an important quantity in magnetohydrodynamics as a source of magnetic field amplification.

Before delving into a detailed discussion of ϵ and Ω in the next section, it is worthwhile to look at the statistics of these two quantities. Figure 4.10a show PDFs of these two quantities, both of which are highly intermittent, regularly reaching values over 30 times their time averages. The statistics of ϵ and Ω very closely resemble those observed in numerical simulations [59] and reflect the fact that the

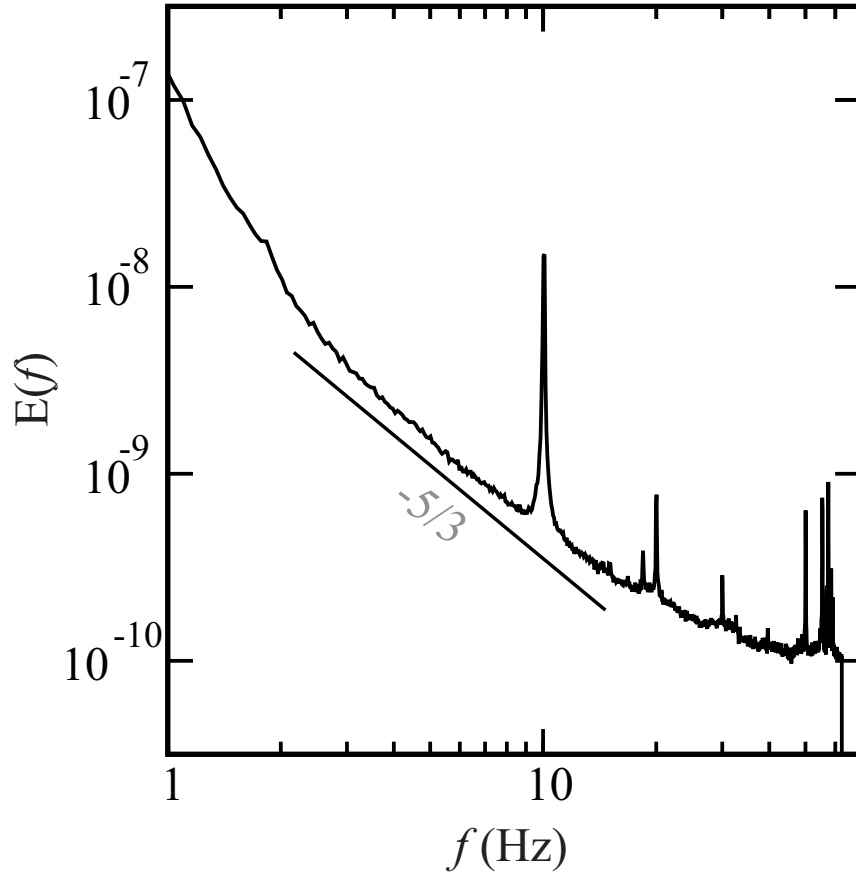


Figure 4.7: Power spectrum of v_y showing a small region of $E(f) \propto f^{-5/3}$ scaling. Large peaks are seen at the oscillation frequency of the grid, $f = 10$ Hz, and at higher harmonics.

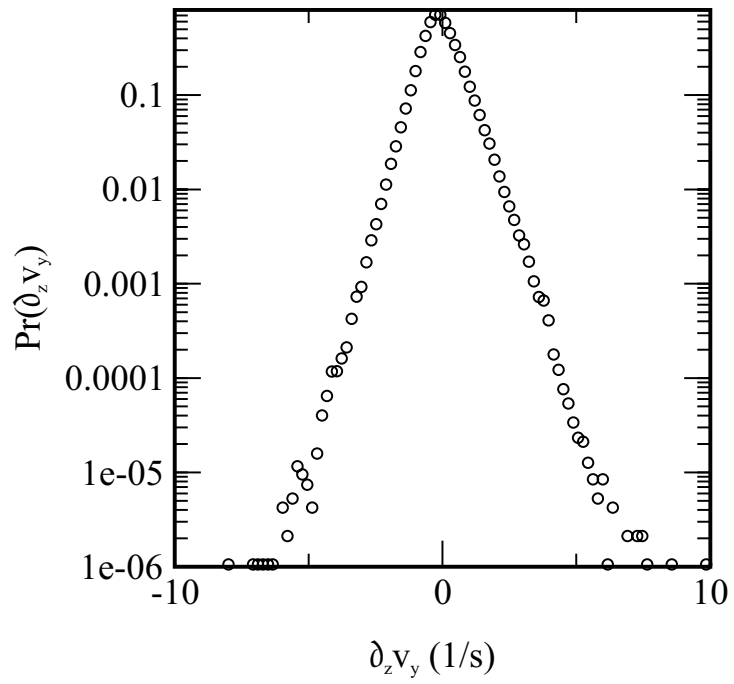


Figure 4.8: PDF of $\partial v_y / \partial z$, one component of the gradient matrix \mathbf{M} . The distribution is exponential with slight asymmetry around the mean.

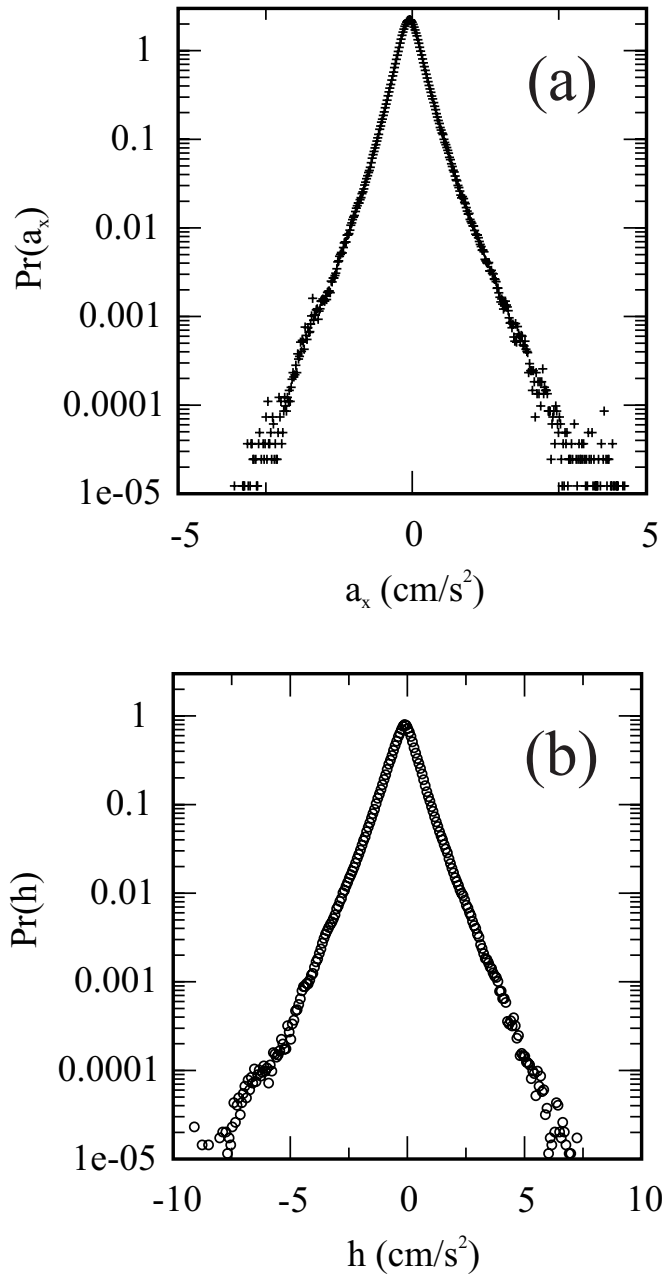


Figure 4.9: PDFs of a_x and the helicity h . a) The distribution of a_x is a stretched exponential, $\text{Pr}(a_x) \propto \exp(a_x^{0.68})$ as expected from previous analytical, numerical, and experimental work. b) The distribution of h is also a stretched exponential, $\text{Pr}(h) \propto \exp(h^{0.85})$, though its form is closer to a simple exponential.

enstrophy is a more strongly intermittent quantity. Log-log PDFs of ϵ and Ω (Figure 4.10b) show that near zero, $Pr(\epsilon) \propto \epsilon^a$ and $Pr(\Omega) \propto \Omega^b$, where $a \approx 2.34$ and $b \approx 1.44$. PDFs of eigenvalues of the symmetric strain matrix (Eq. 1.11) lend insight into the nature of high- ϵ events (Figure 4.11). λ_2 can take on either positive (stretching) or negative (compressing) values, but more commonly takes on a positive value. These results match those found by Tao et al. [57] in studies of channel flow using holographic PIV. For exceptionally high ϵ events, there are more likely to be two stretching directions and one compressing direction than vice versa.

4.1.3 Dissipation and Enstrophy

We have already seen in Figure 4.10 that the dissipation and enstrophy intermittently burst to values many times their time averages. One benefit of a time-resolved measurement like LH μ PIV is that individual intense events can be studied in depth. Figure 4.12 shows time traces of ϵ and Ω (normalized by $\langle \epsilon \rangle$ and $\langle \Omega \rangle$) for two video sequences with high- ϵ events. The two events shown are qualitatively similar. Both show a sudden sharp rise in ϵ accompanied by a downturn in Ω , then a peak in ϵ as Ω rises sharply, and finally a sharp decrease in both quantities. The growth of ϵ in the second sequence shows a more extreme functional form than in the first. In Figure 4.12a, ϵ shows exponential growth (Figure 4.13a), similar to that found by Kida and Ohkitani [38]. The growth of ϵ in Figure 4.12b is more closely described by algebraic growth with a -2 power law: $\epsilon \propto (t_0 - t)^{-2}$ (Eq. 1.8). This scaling has been predicted for a self-similar Euler singularity occurring at time t_0 . Though the

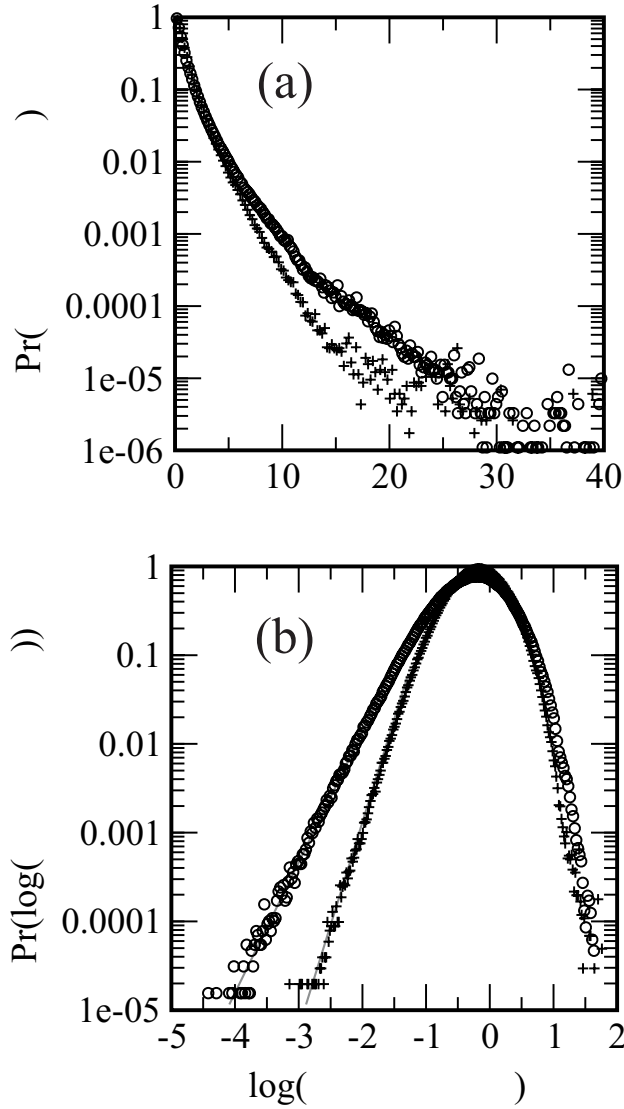


Figure 4.10: a) PDFs of $\epsilon/\langle\epsilon\rangle$ (+) and $\Omega/\langle\Omega\rangle$ (o). The tails of the PDFs extend toward high values of ϵ and Ω and are fit well by stretched exponentials: $Pr(\epsilon) \propto \exp(-\epsilon^{0.6})$ and $Pr(\Omega) \propto \exp(-\Omega^{0.45})$. Their time averages are: $\langle\epsilon\rangle = 0.0337 \text{ cm}^2/\text{s}^3$ and $\langle\Omega\rangle = 4.13 \text{ 1/s}$. b) Log-log PDFs of ϵ and Ω show a significant skewing towards values below their time averages. At low values, ϵ and Ω show scalings $Pr(\epsilon) \propto \epsilon^{2.34}$ and $Pr(\Omega) \propto \Omega^{1.44}$ over four decades.

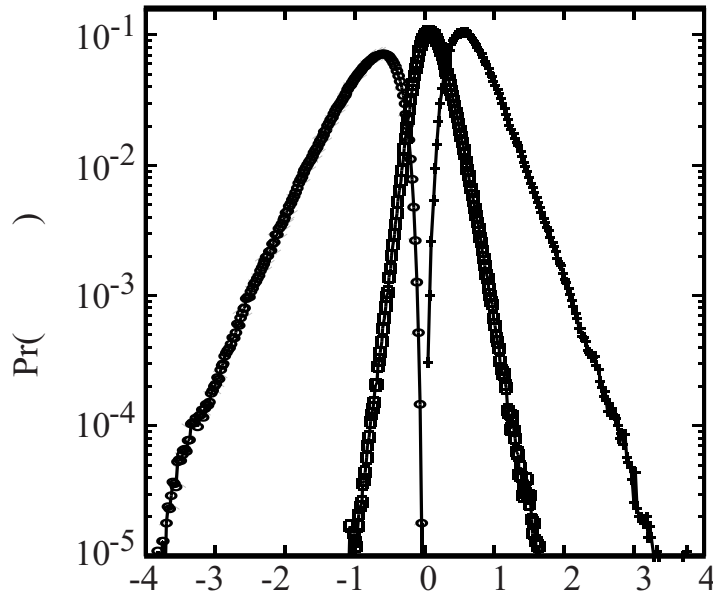


Figure 4.11: PDFs of λ_1 , λ_2 , and λ_3 , the eigenvalues of the symmetric strain matrix. Because the fluid is incompressible, $\lambda_1 < 0$ (representing compression), $\lambda_3 > 0$ (representing stretching), and $\sum \lambda_i = 0$. λ_2 can be either positive or negative, though the PDF is skewed toward positive values.

power law scaling occurs over less than a decade of $t_0 - t$, it is quite interesting to see such extreme growth at all.

Past numerical and experimental work has shown that in turbulent flows, regions of high dissipation and high enstrophy are spatially correlated. Figure 4.14 characterizes the interrelationship of these two quantities in our flow. High dissipation and enstrophy are much more likely to occur at the same time than separately. Similarly, correlations exist between the time derivative $\dot{\epsilon}$ and the local conditions of ϵ and Ω . More specifically, when the positive eigenvalue λ_3 of the strain matrix is large, the dissipation is on average rising (Figure 4.15). On the other hand, when Ω is large, ϵ is on average falling (Figure 4.16).

More than one mechanism may be responsible for these trends. Large coherent structures such as vortex tubes or filaments, long thin regions of intense vorticity, have been observed in grid-generated turbulence [66] and offer one explanation for the observed statistics. It has been observed that such filaments often have sheets of high dissipation wrapped around them. The statistics are consistent with structures being advected through the measurement volume such that the dissipation sheet typically preceded the vortex tube (Figure 4.17). It is possible that the dissipation would be concentrated in front of vortex tube as a result of the motion in that direction. In such a situation, a sudden rise would be seen in ϵ followed by a decrease in ϵ as Ω quickly increased. Both quantities would fall as the structures moved out of the measurement volume.

An alternate explanation relies on a series of events based on kinematics. Substituting the Taylor expansion of the velocity field (Eq. 2.1) into the Navier-

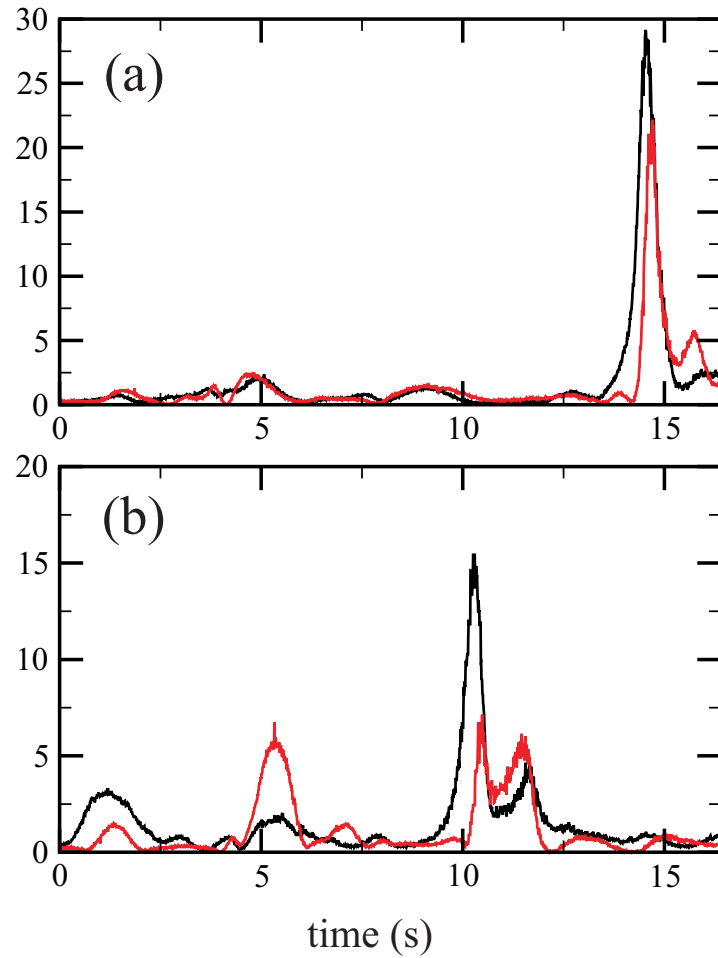


Figure 4.12: Time traces showing high dissipation (black) and enstrophy (red) events. The extreme events in both a) and b) are qualitatively similar, but the sharp rise in ϵ has a steeper functional form in the latter. A 3-D reproduction of the flow at the time of the ϵ peak in b) is shown in Fig. 4.5, in which both shear and rotation are visible.

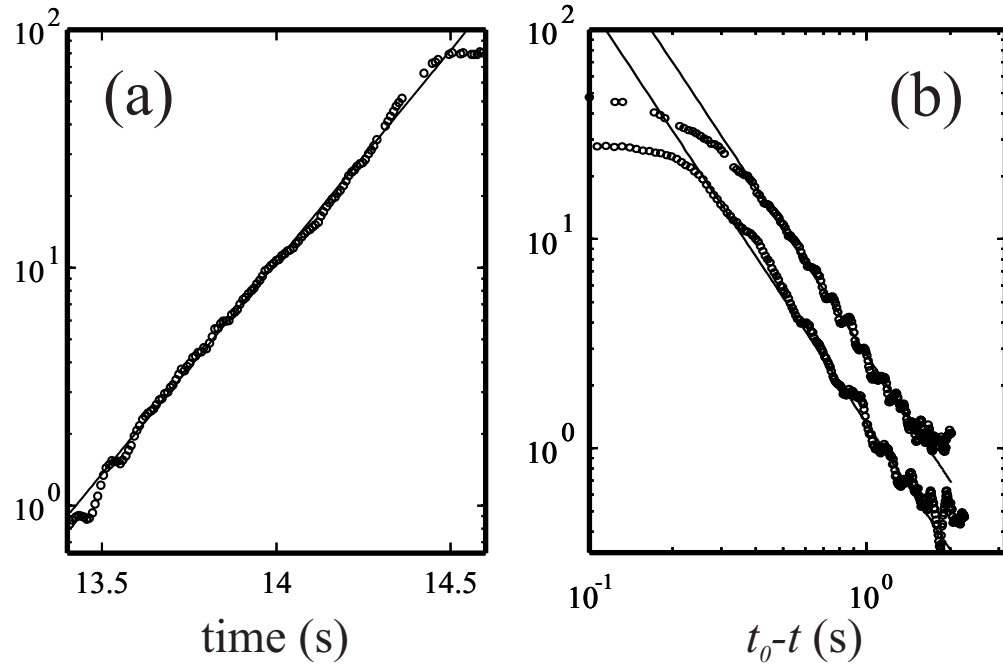


Figure 4.13: Examples of both exponential and algebraic growth of ϵ . a) Exponential growth of ϵ during the intense event in Figure 4.12a. The straight line represents the exponential growth $\epsilon \propto e^{\alpha t}$ with $\alpha = 1.75$ 1/s. b) Log-log plot of exponential growth of ϵ for the event shown in Figure 4.12b and one other. The dissipation is plotted versus $t_0 - t$, where t_0 is a time towards which ϵ is attempting to diverge. The straight line represents the scaling $\epsilon \propto (t_0 - t)^{-2}$ expected in the presence of an Euler singularity.

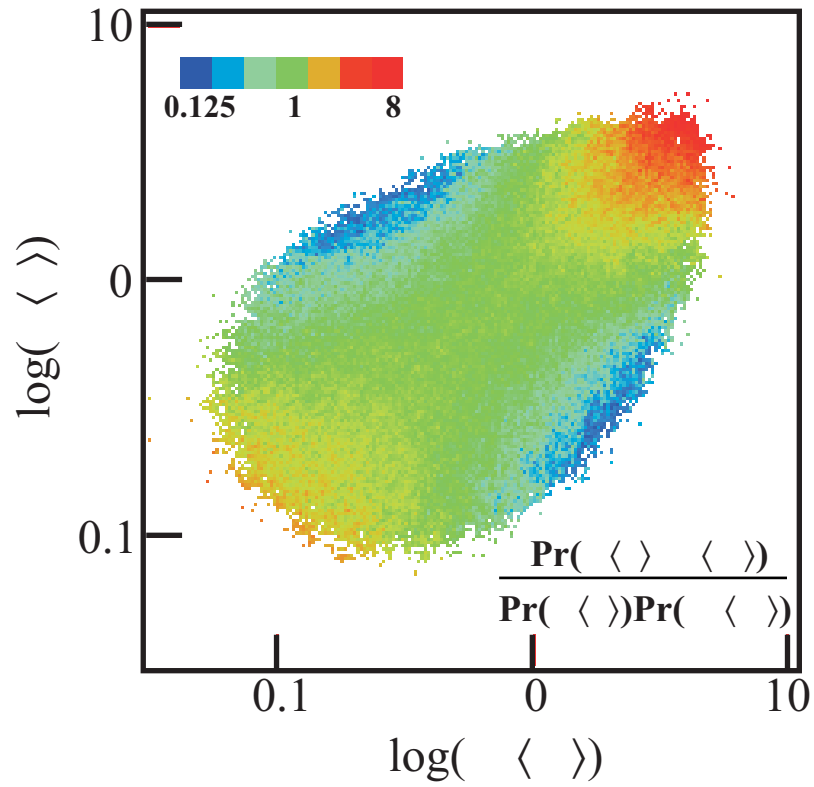


Figure 4.14: A scatter plot of $\log(\epsilon/\langle\epsilon\rangle)$ and $\log(\Omega/\langle\Omega\rangle)$. The color of the graphs represents the value $Pr(\epsilon/\langle\epsilon\rangle, \Omega/\langle\Omega\rangle)/Pr(\epsilon/\langle\epsilon\rangle)Pr(\Omega/\langle\Omega\rangle)$ and would be 1 (green) everywhere if these two quantities were statistically independent. We find that very high values of the dissipation and enstrophy occur simultaneously about eight times more often than would be expected. Particularly low values are similarly correlated.

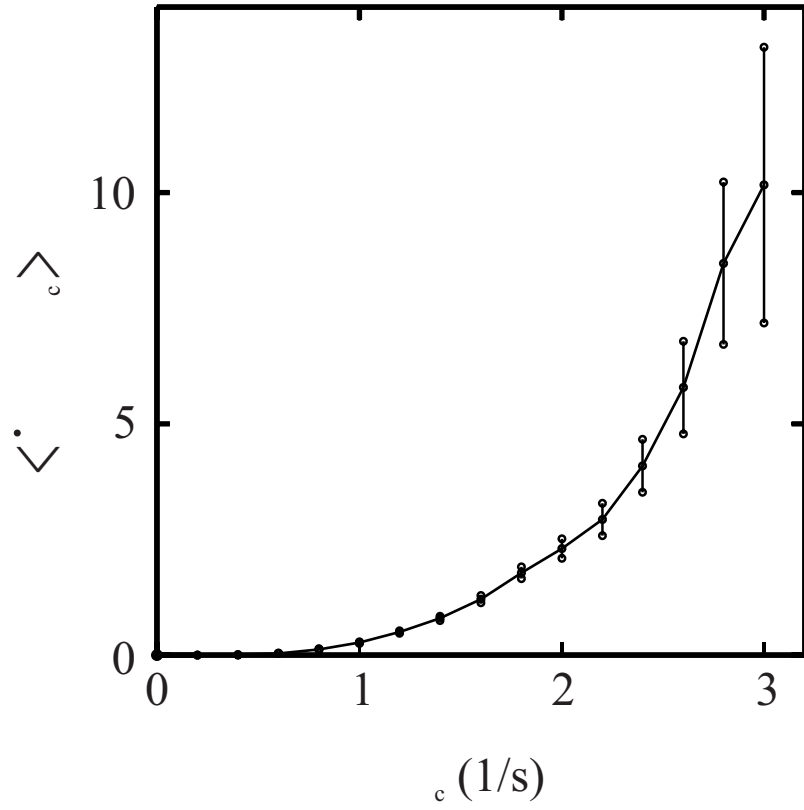


Figure 4.15: The average of ϵ conditioned on $\lambda_3 > \lambda_c$. The gradients are subject to a self-steepening mechanism, so when λ_3 is large, the dissipation is typically rising.

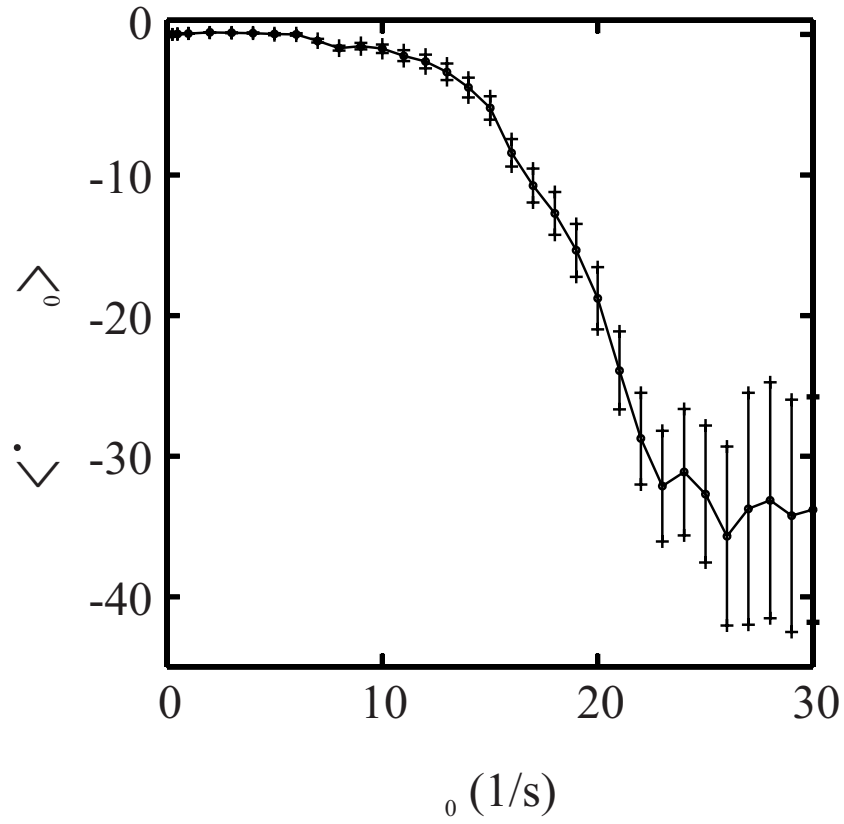


Figure 4.16: The average of ϵ conditioned on $\Omega > \Omega_0$. When the enstrophy is high, the dissipation is typically falling.

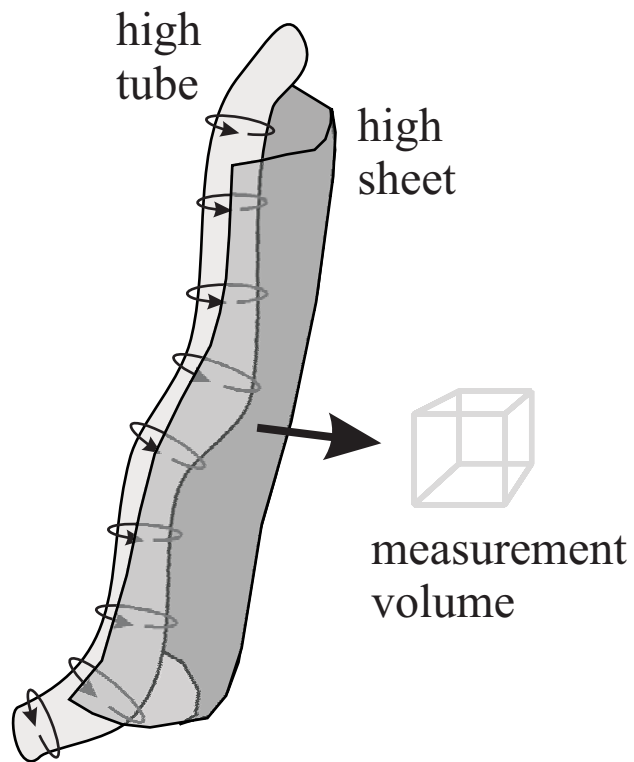


Figure 4.17: A vortex tube (high- Ω) and dissipation sheet (high- ϵ) passing through the measurement volume. The advection of such coherent structures offers one possible explanation for the observed statistics.

Stokes equation yields the following equation for the gradient matrix, \mathbf{M} :

$$\dot{\mathbf{M}} = -\mathbf{M}^2 - \Pi/\rho,$$

where Π is the pressure Hessian matrix. Breaking \mathbf{M} into symmetric and antisymmetric parts, $\mathbf{M} = \mathbf{S} + \mathbf{A}$ results in the following set of equations:

$$\dot{\mathbf{S}} = -\mathbf{S}^2 - \mathbf{A}^2 - \Pi/\rho \quad (4.5)$$

$$\dot{\mathbf{A}} = -\mathbf{SA} - \mathbf{AS}. \quad (4.6)$$

Rotated into a coordinate system to diagonalize \mathbf{S} , the matrix \mathbf{S} contains only the three strain eigenvalues, λ_i , and \mathbf{A} is comprised solely of the vorticity components, ω_i . Hence, Eq. 4.6 can be rewritten as $\dot{\vec{\omega}} = \mathbf{S}\vec{\omega}$. This equation underlies the vortex stretching mechanism whereby large strains cause the vorticity to grow. Along with the self-steepening of gradients, this mechanism suggests two sequences of events which might explain the observed statistics. In one possible sequence (Figure 4.18), a sheet of high dissipation develops at the boundary between two regions of flow moving in opposite directions. The underlying motion and a self-steepening instability causes the gradients and vorticity to rise rapidly. A Kelvin-Helmholtz instability develops and produces a vortex tube via the roll-up of the high- ϵ sheet. Vortex stretching causes the vorticity to grow rapidly. Since dissipation at the center of a vortex is low, ϵ begins to fall as the vorticity (or Ω) rises. The vortex then dissipates or is advected out of the measurement volume. In the first two frames of Fig. 4.18, both ϵ and Ω are non-zero, and they grow in tandem. In the second scenario (Figure 4.19), the initial flow has only dissipation ($\Omega = 0$), which

is amplified by self-steepening mechanisms. The vorticity is exponentially unstable (Eq. 4.6), so any small vorticity rapidly grows. The $-\mathbf{A}^2$ term in Eq. 4.5 suggests a mechanism by which high vorticity squelches the growth of the dissipation.

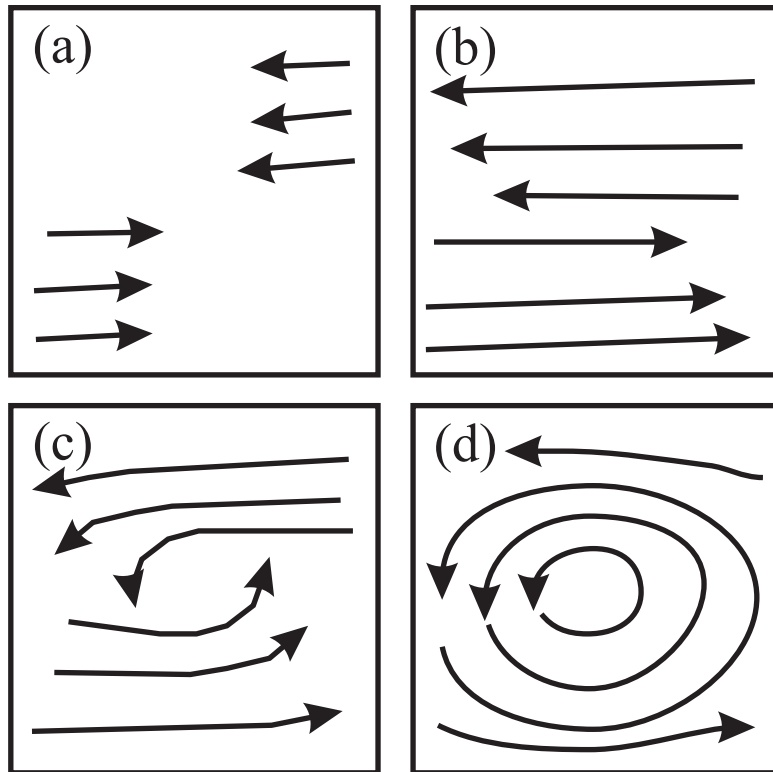


Figure 4.18: A possible sequence of events which could explain the observed statistics of ϵ and Ω . a) A region of high dissipation develops due to fluid motions. b) A self-steepening mechanism causes the gradients to grow rapidly, increasing both ϵ and Ω in tandem. c) An instability causes the formation of a vortex, which grows rapidly due to vortex stretching. d) As Ω rises, the dissipation falls.

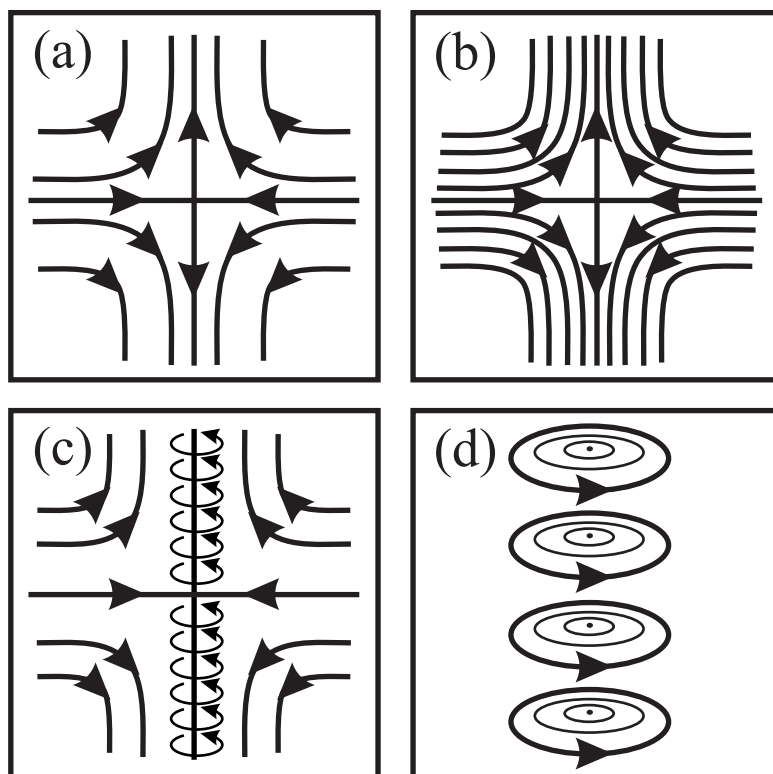


Figure 4.19: Another sequence of events which may explain the observed statistics of ϵ and Ω . a) & b) A region of high dissipation and zero vorticity develops and is amplified by self-steepening mechanisms. c) An instability produces a non-zero vorticity which grows exponentially due to vortex stretching. d) The dissipation falls rapidly.

4.2 Turbulent Rayleigh-Bénard Convection

Applying LH μ PIV to Rayleigh-Bénard convection presented challenges not present with grid-generated turbulence. Convective motions are driven by thermal density variations in the fluid. The same temperature variations that drive the flow also produce variations in the index of refraction n of the fluid. On a hot day, such thermal variations of n are visible above hot surfaces as a distorting waviness in the air. Similar distortion is visible in our tank when turbulent convection is occurring. The distortion is strongest near the top and bottom thermal boundary layers—that is, near the glass window and copper plate. LH μ PIV is an optical measurement technique and is very sensitive to optical distortion. Cameras 1 and 3, which look through the tank sides, are affected only slightly; particles drift in and out of focus but are still distinguishable. Camera 2, however, looks through the bottom glass plate and the thermal boundary layer. Index of refraction fluctuations produce wide variations in the focal plane of that camera, sometimes blurring the image beyond recognition. Figure 4.20 shows a sample blurry frame from camera 2. As long as the position of the laser sheets does not change, the imaged particles are in the correct plane even when they are out of focus. The laser sheets do not pass through the thermal boundary layers and are not subject to the strong fluctuations of n . The focus changes on a time scale much longer than the duration of a frame. Except in extreme cases, a cross-correlation can still be obtained, but the measurement error is significantly greater.

To set up a turbulent convective state, the heating bath was kept at a tem-

perature of 73 °C and the cooling bath at 10 °C. The temperature was monitored at the center of the tank and at two locations in the copper plate. No temperature difference could be measured between the two thermocouples at different heights in the copper, which both read 13 °C, so that was taken to be the temperature at the top interface. A temperature of 26 °C was measured at the center of the tank, giving an estimated 26 °C temperature difference across the convection cell. From Eq. 3.1, we find a Rayleigh number for the system of $Ra = 5.1 \times 10^9$. “Hard turbulent convection” occurs for $Ra > 10^9$.

Typical velocities in convection were smaller than in grid turbulence, so a frame rate of 60 frames/s was used. Additionally, the focusing difficulties necessitated the use of the camera’s full 480×420 resolution. Frames were subdivided into 3×3 subsections of size 192×144 pixels. Out of focus particle images result in blurrier cross-correlation peaks. A much larger radius, 15 pixels, was used for the weighted averaging.

Table 4.2 shows time averages of velocity components in turbulent convection. These measurements were taken at the center of the tank both vertically and horizontally. Unlike the grid turbulence, there appears to be no large scale pumping in convection; all $\langle v_i \rangle \approx 0$. As expected, though, the fluctuations in the y -directions are larger than those in the other two directions. This statistic is borne out by observations—large plumes are seen moving vertically but not horizontally.

The time average dissipation was $\langle \epsilon \rangle = 0.0232 \text{ cm}^2/\text{s}^3$. As in Sec. 4.1.2, this value can be used to determine η and Re : $\eta = 0.08 \text{ cm}$ and $Re = 1985$. Due to the inherent anisotropy in convection, R_λ depends on the direction used. For the x -

X	$\langle X \rangle$	σ_X
v_x	-0.02 cm/s	0.30 cm/s
v_y	0.07 cm/s	0.61 cm/s
v_z	0.01 cm/s	0.30 cm/s

Table 4.2: Time-average velocity components in turbulent convection.

and y -directions, we find $R_\lambda = 25$ and $R_\lambda = 112$, respectively.

It is much more common in the case of convection for one or more subsections to have spurious velocity data. When the particles go entirely out of focus, the cross-correlations tend to yield velocities of zero. Figure 4.21 shows an example of a subsection velocity trace with this problem. Such severe problems are atypical, and when they do occur, no more than 1 or 2 subsections of 27 are faulty. Velocity traces of the components of \vec{v}_0 reflect the increased noise (Figure 4.22), and the problems are compounded in the gradient components (Figure 4.23).

Due to the large number of spurious points in the convection data, it was impractical to apply the cleaning algorithm. Likewise, statistical analyzes of turbulent quantities in convection are very skewed by false high values. Distributions of some quantities will be discussed in the next section in relation to grid turbulence. Chapter 5 includes a discussion of ways in which the convection data could be extended and improved.

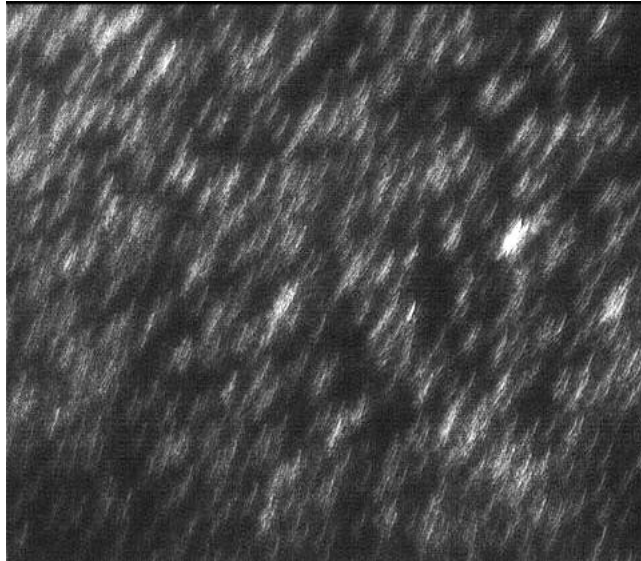


Figure 4.20: Sample frame of $1\ \mu\text{m}$ particles imaged through the thermal boundary layer. Temperature fluctuations in the fluid change the index of refraction and the focal depth.

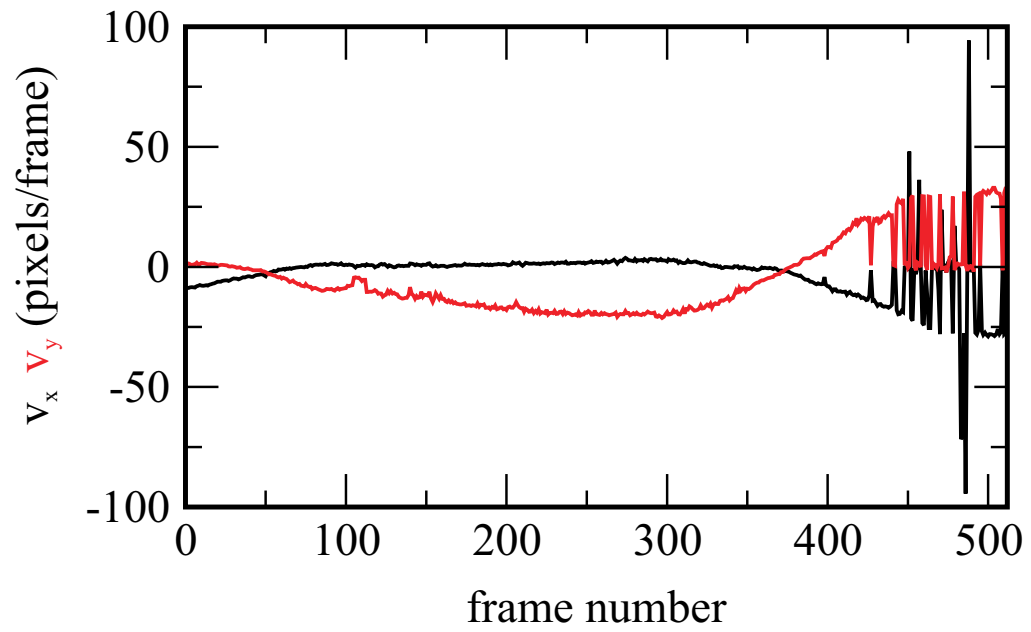


Figure 4.21: Subsection traces v_x and v_y for turbulent convection. Focusing problems results in poor cross-correlations that often show no velocity at all, as in the noisy section at the end.

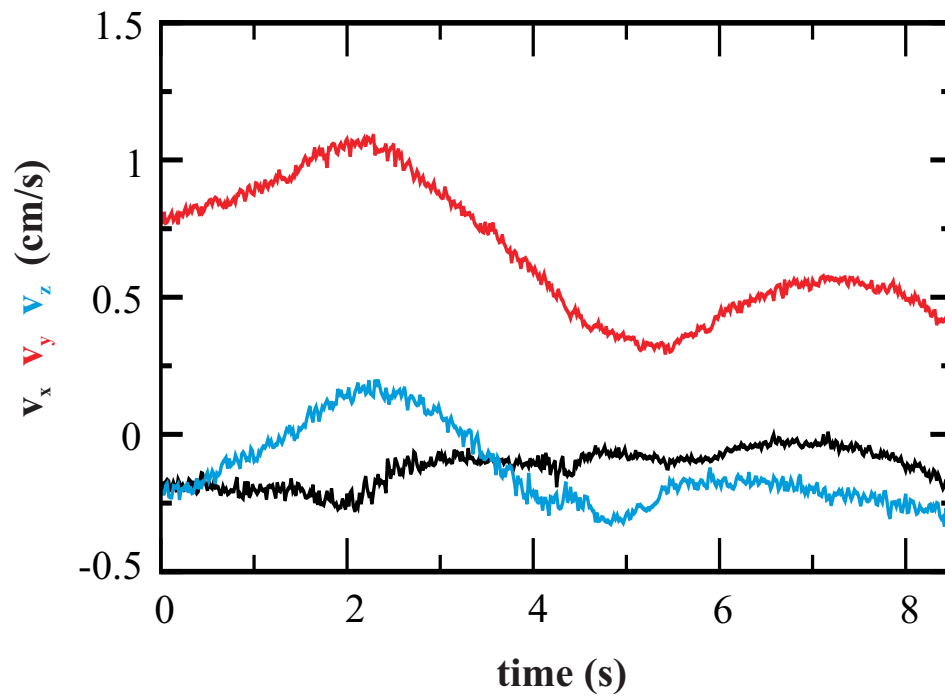


Figure 4.22: Traces of the three components of \vec{v}_0 for turbulent convection. The velocity measurement error is higher than in the case of grid-generated turbulence.

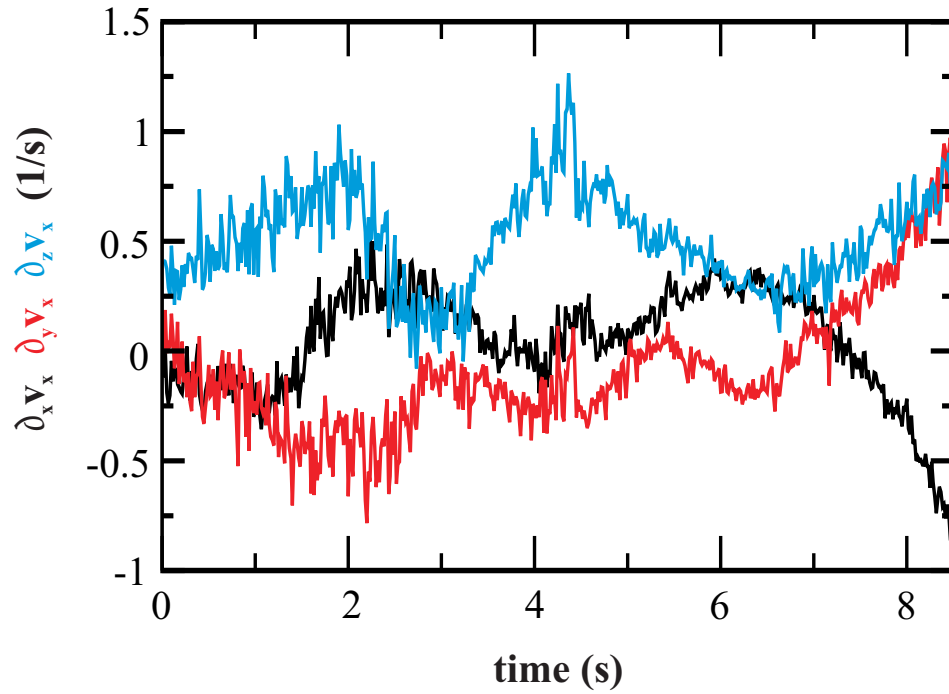


Figure 4.23: Typical traces of three components, $\partial v_x / \partial x$, $\partial v_x / \partial y$, and $\partial v_x / \partial z$, of the gradient matrix \mathbf{M} for turbulent convection. The gradients are calculated from spatial variations of measured velocity components. Hence, the noise is magnified in these quantities.

4.3 Grid/Convection Statistical Comparison

In Section 1.1.1, two hypotheses from Kolmogorov's 1941 theory were discussed. The first stated that at small (dissipative) length scales, the statistical properties of the fluid are universal and determined solely by the dissipation and viscosity. In other words, at these scales, the fluid has no knowledge of the mechanism by which the turbulence was produced. Appropriately nondimensionalized by ϵ and ν , the statistics of grid turbulence and convection should be the same.

Figures 4.24 and 4.25 show scaled helicity and dissipation distributions for both types of turbulence. In the central region of the helicity PDF, the statistics line up well. Only for events with a probability of less than 0.01 do the two diverge, with the tails of the convection distribution stretched to higher helicity values. The stretching is likely a result of spurious convection data for high values of h . The PDF of $\log(\epsilon/\langle\epsilon\rangle)$ shows the trend more clearly. For all values of ϵ up to those about 10 times the average, the statistics from grid and convection are virtually the same. Above that point, there is a shoulder in the convection distribution as the high- ϵ statistics become dominated by the noise. Undoubtedly, improved convection statistics would allow a more detailed comparison of the two, but it appears that the data do support the K41 hypothesis.

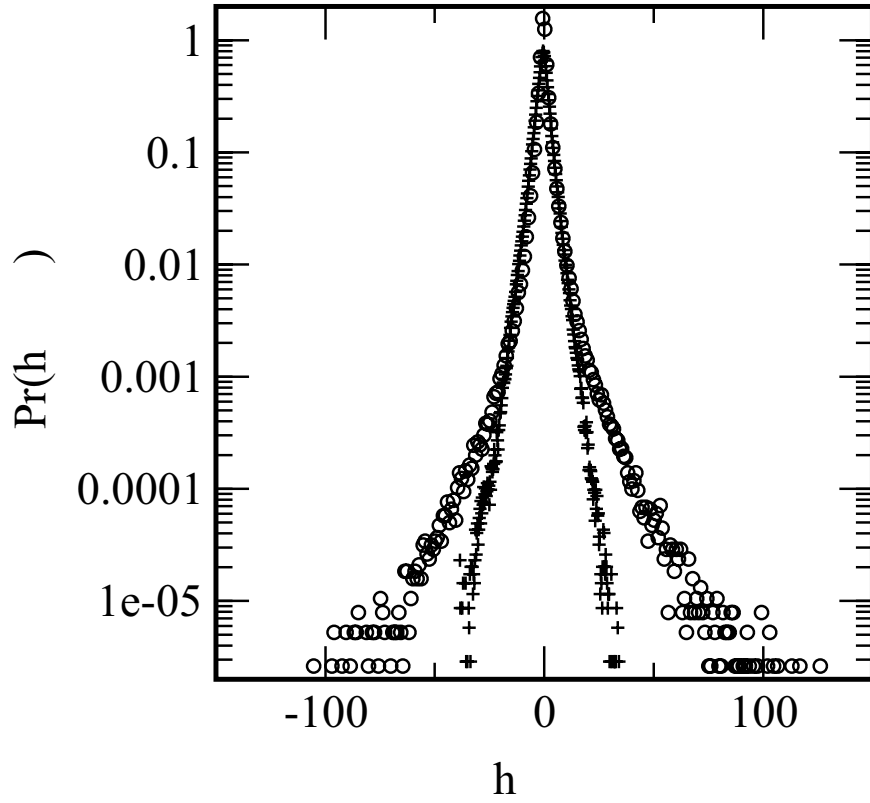


Figure 4.24: PDFs of the scaled helicity for grid turbulence (+) and turbulent convection (O).

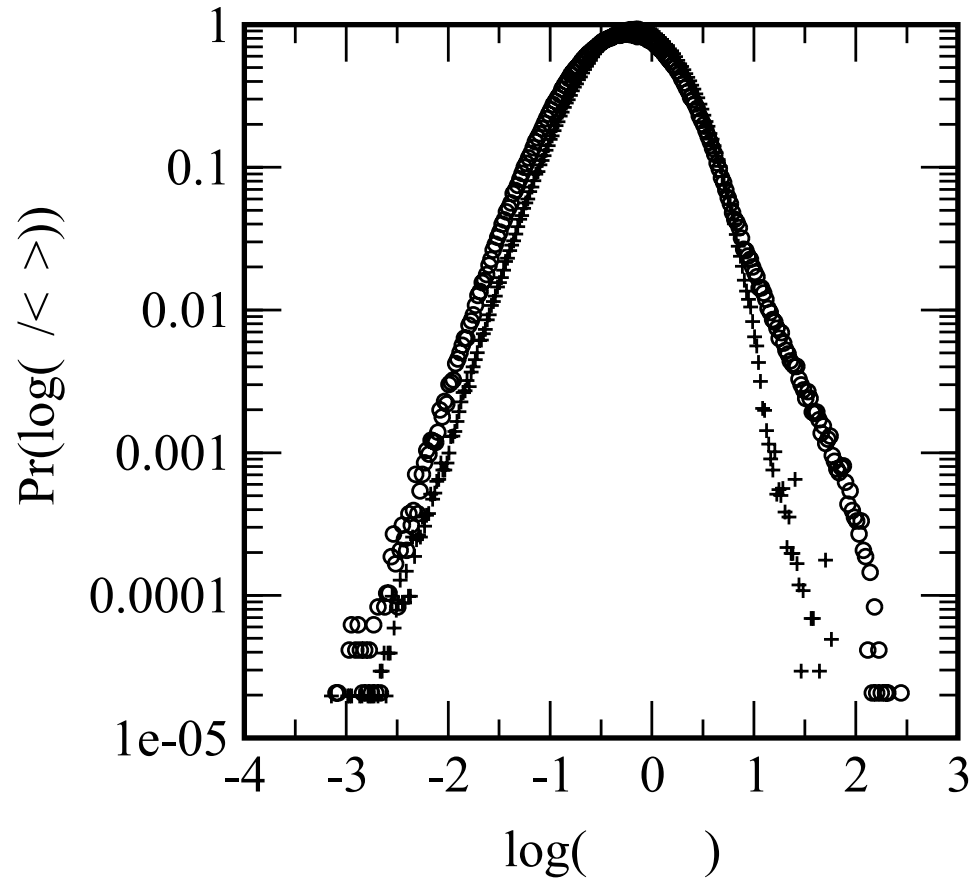


Figure 4.25: PDFs of the scaled dissipation for grid turbulence (+) and turbulent convection (O). Other than at very high values of ϵ , the statistics appear very similar.

Chapter 5

Conclusions

In a project such as this one, in which the development and initial application of a new measurement technique is realized, it is difficult to formulate a true “conclusion.” We developed LH μ PIV not to answer a single question about turbulent flows, but to offer a new tool with which to explore this fascinating phenomenon. Already, it has provided insights into the complex dissipation-scale dynamics of turbulence, and it is clear that there are many interesting aspects of turbulence still to be explored and understood. We are continuously honing the LH μ PIV system to improve its capabilities. The first runs of data gathering and analysis highlighted its strengths and weaknesses and pointed towards interesting phenomena which deserve further study.

Our observations of grid turbulence fall into one of two categories: reproduc-

tions or confirmations of published results and entirely new results. Since these experiments were the first with the LH μ PIV system, those results in the first category provided important evidence of the measurement technique's success. Having a time-resolved, three-dimensional data allowed us to create a more detailed picture of the interplay of dissipation and enstrophy. Time traces of high- ϵ and high- Ω events show that these quantities not only burst to high values, but that they sometimes do so at rates more suggestive of local singularities than exponential growth. The observed time dynamics shed light on the process by which intense regions of ϵ and Ω develop and interact. A rapid increase in the dissipation, possibly due to self-steepening of the gradients, sets off an intense event. In the presence of high gradients, a vortex stretching mechanism would rapidly amplify the enstrophy. The sudden rise in enstrophy is accompanied by a sudden drop dissipation, which is quickly followed by a drop in the enstrophy. No mechanism is supported by the data or analysis of the kinematics for this last step, the rapid decrease in enstrophy. It is clear, though, that an understanding of the temporal interactions between stretching and vorticity is crucial to understanding extreme events in turbulent flow systems.

A higher Re flow was desirable, but impractical in the grid-generated turbulence. At higher Re , turbulent quantities should be more intermittent, bursting more often and to higher values, and we expect to see more high-dissipation events which display power-law growth. The main limit on Re is essentially a problem of imaging: as Re increases, the Kolmogorov scale decreases. Already, we are using the long-distance microscope lenses near their magnification limit. Different objective

lenses or increasing the size of the tank would only allow a Re increase of 5 or so. An improvement in data quality for grid turbulence, however, is somewhat easier. Certainly, longer data sets can be taken. Fitting the velocity data to a quadratic model (one additional term in the Taylor series) might improve the data. It should be noted that the grid turbulence data has yet to be fully mined. With over 5,000,000 velocities and matrices measured, there is undoubtedly much to be discovered.

Perhaps more promising for future work, despite its challenges (or perhaps, because of them), is convection. Turbulent convection is an important and widely studied phenomenon. While oscillating double grid turbulence produces a reasonable approximation of isotropic turbulence, it is a highly artificial system which is difficult to characterize. In convection, the tank aspect ratio and the Rayleigh number provide a straightforward means to describe the fluid state. Velocity measurement techniques which can be applied to convection are limited, and techniques which can measure gradients are even more so. Fluctuations in the index of the refraction of the water are unavoidable. However, a number of changes could be made to the system which would improve our measurement capabilities. A simple solution would be to lower the temperature gradients. With a temperature drop of 26 °C across the convection cell, we are outside the regime in which the Boussinesq approximation is valid. Ra is linear in ΔT , so we could stay in the “hard turbulence” regime while decreasing the focusing problem, perhaps significantly. And, since $Ra \propto \ell^3$, slightly increasing the size of the tank could easily compensate for the lower temperature difference. Decreasing the aperture size on the camera lenses increases the depth of field and could be used to keep particles in focus even as the focal length shifts. The

corresponding decrease in light would need to be compensated for by increasing the particle size.

The available convection data points toward an entirely different possibility for improving data quality: use only the two side cameras. Of the 3 velocity components and 9 velocity gradients, only $\partial v_x/\partial z$ and $\partial v_z/\partial x$ cannot be measured in such a setup. Our data shows a high level of horizontal isotropy to the velocities and gradients. In fact, all gradient components have very similar behavior statistically, so it would be straightforward to approximate these two unmeasured quantities. A side-benefit of such a modification is that optical access would no longer be necessary through the bottom of the tank. The glass window could be replaced with a copper plate or other material with high thermal conductivity.

Improved convection statistics would allow a more detailed comparison with grid turbulence. One future goal is to measure how dissipation depends on the vertical position in the tank. By shifting the tank vertically, with or without the third camera looking upward through the bottom, we can measure dissipation from the center of the convection cell to one end. Likewise, horizontal translation of the tank could be used to map out the x - and z -dependence of ϵ .

We have demonstrated that LH μ PIV is a useful tool for studying turbulence. It extends the capabilities of previous Eulerian measurement techniques by simultaneously measuring all velocities and gradients in a fully time-resolved fashion. I hope that future applications of LH μ PIV will provide further insight into the nature of turbulence.

Appendix A

Analysis Software

A.1 Automation

The following shell script “doanal” was written to automate the data acquisition and analysis procedure (see Fig. 2.10). The script runs continuously on each of the processing computers, checking every second for a full-size AVI file. When a complete video has been saved, the script immediately runs the PIV analysis program on it, saves the velocity data to a another computer, then deletes or renames the original AVI file.

```
#!/bin/csh
while (1)
set list = `ls -l *.avi | sort -k5 | tail -n 1`
set size = `echo $list | awk '{print $5}'`
if ( $size == "103272960" ) then
```

```

date
set name = `echo $list | awk '{print substr($9,0,length($9)-4)}' `
echo $name is full size -- starting analysis
time piv2 $name.avi 2 > $name.dat
rcp $name.dat window.umd.edu:/bigdisk/wolf/020402/$name.dat
rm $name.dat
rm *.cfg *.cfg
rm $name.avi
else
sleep 1
endif
end

```

A.2 AVI File Format

The following is some relevant information about the storage of video data in an uncompressed AVI file format. This information may not be accurate for color videos or grayscale videos with > 8 bit depth.

BYTE #	INFORMATION
32-35	microseconds per frame
48-51	total number of frames
60-63	frame size in bytes
64-67	x-dimension of frame
68-71	y-dimension of frame
	...header ends at byte 4095...
	...starting at byte 4096...
8 bytes	frame 1 buffer
frame size bytes	frame 1 data
8 bytes	frame 2 buffer
frame size bytes	frame 2 data

A.3 PIV Analysis Code

This C program “piv.c” was written by Dr. Daniel P. Lathrop and me. The program, the backbone of the PIV analysis, takes in raw video data and outputs velocities for subsections in each frame pair.

```
/* This program takes in two frames, performs an NxN
 * cross-correlation, finds the peaks in each subdivisions,
 * calculates a weighted velocity for each subdivision, and outputs
 * outputs those values in pixels */

/* The command line is: piv file.avi N */

#include <stdio.h>
#include <stdlib.h>
#include <math.h>
#include <fft.h>

#define index1 i+lda*j
#define index2 ind+lda*jnd

main(argc, argv)
int argc;
char *argv[];
{
/* Declare all variables and arrays */
    double sumx,sumy,sumvx,sumvy;
    double sumw,sumvxv, sumyv, sumxvy, sumyvy, sumxy, sumx2, sumy2;
    double maxd=1e-6, mind=1e+20, sum, opow, mpow, good, maxgood;
    double w[45], vx[45], vy[45], px[45], py[45], px2[45], py2[45];
    double xcent[45], ycent[45];
    double dxx, dxy, dyx, dy, mvx, mvy, a[3][3], det, vx0, vy0;
    int xpeak, ypeak, filenum, job=-1;
    int N, oxlim, nxlim, oylim, nylin, subi, subj, xlim, ylim, lda=480, i, j;
    int whi, ymin, xmin, xmax, ymax, ind, jnd, bad;
    float test[480*420];
    float test2[480*420], last[4][4][480*420], *workspace;
    FILE *fpi;
    char header[100];
    char *avi;
    int xsize, ysize, howmany, avisize, framesize;
    int framestart2;

/* Get input file name and output file prefix from command line */
/* Open input file */
    if ((fpi=fopen(argv[1], "r"))==NULL) {
        fprintf(stderr, "File opened is stdin for input\n");
    }
}
```

```

        fpi=stdin;
    }
/* Read in first 100 bytes into header */
    fread(header, 100, 1, fpi);
/* Find xsize, ysize, # of frames, framesize, avisize from header*/
    xsize = (int)header[64] + (int)header[65]*256;
    ysize = (int)header[68] + (int)header[69]*256;
    howmany = (int)header[48] + (int)header[49]*256;
    framesize = xsize*ysize;
    avisize = 4096 + howmany*(8+framesize);
/* Print xsize, ysize, # of frames, framesize, & avisize to screen*/
    fprintf(stderr,"frame size %dx%d, %d frames\n", xsize, ysize,
            howmany);
    fprintf(stderr,"frame size %d, avi size %d\n", framesize,
            avisize);
/* Allocate memory for full avi file */
    avi = (char *) malloc(avisize);
/* setting the pointer back to the beginning of the file */
    fseek(fpi,-100,1);
/* Read in video data into avi */
    fread(avi, avisize, 1, fpi);
    sum=0;
/* Get arguments from command line */
    xlim=xsize;
    oxlim=xlim;
    lda=xlim;
    ylim=ysize;
    oylim=ylim;
    N=atoi(argv[2]);
    if (oxlim==480 && N==2) { nxlim=256; nyylim=256; }
    if (oxlim==480 && N==3) { nxlim=192; nyylim=144; }
    if (oxlim==480 && N==4) { nxlim=128; nyylim=128; }
    if (oxlim==480 && N==5) { nxlim=96; nyylim=96; }
    if (oxlim==320 && N==2) { nxlim=192; nyylim=192; }
    if (oxlim==320 && N==3) { nxlim=128; nyylim=96; }
    if (oxlim==320 && N==4) { nxlim=96; nyylim=72; }
    if (oxlim==240 && N==2) { nxlim=128; nyylim=108; }
    if (oxlim==240 && N==3) { nxlim=96; nyylim=96; }
/* Begin loop over files in directory */
    workspace=scfft2dui(nxlim,nyylim,NULL);
/* initialize last array for first frame */
    filenum=0;
    xlim=oxlim; ylim=oylim;
/* Read in frame 1 data */
    framestart2 = 4096 + 8*(filenum+1) + framesize*(filenum);
/* BEGIN subimage loop */
/* Loops from lower left to upper right in columns */
/* Define new limits */
    xlim=nxlim; lda=xlim+2; ylim=nyylim;
    for (subi=0; subi<N; subi++) {
        for (subj=0; subj<N; subj++) {
            xmin = subi*(oxlim-xlim)/(N-1); /* subimage limits */
            ymin = subj*(oylim-ylim)/(N-1);
/* Put subimages from two frames into an array */

```

```

    for (j=0; j<yylim; j++) {
    for (i=0; i<xylim; i++) {
        test2[index1]=avi[framestart2+i+xmin+oxlim*(j+ymin)];
    }
    for (i=xylim; i<xylim+2; i++) {
        test2[index1]=0;
    }
}
/* Start of fft and cross-correlation */
    job=-1;
    scfft2du(job,xylim,yylim,test2,lda,workspace);
    for (j=0; j<yylim; j++)
    for (i=0; i<lda; i++) {
        last[subi][subj][index1]=test2[index1];
    }
}
/* Start loop over rest of frames */
    for (filenum=1; filenum<howmany; filenum+=1) {
        xylim=oxylim; yylim=oyylim;
/* Read in frame data */
        framestart2 = 4096 + 8*(filenum+1) + framesize*(filenum);
/* BEGIN subimage loop */
/* Loops from lower left to upper right in columns */
/* Define new limits */
        xylim=nxylim; lda=xylim+2; yylim=nyylim;
        for (subi=0; subi<N; subi++) {
        for (subj=0; subj<N; subj++) {
            whi=(subi*N)+subj; /* which subimage */
            px[whi]=subi; py[whi]=subj; /* subimage coordinate */
            px2[whi]=px[whi]; py2[whi]=py[whi];
            xmin = subi*(oxylim-xylim)/(N-1); /* subimage limits */
            ymin = subj*(oyylim-yylim)/(N-1);
            xmax=xmin+xylim-1;
            ymax=ymin+yylim-1;
            xcent[whi]=(xmax+xmin)/2;
            ycent[whi]=(ymax+ymin)/2;
/* Put subimages from two frames into an array */
            for (j=0; j<yylim; j++) {
            for (i=0; i<xylim; i++) {
                test2[index1]=avi[framestart2+i+xmin+oxlim*(j+ymin)];
            }
            for (i=xylim; i<xylim+2; i++) {
                test2[index1]=0;
            }
        }
}
/* Start of fft and cross-correlation */
    job=-1;
    scfft2du(job,xylim,yylim,test2,lda,workspace);
    for (j=0; j<yylim; j++)
    for (i=0; i<lda; i+=2) {
        test[index1]=last[subi][subj][index1]*test2[index1]
            +last[subi][subj][index1+1]*test2[index1+1];
        test[index1+1]=-last[subi][subj][index1]*test2[index1+1]
            +last[subi][subj][index1+1]*test2[index1];
    }
}
/* Now rewrite last to be for the current frame */

```

```

        for (j=0; j<yylim; j++)
        for (i=0; i<llda; i++) {
            last[subi][subj][index1]=test2[index1];
        }
/* It's time for the inverse transform */
    job=1;
    csfft2du(job,xlim,yylim,test,lda,workspace);
/* Find maximum and minimum values in cross-correlated data */
    sum=0;
    maxd=1e-6; mind=1e+20;
    for (j=0; j<yylim; j++)
    for (i=0; i<xylim; i++) {
        if (test[index1]>maxd) {
            maxd=test[index1];
            xpeak=i; ypeak=j;
        }
        if (test[index1]<mind) mind=test[index1];
    }
/* Define a velocity and weight using the Everest of peaks */
    vx[whi]=0; vy[whi]=0;
    sum=0; sumx=0; sumy=0;
    for (i=xpeak-2; i<xpeak+3; i++) /* sum over 225 pixels */
    for (j=ypeak-2; j<ypeak+3; j++) {
        ind=i; jnd=j;
        if (i<0) ind=xlim+i;
        if (i>xylim-1) ind=i-xylim;
        if (j<0) jnd=yylim+j;
        if (j>yylim-1) jnd=j-yylim;
        sum+=(test[index2]-mind)*(test[index2]-mind)*
            (test[index2]-mind);
        sumx+=i*(test[index2]-mind)*(test[index2]-mind)*
            (test[index2]-mind);
        sumy+=j*(test[index2]-mind)*(test[index2]-mind)*
            (test[index2]-mind);
    }
    vx[whi]=sumx/sum;
    vy[whi]=sumy/sum;
    w[whi]=1;
    if (vx[whi]<nxlim/2) vx[whi]=-vx[whi];
    if (vx[whi]>(nxlim/2-1)) vx[whi]=(nxlim-vx[whi]);
    if (vy[whi]<nyylim/2) vy[whi]=-vy[whi];
    if (vy[whi]>(nyylim/2-1)) vy[whi]=(nyylim-vy[whi]);
/* End subimage loop */
    }}
/* Write out data for the subsections */
    xlim=N*N;
    for (j=0; j<xylim; j++) {
        printf("%d vx %3.2f wx %3.3f vy %3.2f wy %3.3f vz 0 wz
            0 x %3.1f y %3.1f z 0\n",filenum,vx[j],w[j],vy[j],
            w[j],xcent[j],ycent[j]);
    }
/* End file loop */
    }
free(avi);

```

```

/* End main */
}

```

A.4 Linear Least Squares Code

This Fortran 90 program “frag.f90” performs a linear least squares fit of the velocity data to the divergence-free three-dimensional model of Eq. 2.1. The program was written for us by Dr. Eric J. Kostelich (Arizona State University). In addition to the $\vec{\nabla} \cdot \vec{v} = 0$ linear model, the program can fit the data to a quadratic model or a non-divergence-free linear model. Only the divergence-free linear model was used for the data presented in this dissertation.

```

!-----
  module fitparams
! FITPARAMS - various global data constants that are appropriate for
! the fitting the various models.
! RCOND : the relative condition number to use for the least squares.
!         More or less, given the scaling of the data, we treat numbers
!         less than RCOND as 0.
! MAXDAT : the maximum number of equations of condition for a given component
!         of the velocity.
! MAXTIME : maximum number of frames (time steps) that we can process
! COUNT : (k,m)th entry holds the number of equations of condition
!         for coordinate k in frame m (coord 1 = x, coord 2 = y,
!         coord 3 = z).
! EVX : (j,k,m)th entry holds, for frame m, the kth component of the
!         jth position vector (which corresponds to the jth measurement
!         of V_X). We use the convention K=1 <-> X, K=2 <-> Y, K=3 <-> Z.
! VXM : (j,m)th entry holds, for frame m, the jth measurement of V_X.
!         Similarly for VYM, VZM.
! COUNT, EV[XYZ] and V[XYZ]M are set in read_data and otherwise remain
! unchanged throughout the program.
!
  integer,parameter::MAXDAT=50
  integer,parameter::MAXTIME=2048
  integer,parameter::STDERR=0 !for standard error output

```

```

real,save::rcond=1.0e-3
real,save::divweight=0.0
logical,save::forced_divfree=.false.
integer,save::count(3,MAXTIME)
real,save::evx(MAXDAT,4,MAXTIME)
real,save::evy(MAXDAT,4,MAXTIME)
real,save::evz(MAXDAT,4,MAXTIME)
real,save::vxm(MAXDAT,MAXTIME)
real,save::vym(MAXDAT,MAXTIME)
real,save::vzm(MAXDAT,MAXTIME)
end module fitparams
-----
! FRAG - Process all frame data in the format produced by crosscam and docam
! and output the velocity data.
!
program frag
use fitparams
implicit none
integer::nframes,omitted,j,info
logical::quadratic
external simple_linear,simple_quadratic,divfree_linear,forced_divfree_linear
!
call trap(1) !crash on floating-point exception
call parseline(quadratic)
call read_data(nframes,omitted)
if(nframes.eq.0) then
write(STDERR,900)
call exit(1)
endif
900 format('No frames in data file!')
if(omitted.gt.0) write(STDERR,910) omitted
910 format('Warning:',i6,' data values omitted due to lack of space')
!
! Do fits for all frames
!
if(quadratic) then
call doit(simple_quadratic,nframes)
else if(divweight.gt.0.0) then
call doit(divfree_linear,nframes)
else if(forced_divfree) then
call doit(forced_divfree_linear,nframes)
else
call doit(simple_linear,nframes)
endif
call exit(0)
end program frag
-----
! DOIT - fit the least-squares according to the indicated model
! and print the results.
!
subroutine doit(model,nframes)
implicit none
external model
integer,intent(in)::nframes

```

```

!
! Local variables
!
  real::beta(4,3),div,varexp
  integer::info,j
  real,external::div_measure,r2
!
! Rescale dxvx terms to account for scaling of pixel data by 0.01 in read_data
!
  do j=1,nframes
    call model(j,beta,info)
    if(info.ge.0) then
      write(6,100) 'vx: ',j,beta(1:4,1)
      write(6,100) 'vy: ',j,beta(1:4,2)
      write(6,100) 'vz: ',j,beta(1:4,3)
      div=div_measure(beta)
varexp=r2(j,beta)
      write(6,100) 'div:',j,div
      write(6,100) 'r2: ',j,varexp
    else
      write(6,101) j,info
    endif
  enddo
100 format(a,i4,4es11.3)
101 format('fail!',2i6)
  return
  end subroutine doit
!-----
  subroutine fit(x,ldx,nobs,y,beta,npar,rank)
!
! FIT - Fit a model of the form  $Y = X*beta$ , where Y is NOBSxNRHS,
!       X is NOBSxNPAR and BETA is NPARxNRHS.
! Arguments:
! X   :=: NOBS x NPAR matrix of observations.  Overwritten on return.
! LDX :   leading dimension of X; LDX >= NOBS.
! Y   :=: NOBS vector giving right-hand side.  Overwritten on return.
! BETA := NPAR vector of fitted parameters
! RANK := On return, an estimate of the numerical rank of the problem (<=NPAR).
! RANK := On return, effective rank of the problem; negative if an
!          error occurred.
!
! The problem must be overdetermined (NOBS > NPAR), otherwise an error code
! (RANK = -1) is returned.
!
  use fitparams,only:rcond,MAXDAT
  implicit none
! Arguments
!
  integer,intent(in)::nobs,npar,ldx
  integer,intent(out)::rank
  real,intent(out)::beta(npar)
  real,intent(inout)::x(ldx,npar),y(nobs)
!

```

```

! Local variables
!
  integer,parameter::NRHS=1      !placeholder to remember order of arguments
  real::work(max(min(nobs, npar)+3*npar, 2*max(nobs, npar)+NRHS))
  integer::j, info, jpvt(npar)
!
! Make sure that the problem is overdetermined; set error flag otherwise
!
  if(nobs.lt.npar.or.ldx.lt.nobs) then
    rank=-1
    return
  endif
!
! Compute QR decomposition and fit parameters.
!
  jpvt(:)=0
  call sgelsx(nobs, npar, NRHS, x, ldx, y, nobs, jpvt, rcond, rank, work, info)
  if(info.lt.0) then ! oops
    rank=info
  else
    beta(1:npar)=y(1:npar)
  endif
  return
end subroutine fit
-----
  subroutine parseline(quadratic)
! PARSELINE : parse execute line.
! Format: frag [-r rcond] [-q (quadratic fit)] [-d divfree_weight] [file]
! Defaults: rcond=1.0e-03, linear fit, no divergence free enforcement
! QUADRATIC := set to true if we should fit an unconstrained quadratic map.
!
  use fitparams
  implicit none
  logical, intent(out)::quadratic
!
! Local variables
!
  character(len=80)::optarg
  integer::iopt, optind, nargs
  integer, external::iargc
  character::arg
!
  quadratic=.false. ! default
  do
    call getopt(iopt, optarg, optind, 'r:qd:D')
    if(iopt.le.0) exit
    arg=char(iopt)
    select case(arg)
    case('r')
      read(optarg, 100) rcond
100    format(e16.0)
    case('q')
      quadratic=.true.
    case('d')

```

```

        read(optarg,100) divweight
        case('D')
forced_divfree=.true.
        case default
            write(STDERR,990) arg
990         format('unknown argument ',a)
            call exit(1)
        end select
    enddo
nargs=iargc()
if(optind.le.nargs) then !read from indicated file instead of stdin
    close(5)
    call getarg(optind,optarg)
    open(unit=5,file=optarg,status='old')
endif
return
end subroutine parseline
!-----
    subroutine read_data(nframes,omitted)
! Sets up basic equations of condition for each component of velocity.
! NFRAMES := the number of frames in the data (crude check based on
! input from crosscam/docam.
! OMITTED := number of data points omitted because of lack of storage
! (to fix this, increase MAXTIMES in module fitparams).
!
    use fitparams
    implicit none
    integer,intent(out)::nframes,omitted
!
! Local variables
!
    integer::k,time,nvx,nvy,nvz,omitted
    real::vx,wvx,vy,wvy,vz,wvz,x,y,z
!
    omitted=0
    nframes=0
!
! COUNT := (k,m)th entry holds the number of equations of condition
!         for coordinate k in frame m (coord 1 = x, coord 2 = y,
!         coord 3 = z).
! EVX := (j,k,m)th entry holds, for frame m, the kth component of the
!         jth position vector (which corresponds to the jth measurement
!         of V_X). We use the convention K=1 <-> X, K=2 <-> Y, K=3 <-> Z.
! VXM := (j,m)th entry holds, for frame m, the jth measurement of V_X.
!         Similarly for VYM, VZM.
!
    count(:,:)=0
    do
        read(5,*,end=10) time,vx,wvx,vy,wvy,vz,wvz,x,y,z ! until EOF
        x=x*0.01
        y=y*0.01
        z=z*0.01
        if(vx.ne.0.0) then
            count(1,time)=count(1,time)+1

```

```

nvx=count(1,time)
if(nvx.le.MAXDAT) then
  vxm(nvx,time)=vx*vwvx
  evx(nvx,1,time)=x
  evx(nvx,2,time)=y
  evx(nvx,3,time)=z
  evx(nvx,4,time)=wvx
  nframes=max(nframes,time)
else
  omitted=omitted+1
endif
endif
if(vy.ne.0.0) then
  count(2,time)=count(2,time)+1
  nvy=count(2,time)
  if(nvy.le.MAXDAT) then
    vym(nvy,time)=vy*vwvy
    evy(nvy,1,time)=x
    evy(nvy,2,time)=y
    evy(nvy,3,time)=z
    evy(nvy,4,time)=wvy
    nframes=max(nframes,time)
  else
    omitted=omitted+1
  endif
endif
if(vz.ne.0.0) then
  count(3,time)=count(3,time)+1
  nvz=count(3,time)
  if(nvz.le.MAXDAT) then
    vzm(nvz,time)=vz*vwvz
    evz(nvz,1,time)=x
    evz(nvz,2,time)=y
    evz(nvz,3,time)=z
    evz(nvz,4,time)=wvz
    nframes=max(nframes,time)
  else
    omitted=omitted+1
  endif
endif
enddo
10 continue
return
end subroutine read_data

```

```

  subroutine simple_linear(frame,beta,info)
! SIMPLE_LINEAR : fit a simple linear model for the velocity vectors.
! The Jth equation of condition for the measured X component of velocity
! is vxm(j)=beta(1:4,j).dot.evx(j,1:4) (and likewise for Y and Z components)
! where evx(1:3,j) correspond to (x,y,z) positions for the Jth subframe
! and evx(4,j) is the weight given to the constant offset (and likewise
! for the Y and Z components). This means that beta(1:3,1) holds
! (dxvx, dyvx, dzvx) respectively, and beta(4,1) is the v_x offset.
! beta(:,2) and beta(:,3) hold the parameters for the Y and Z coordinate,

```

```

! respectively.
! INFO := on return, 0 means that all least-squares calculations
!         proceeded normally.
!
!   use fitparams
!   integer,intent(in)::frame
!   real,intent(out)::beta(4,3)
!   integer,intent(out)::info
!
! Local variables
!
!   integer,parameter::NPAR=4
!   real::v(MAXDAT),x(MAXDAT,NPAR)
!   integer::rank,n
!
! Fit X coordinate data
!
!   n=count(1,frame)
!   v(1:n)=vxm(1:n,frame)
!   x(:,:)=evx(:, :,frame)
!   call fit(x,MAXDAT,n,v,beta,NPAR,rank)
!   if(rank.le.0) goto 90
!
! Fit Y coordinate data
!
!   n=count(2,frame)
!   v(1:n)=vym(1:n,frame)
!   x(:,:)=evy(:, :,frame)
!   call fit(x,MAXDAT,n,v,beta(1,2),NPAR,rank)
!   if(rank.le.0) goto 90
!
! Fit Z coordinate data
!
!   n=count(3,frame)
!   v(1:n)=vzm(1:n,frame)
!   x(:,:)=evz(:, :,frame)
!   call fit(x,MAXDAT,n,v,beta(1,3),NPAR,rank)
!   if(rank.le.0) goto 90
!   info=0
!   return
!
! Error occurred
!
90 continue
!   info=-1
!   return
!   end subroutine simple_linear
!-----
!   subroutine simple_quadratic(frame,beta,info)
! SIMPLE_QUADRATIC - fit a model that is linear in the parameters but
! includes quadratic terms in the position variables.
! No effort is made to enforce divergence-free conditions on the computed
! parameters.
! In each equation of condition, the position variables occur in the

```

```

! order x y z w x^2 y^2 z^2 xy yz xz, where w is the weight ascribed to
! the constant term.
! INFO := on return, 0 means that all least-squares calculations
!         proceeded normally.
!
      use fitparams
      integer,intent(in)::frame
      real,intent(out)::beta(4,3)
      integer,intent(out)::info
!
! Local variables
!
      integer,parameter::NPAR=10
      real::v(MAXDAT),x(MAXDAT,NPAR),param(NPAR)
      integer::rank,n
!
! Fit X coordinate data
!
      n=count(1,frame)
      v(1:n)=vxm(1:n,frame)
      x(:,1:4)=evx(:,1:4,frame)
      x(1:n,5)=evx(1:n,1,frame)**2   ! x^2 terms
      x(1:n,6)=evx(1:n,2,frame)**2   ! y^2 terms
      x(1:n,7)=evx(1:n,3,frame)**2   ! z^2 terms
      x(1:n,8)=evx(1:n,1,frame)*evx(1:n,2,frame) ! xy terms
      x(1:n,9)=evx(1:n,1,frame)*evx(1:n,3,frame) ! xz terms
      x(1:n,10)=evx(1:n,2,frame)*evx(1:n,3,frame) ! yz terms
      call fit(x,MAXDAT,n,v,param,NPAR,rank)
      if(rank.le.0) goto 90
      beta(1:4,1)=param(1:4) ! ignore parameters for quadratic terms
!
! Fit Y coordinate data
!
      n=count(2,frame)
      v(1:n)=vym(1:n,frame)
      x(:,1:4)=evy(:,1:4,frame)
      x(1:n,5)=evy(1:n,1,frame)**2   ! x^2 terms
      x(1:n,6)=evy(1:n,2,frame)**2   ! y^2 terms
      x(1:n,7)=evy(1:n,3,frame)**2   ! z^2 terms
      x(1:n,8)=evy(1:n,1,frame)*evy(1:n,2,frame) ! xy terms
      x(1:n,9)=evy(1:n,1,frame)*evy(1:n,3,frame) ! xz terms
      x(1:n,10)=evy(1:n,2,frame)*evy(1:n,3,frame) ! yz terms
      call fit(x,MAXDAT,n,v,param,NPAR,rank)
      if(rank.le.0) goto 90
      beta(1:4,2)=param(1:4) ! ignore parameters for quadratic terms
!
! Fit Z coordinate data
!
      n=count(3,frame)
      v(1:n)=vzm(1:n,frame)
      x(:,1:4)=evz(:,1:4,frame)
      x(1:n,5)=evz(1:n,1,frame)**2   ! x^2 terms
      x(1:n,6)=evz(1:n,2,frame)**2   ! y^2 terms
      x(1:n,7)=evz(1:n,3,frame)**2   ! z^2 terms

```

```

x(1:n,8)=evz(1:n,1,frame)*evz(1:n,2,frame) ! xy terms
x(1:n,9)=evz(1:n,1,frame)*evz(1:n,3,frame) ! xz terms
x(1:n,10)=evz(1:n,2,frame)*evz(1:n,3,frame) ! yz terms
call fit(x,MAXDAT,n,v,param,NPAR,rank)
if(rank.le.0) goto 90
beta(1:4,3)=param(1:4) ! ignore parameters for quadratic terms
info=0
return
!
! Error occurred
!
90 continue
info=-1
return
end subroutine simple_quadratic
!-----
subroutine divfree_linear(frame,beta,info)
! DIVFREE_LINEAR : fit a simple linear model for the velocity vectors,
! but add an extra equation of condition that requires
! dxvx+dyvy+dzvz=0, and weight it according to the amount specified
! on the command line.
! The Jth equation of condition for the measured X component of velocity
! is vxm(j)=beta(1:4,j).dot.evx(j,1:4) (and likewise for Y and Z components)
! where evx(1:3,j) correspond to (x,y,z) positions for the Jth subframe
! and evx(4,j) is the weight given to the constant offset (and likewise
! for the Y and Z components). This means that beta(1:3,1) holds
! (dxvx, dyvx, dzvx) respectively, and beta(4,1) is the v_x offset.
! beta(:,2) and beta(:,3) hold the parameters for the Y and Z coordinate,
! respectively.
! INFO := on return, 0 means that all least-squares calculations
! proceeded normally.
!
! use fitparams
! implicit none
! integer,intent(in)::frame
! real,intent(out)::beta(4,3)
! integer,intent(out)::info
!
! Local variables
!
! integer,parameter::NPAR=12
! real::weight
! real::v(MAXDAT*3+1),x(MAXDAT*3+1,NPAR),param(NPAR)
! integer::rank,n,offset
!
! Initialize
!
! x(:,:)=0.0
! if(divweight.le.0.0) then ! use reasonable default
! weight=1.0
! else
! weight=divweight
! endif
!

```

```

! Copy equations of condition for X components of velocity
!
  n=count(1,frame)
  v(1:n)=vxm(1:n,frame)
  x(1:n,1:4)=evx(1:n,1:4,frame)
  offset=n
!
! Copy equations of condition for Y components of velocity
!
  n=count(2,frame)
  v(offset+1:offset+n)=vym(1:n,frame)
  x(offset+1:offset+n,5:8)=evy(1:n,1:4,frame)
  offset=offset+n
!
! Copy equations of condition for Z components of velocity
!
  n=count(3,frame)
  v(offset+1:offset+n)=vzm(1:n,frame)
  x(offset+1:offset+n,9:12)=evz(1:n,1:4,frame)
  offset=offset+n
!
! Add equation of condition for divergence free parameters
!
  n=offset+1
  v(n)=0.0
  x(n,1)=weight
  x(n,6)=weight
  x(n,11)=weight
!
! Do least-squares and copy velocity coefficients
!
  call fit(x,MAXDAT*3+1,n,v,param,NPAR,rank)
  if(rank.le.0) goto 90
  beta(1:4,1)=param(1:4)
  beta(1:4,2)=param(5:8)
  beta(1:4,3)=param(9:12)
  info=0
  return
!
! Error occurred
!
90 continue
  info=-1
  return
end subroutine divfree_linear
-----
  subroutine forced_divfree_linear(frame,beta,info)
! FORCED_DIVFREE_LINEAR : fit a simple linear model for the velocity vectors,
! subject to the linear constraint that dxvx+dyvy+dzvz=0.
! The Jth equation of condition for the measured X component of velocity
! is vxm(j)=beta(1:4,j).dot.evx(j,1:4) (and likewise for Y and Z components)
! where evx(1:3,j) correspond to (x,y,z) positions for the Jth subframe
! and evx(4,j) is the weight given to the constant offset (and likewise
! for the Y and Z components). This means that beta(1:3,1) holds

```

```

! (dxvx, dyvx, dzvx) respectively, and beta(4,1) is the v_x offset.
! beta(:,2) and beta(:,3) hold the parameters for the Y and Z coordinate,
! respectively.
! INFO := on return, 0 means that all least-squares calculations
!         proceeded normally.
!
!   use fitparams
!   implicit none
!   integer,intent(in)::frame
!   real,intent(out)::beta(4,3)
!   integer,intent(out)::info
!
! Local variables
!
!   integer,parameter::NPAR=12
!   integer,parameter::NCONSTRAINT=1
!   integer,parameter::LWORK= &
!       NCONSTRAINT+min(MAXDAT*3,NPAR)+max(MAXDAT*3,NPAR)*32
!   real::weight
!   real::v(MAXDAT*3),x(MAXDAT*3,NPAR),work(LWORK)
!   real::param(NPAR),constraint(NPAR),zero(NCONSTRAINT)
!   integer::info,n,offset
!
! Initialize
!
!   constraint(:)=0.0
!   constraint(1)=1.0
!   constraint(6)=1.0
!   constraint(11)=1.0
!   zero(:)=0.0
!   x(:,:)=0.0
!
! Copy equations of condition for X components of velocity
!
!   n=count(1,frame)
!   v(1:n)=vxm(1:n,frame)
!   x(1:n,1:4)=evx(1:n,1:4,frame)
!   offset=n
!
! Copy equations of condition for Y components of velocity
!
!   n=count(2,frame)
!   v(offset+1:offset+n)=vym(1:n,frame)
!   x(offset+1:offset+n,5:8)=evy(1:n,1:4,frame)
!   offset=offset+n
!
! Copy equations of condition for Z components of velocity
!
!   n=count(3,frame)
!   v(offset+1:offset+n)=vzm(1:n,frame)
!   x(offset+1:offset+n,9:12)=evz(1:n,1:4,frame)
!   offset=offset+n
!
! Do least-squares and copy velocity coefficients

```

```

!
n=offset
call sgglse(n,NPAR,NCONSTRAINT,x,MAXDAT*3,constraint,NCONSTRAINT, &
    v,zero,param,work,LWORK,info)
if(info.lt.0) goto 90
beta(1:3,1)=param(1:3)*0.01
beta(4:4,1)=param(4)
beta(1:3,2)=param(5:7)*0.01
beta(4:4,2)=param(8)
beta(1:3,3)=param(9:11)*0.01
beta(4:4,3)=param(12)
return
!
! Error occurred
!
90 continue
    info=-1
    return
end subroutine forced_divfree_linear
-----
    real function div_measure(beta)
! DIV_MEASURE - return a measure of the divergence of the computed
! velocity parameters
!
    real,intent(in)::beta(4,3)
!
! Local variables
!
    real::dv(3)
!
    dv(1)=beta(1,1)
    dv(2)=beta(2,2)
    dv(3)=beta(3,3)
    div_measure=sum(dv)**2/dot_product(dv,dv)
    return
end function div_measure
-----
    real function r2(frame,beta)
! R2 - Return the RATIO of the variance in the predicted velocities
! (using the linear part of the model) compared to the variance
! in the raw data.
! This is NOT the same as the fraction of the variance
! explained by the linear regression itself.
!
    use fitparams
    implicit none
    integer,intent(in)::frame
    real,intent(in)::beta(4,3)
!
! Local variables
!
    real::totvar(3) ! total variance in each coordinate
    real::regvar(3) ! variance per coordinate after regression
    real::vavg,v(MAXDAT)

```

```

integer::n
!
! Look at X coordinates first - use all equations of condition
!
n=count(1,frame)
vavg=sum(vxm(1:n,frame))/n
v(1:n)=vxm(1:n,frame)
totvar(1)=dot_product(v(1:n),v(1:n))
v(1:n)=vxm(1:n,frame)-matmul(evx(1:n,1:4,frame),beta(1:4,1))
regvar(1)=dot_product(v(1:n),v(1:n))
!
! Likewise for Y coordinates ...
!
n=count(2,frame)
vavg=sum(vym(1:n,frame))/n
v(1:n)=vym(1:n,frame)
totvar(2)=dot_product(v(1:n),v(1:n))
v(1:n)=vym(1:n,frame)-matmul(evy(1:n,1:4,frame),beta(1:4,2))
regvar(2)=dot_product(v(1:n),v(1:n))
!
! ... and Z coordinates
!
n=count(3,frame)
vavg=sum(vzm(1:n,frame))/n
v(1:n)=vzm(1:n,frame)
totvar(3)=dot_product(v(1:n),v(1:n))
v(1:n)=vzm(1:n,frame)-matmul(evz(1:n,1:4,frame),beta(1:4,3))
regvar(3)=dot_product(v(1:n),v(1:n))
r2=1-sum(regvar)/20000
return
end function r2

```

BIBLIOGRAPHY

- [1] C.L.M.H. Navier, *Mém. Acad. Roy. Sci.* **6**, 389 (1823).
- [2] S. Rahmstorf, *Nature*, **288**, 825 (1997).
- [3] E.N. Lorenz, *J. Atmos. Sci.* **20**, 130 (1963).
- [4] E. Villermaux, H. Chaté, and J.-M. Chomaz, in *Mixing: Chaos and Turbulence*, edited by H. Chaté, E. Villermaux, and J.-M. Chomaz (Klewer Academic/Plenum Publishers, New York, 1999), p. 1.
- [5] S.B. Pope, *Annu. Rev. Fluid. Mech.* **26**, 23 (1994).
- [6] E.J. Hinch, in *Mixing: Chaos and Turbulence*, edited by H. Chaté, E. Villermaux, and J.-M. Chomaz (Klewer Academic/Plenum Publishers, New York, 1999), p. 37.
- [7] J.P. Gollub et al., *Phys. Rev. Lett.* **67**, 3507 (1991).

- [8] *Wake Turbulence Consistency* (ABCNews.com, November 15, 2001).
- [9] U. Frisch and S.A. Orszag, *Physics Today* **January**, 24 (1990).
- [10] M. Nelkin, *Am. J. Phys.* **68**, 310 (2000).
- [11] K.R. Sreenivasan, *Rev. Mod. Phys.* **71**, S383 (1999).
- [12] K.R. Sreenivasan and R.A. Antonia, *Annu. Rev. Fluid Mech.* **29**, 435 (1997).
- [13] Z.-S. She, E. Jackson, and S.A. Orszag, *Proc. R. Soc. Lond. A* **434**, 101 (1991).
- [14] U. Frisch, *Turbulence: The Legacy of A.N. Kolmogorov* (Cambridge University Press, Cambridge, 1995).
- [15] O. Reynolds, *Phil. Trans. R. Soc. Lond.* **174**, 935 (1883).
- [16] O. Reynolds, *Phil. Trans. R. Soc. Lond. A* **186**, 123 (1895).
- [17] L.F. Richardson, *Weather Prediction by Numerical Process* (Cambridge University Press, Cambridge, 1922).
- [18] A.N. Kolmogorov, *Dokl. Akad. Nauk. SSSR* **30**, 299 (1941).
- [19] A.N. Kolmogorov, *Dokl. Akad. Nauk. SSSR* **31**, 538 (1941).
- [20] G.K. Batchelor and A.A. Townsend, *Proc. R. Soc. Lond. A* **199**, 238 (1949).
- [21] R.H. Kraichnan, *Phys. Fluids* **10**, 2080 (1967).
- [22] U. Frisch and R. Morf, *Phys. Rev. A* **23**, 2673 (1981).
- [23] A.N. Kolmogorov, *J. Fluid Mech.* **13**, 82 (1962).

- [24] F. Anselmet, Y. Cagne, E.J. Hopfinger, and R.A. Antonia, *J. Fluid Mech.* **140**, 63 (1984).
- [25] B. Mandelbrot, *J. Fluid Mech.* **62**, 331, (1974).
- [26] C. Meneveau and K.R. Sreenivasan, *Phys. Rev. Lett.* **59**, 1424 (1987).
- [27] R. Prasad, C. Meneveau, and K.R. Sreenivasan, *Phys. Rev. Lett.* **61**, 74 (1988).
- [28] K.R. Sreenivasan and C. Meneveau, *Phys. Rev. A* **38**, 6287 (1988).
- [29] P. Constantin, *SIAM Review* **36**, 73 (1994).
- [30] R.M. Kerr, *Phys. Fluids A* **5**, 1725 (1993).
- [31] J.M. Greene and R.B. Pelz, *Phys. Rev. E* **62**, 7982 (2000).
- [32] O.N. Boratav and R.B. Pelz, *Phys. Fluids* **7**, 1712 (1995).
- [33] R.M. Kerr, *J. Fluid Mech.* **153**, 31 (1985).
- [34] A. Vincent and M. Meneguzzi, *J. Fluid Mech.* **258**, 245 (1994).
- [35] N. Cao, S. Chen, and G. Doolen, *Phys. Fluids* **11**, 2235 (1999).
- [36] D. Bonn, Y. Couder, P.H.J. van Dam, and S. Douady, *Phys. Rev. E* **47**, R28 (1993).
- [37] B. Tao, J. Katz, and C. Meneveau, *Phys. Fluids* **12**, 941 (2000).
- [38] S. Kida and K. Ohkitani, *Phys. Fluids* **4**, 1018 (1992).

- [39] *Fluid Mechanics Measurement*, edited by R.J. Goldstein (Taylor and Francis, Washington D.C., 1996).
- [40] U. Piomelli, J.-L. Balint, and J.M. Wallace, *Phys. Fluids A* **1**, 609 (1989).
- [41] I. Hosokawa, S.-I. Oide, and K. Yamamoto, *Phys. Rev. Lett.* **77**, 4548 (1996).
- [42] S.-R. Park and J.M. Wallace, *Exp. in Fluids* **16**, 17 (1993).
- [43] J.-L. Balint, J.M. Wallace, and P. Vukoslavčević, *J. Fluid Mech.* **228**, 53 (1991).
- [44] P. Vukoslavčević, J.M. Wallace, and J.-L. Balint, *J. Fluid Mech.* **228**, 25 (1991).
- [45] A. Tsinober, E. Kit, and T. Dracos, *J. Fluid Mech.* **242**, 169 (1992).
- [46] P. Vukoslavčević and J.M. Wallace, *Meas. Sci. Technol.* **7**, 1451 (1996).
- [47] R.B. Loucks, *An Experimental Examination of the Velocity and Vorticity Fields in a Plane Mixing Layer* (Ph.D. Dissertation, The University of Maryland, College Park, 1998).
- [48] H.Z. Cummins, N. Knable, and Y. Yeh, *Phys. Rev. Lett.* **12**, 150 (1964).
- [49] C. Tropea, *Meas. Sci. Technol.* **6**, 605 (1995).
- [50] A. Cenedese, G.P. Romano, and F. Di Felice, *Exp. in Fluids* **11**, 351 (1991).
- [51] J.M. Wallace and J.F. Foss, *Ann. Rev. Fluid Mech.* **27**, 469 (1995).
- [52] N. Mordant, P. Metz, O. Michel, and J.-F. Pinton, *Phys. Rev. Lett.* **87**, 214501-1 (2001).

- [53] G.A. Voth, K. Satyanarayan, and E. Bodenschatz, *Phys. Fluids* **10**, 2268 (1998).
- [54] A. La Porta, G.A. Voth, A.M. Crawford, J. Alexander, and E. Bodenschatz, *Nature* **409**, 1017 (2001).
- [55] R. D. Keane and R.J. Adrian, *App. Sci. Res.* **49**, 191 (1992).
- [56] M. Raffel, C.E. Willert, and J. Kompenhans, *Particle Image Velocimetry: A Practical Guide* (Springer, Berlin, 1998).
- [57] B. Tao, J. Katz, and C. Meneveau, *J. Fluid Mech.* (in press).
- [58] B. Tao, *Development of Holographic Particle Image Velocimetry and its Application in Three-dimensional Velocity Measurement and Modeling of High Reynolds Number Turbulent Flows* (Ph.D. Dissertation, The Johns Hopkins University, 2000).
- [59] S. Chen, K.R. Sreenivasan, and M. Nelkin, *Phys. Rev. Lett.* **79**, 1253 (1997).
- [60] I.P.D. De Silva and H.J.S. Fernando, *Phys. Fluids* **6**, 2455 (1994).
- [61] A. Srdic, H.J.S. Fernando, *Exp. in Fluids*, **20**, 395 (1996).
- [62] E.D. Siggia, *Annu. Rev. Fluid Mech.* **26**, 137 (1994).
- [63] C.W. van Atta and W.Y. Chen, *J. Fluid Mech.* **44**, 145 (1970).
- [64] M. Holzer and E.D. Siggia, *Phys. Fluids* **5**, 2525 (1993).
- [65] P. Vedula and P.K. Yeung, *Phys. Fluids* **11**, 1208 (1999).
- [66] E. Villermaux, B. Sixou, and Y. Gagne, *Phys. Fluids* **7**, 2008 (1995).

Benjamin Wolf Zeff

11215 Oak Leaf Drive #309
Silver Spring, MD 20901
(h) 301.592.9120 (w) 301.405.7986
wolf@window.umd.edu

EDUCATION

Ph.D. in Physics, May 2002
University of Maryland, College Park

M.S. in Physics, December 1999
University of Maryland, College Park

B.S. in Physics, May 1997
Emory University, Atlanta, GA

RESEARCH

Graduate Research Fellow/Assistant: nonlinear dynamics, 8/97-5/02
Turbulent flows at dissipative length scales (dissertation work).

- Developed a long-range, high-speed micro particle image velocimetry system to facilitate the three-dimensional study of turbulent dissipation (provisional patent application submitted).
- Studied dissipation-scale dynamics of grid-generated turbulence and turbulent convection.
- Developed digital image analysis algorithm and software.
- Designed and fabricated tank for study of turbulent convective flows. Experimental chaotic scattering of light.

- Studied chaotic scattering using a novel optical billiards system.
- Devised unique photographic techniques for image acquisition.

Singularities on a fluid surface.

- Designed and fabricated a surface wave tank.
- Developed a technique for producing a repeatable singular event.
- Designed and implemented computer and electronic control system.
- Developed laser velocity measurement and high-speed flash photography techniques.

Sodium dynamo experiments.

- Designed and built heating system.
- Managed safety equipment and procedures in sodium lab.

Undergraduate Research Assistant: nonlinear dynamics, 10/95-5/97

- Implemented temperature control, heating, thermometry, and data acquisition systems and wrote data acquisition program for dynamo experiment.
- Developed and printed photos for surface wave experiments.

TEACHING

Teaching Assistant: introductory college physics I & II, 9/95-5/97

Wrote and graded assignments and tutored students.

PUBLICATIONS & PRESENTATIONS

- B.W. Zeff, D.D. Lanterman, R. McAllister, R. Roy, E.J. Kostelich, and D.P. Lathrop, *submitted to Science*.
- D. Sweet, B. Zeff, E. Ott, and D.P. Lathrop, *Physica D* **154**, 207 (2001).
- B.W. Zeff, B. Kleber, J. Fineberg, and D.P. Lathrop, *Nature* **403**, 6768 (2000).
- B.W. Zeff, Emory Undergraduate Thesis, (1997).

- “3-D Measurement of Local Dissipation in Turbulent Convection and Grid Turbulence”—APS/DFD Meeting, San Diego and Applied Dynamics Seminar, University of Maryland, November 2001.
- “Observing Turbulence from the Inside Out”—Applied Dynamics Seminar, University of Maryland & SIAM Dynamical Systems Meeting, Snowbird, UT, May 2001.
- “Singularities and Jet Eruption on a Fluid Surface”—Johns Hopkins University Department of Mechanical Engineering (Invited Lecture), October 1999.
- “Singularities on a Fluid Surface”—Applied Dynamics Seminar, University of Maryland, Spring 1999.
- “Formation of Singularities on a Liquid Free Surface”—APS/DFD Fluid Dynamics Meeting, Philadelphia, November 1998.

SPECIAL SKILLS

- Experience in BASIC, HTML, C and C++, LabVIEW, LATEX, CorelDRAW, Photoshop, Windows, Macintosh OS, and UNIX
- Extensive machine shop experience with metals and plastics using lathes and milling machines
- Graphic arts work including pen & ink, watercolor, and computer graphics

HONORS & AWARDS

- National Science Foundation Graduate Research Fellowship, 1997-2000
- Emory University, Charles Duncan Full-Tuition Scholarship, 1993-1997
- Hughes Undergraduate Summer Research Fellowship, 1996
- Phi Beta Kappa Honors Society
- Sigma Pi Sigma Physics Honors Society

MEMBERSHIPS

- American Physical Society